University of Alberta

Non-Equilibrium Containerless Solidification of Al-Ni Alloys

by

Arash Ilbagi

A thesis submitted to the Faculty of Graduate Studies and Research
in partial fulfillment of the requirements for the degree of

Doctor of Philosophy

in

Materials Engineering

Chemical and Materials Engineering

Spring 2012
Edmonton, Alberta

Abstract

More than 90% of all metallic materials are manufactured starting from their liquid state. Designing the solid structure produced during solidification can have major savings in downstream processing. Rapid solidification yields significant enhancement in properties through refined microstructure, reduced microsegregation and the formation of metastable phases. To control the microstructure obtained from rapid solidification and attain desired properties, understanding of effects of processing parameters, in particular cooling rate and undercooling on microstructure evolution is required. In the case of peritectic reaction this understanding is lacking.

In this dissertation, the effect of cooling rate on the peritectic reactions occurring in the binary Al-Ni system is investigated. Impulse Atomization technique was used to produce rapidly solidified particles of Al-36 wt%Ni and Al-50wt%Ni. The effect of cooling rate on the microstructure evolution and phase fractions achieved after solidification was studied. Also, porosity formation in the atomized particles was investigated and the effect of processing parameters on the amount and distribution of porosity was analyzed. For characterization, neutron diffraction, X-ray micro-tomography, electron and optical microscopy were utilized.

The results showed that in both Al-36 wt%Ni and Al-50 wt%Ni, cooling rate has a significant effect on the formation of microstructure, phase fractions and metastable phase formation. It was shown that at different cooling rate

regimes different mechanisms are responsible for the changes observed in the phase fractions.

Using X-Ray tomography, multiple nucleation sites were observed in large particles, while smaller particles contained only a single nucleation site. Also, porosity within the particles was quantified and the distribution of porosity with regard to the nucleation site and cooling rate is discussed. The distribution of porosity within the small particles and large particles was found to be significantly different. Quantitative analysis of the micro-tomography images revealed that the volume percent of porosity decreased with increasing cooling rate. Also, it was found that for higher cooling rates, porosity tends to form closer to the periphery of the particles, whereas at lower cooling rates the pores are more randomly distributed.

Acknowledgements

First and foremost I offer my sincerest gratitude to my supervisor, Professor Hani Henein, who has supported me throughout my thesis with his patience and knowledge whilst allowing me the room to work in my own way. He not only helped me professionally, but also taught me how to be a better person.

I would like to show my gratitude to Dr. Jon Johansson, Denise Thornton and Maria Kazakevich from Academic Information and Communication Technologies (AICT) who helped me analyze the X-ray micro-tomography images.

I would like to thank Dr. Ian Swainson, National Research Council Canada (NRC), who taught me how to perform the Rietveld analysis. Also, many valuable discussions with Dr. Guillaume Reinhart, IM2NP, gave me new ideas to achieve my project goals.

The technical support from Bob Smith and Clark Bicknell (machine shop) and Walter Bodez, Less Dean and Richard Cooper (instrument shop) is greatly appreciated.

I am grateful to Dr. Arvind Prasad for supporting me when I started my program. I would like to also thank Mr. Pooya Delshad Khatibi for his help in performing the experiments.

My Mother, Shahindokht Varasteh, and my father, Amirmansour Ilbagi, deserve special mention for their inseparable support and prayers. I cannot

imagine where I would be without them. Also, I want to thank my sister, Ellie Ilbagi, for her support.

Words fail me to express my appreciation to my wife, Mahshid Mohammadi, whose dedication, love and persistent confidence in me, has taken the load off my shoulder.

This project was funded by the Natural Sciences and Engineering Research Council of Canada (NSERC), the Canadian Space Agency (CSA) and the European Space Agency (ESA).

Table of Contents

List of Tables

List of Figures

List of symbols and abbreviations

C_0	Original alloy composition, %
C_s	Composition of solid
C_l^m	Composition of the last liquid to solidify
D	Diffusion coefficient, m^2s^{-1}
EML	Electromagnetic levitation
f_s	Fraction of solid
G_l	Free energy of liquid, J
G_s	Free energy of solid, J
ΔG	Gibbs free energy change, J
ΔG_B	Gibbs free energy change upon freezing, J
IA	Impulse atomization
k	Partition coefficient
M	Coarsening factor
m	Equilibrium liquidus slope
ND	Neutron diffraction
r	Radius, m
SDAS	Secondary dendrite arm spacing, m

SEM Scanning electron microscopy

T_m Melting temperature, K

W_i Weighting factor for each observation point

wRp Weighted profile residual

y(calc) Calculated profile

y(obs) Observed profile

Greek symbols

γ Surface energy, j/m^2

Γ Gibbs-Thomson coefficient, mK

λ Secondary dendrite arm spacing, m

χ Goodness of fit

Chapter 1

1. Introduction

The structure of materials plays an important role in governing their properties. Solidification is considered a key step in developing the structure of an engineered material. More than 90% of all metallic materials are manufactured starting from their liquid state. Designing the solid structure produced during solidification can yield major savings in downstream processing.

Solidification is a complex phenomenon where variation of undercooling or cooling rate results in significantly different structures. Deep undercooling of materials below their equilibrium liquidus temperature results in rapid solidification. This cooling below the liquidus renders the melt metastable with respect to the lower Gibb's free energy of the corresponding solid state. Undercooling is needed to overcome the nucleation energy barrier of the new phase. It also provides the driving force for the formation of metastable solids. In contrast to near-equilibrium solidification, there is more than one solidification pathway which may result in a broad range of metastable microstructures with different physical and chemical properties [1.1].

Rapid solidification is considered an innovative method towards new production routes of novel materials [1.2] which can achieve the following [1.3]:

1. A refined structure,

2. Extension of solid solubility in the primary phase,

3. A morphology change of eutectic and/or primary phases,

4. Formation of metastable phases.

The first step in solidification of materials is the extraction of heat from the liquid. The mode of heat extraction has an important role in the evolution of microstructure. During the formation of the solid, the latent heat is released and has to be extracted. The heat extraction can be through the solid phase, called constrained growth, or can be through the liquid phase, called unconstrained growth. Differences in growth mode may result in different morphologies of the solidified phase.

In the past several years, dendritic growth and eutectic growth of undercooled melts have been studied extensively [1.4]. On the other hand, relatively less research has been focused on solidification with a peritectic reaction. Although the mechanism of this reaction has been studied by some researchers, e.g. Lee et al. [1.5], the understanding of the reaction is limited [1.6]. So far, levitation [1.7] and directional solidification [1.8] have been used to study the peritectic formation in some alloy systems; however, the effects of cooling rate or solidification velocity on the fractions of the primary and peritectic phases in binary peritectic alloys have not been studied extensively [1.7].

The goal of this project is to study the rapid solidification in peritectic alloys and to explore the effect of processing parameters on the microstructure evolution during solidification. Furthermore, porosity formation within the

solidifying specimen, which is also influenced by processing parameters, is studied using 3D imaging techniques. The study will be conducted for Al-Ni binary system. Impulse Atomization (IA) is used to generate Al-Ni powders, on which, microstructural studies are performed using neutron diffraction (ND), scanning electron microscope (SEM) and X-ray micro-tomography. The data from this project will contribute to the development of a full description of the microstructural evolution during rapid solidification of peritectic alloys.

1.1. Thesis layout

Chapter 2 reviews fundamentals of solidification as well as the research efforts by other scientists in this field. In particular, it covers background information about peritectic transformation and Impulse-Atomization as the processing technique. At the end of the chapter the objectives of this thesis work are described. In Chapter 3 the experimental procedures used in this research are outlined. Chapters 4 and 5 are devoted to microstructural analysis of Al-36 wt%Ni and Al- 50 wt%Ni alloys, respectively. In Chapter 6 the microstructure of an electromagnetically levitated droplet of Al- 50 wt%Ni alloy solidified in microgravity is described. In Chapter 7 the results from different techniques are compared and conclusions arising from this study and areas for further research are outlined.

1.2. References

1.1. Herlach, D. M. and Feuerbacher, B., "Non-Equilibrium Solidification of Undercooled Metallic Melts", Advances in Space Research, Vol. 11, No. 7, (1991), 255.

1.2. Herlach, D. M., "Metastable Materials Solidified from Undercooled Melts", Journal of Physics: Condensed Matter, Vol. 13, (2001), 7737–7751.

1.3. Pryds, N. H., Pedersen, A. S., "Rapid Solidification of Martensitic Stainless Steel Atomized Droplets", Metallurgy and Materials Science, Vol. 33, No. 12, (2002), 3755-3761.

1.4. Li, M., Kuribayashi, K., "Free Solidification of Undercooled Eutectics", Materials Transactions, Vol. 47, No. 12, (2006), 2889-2897.

1.5. Lee, J. H., Verhoeven, J. D., "Peritectic Formation in the Ni-Al System", Journal of Crystal Growth, 144, (1994), 353-366.

1.6. Kerr, H. W., Kurz, W., "Solidification of Peritectic Alloys", International Materials Reviews, Vol. 41, No. 4, (1996), 129-164.

1.7. Herlach, D. M., Galenko, P., Holland-Moritz, D., "Metastable Solids from Undercooled Melts", Pergamon, (2007).

1.8. Cao, C. D., Lu, X. Y., Wei, B., "Peritectic Solidification of Highly Undercooled Cu-Co Alloy", Advances in Space Research, Vol. 24, No. 10, (1999), 1251-1255.

Chapter 2

2. Literature Review

2.1. Nucleation

The solidification of a liquid is initiated by thermally activated nucleation. If the liquid is cooled below the melting point, the free energy of the solid becomes lower than that of the liquid. This is the driving force for liquid to solidify. However, it is quite easy to undercool a number of liquids which shows that there is some barrier to solidification. The barrier to starting solidification is known to arise from the positive free energy associated with the formation of the surface area of the nuclei. To account for this surface effect the free energy change to form a homogenous spherical nucleus is defined as:

$$\Delta G=4/3\pi r^3\Delta G_B+4\pi r^2\gamma \qquad (2.1)$$

where, ΔG_B in the first term of Eq. 2.1 is the free energy change per unit volume upon freezing as $\Delta G_B=G_s-G_l$ and G_s and G_l are the free energy of solid and liquid, respectively. In the second term of Eq 2.1, γ represents surface energy per unit area. The two terms of Eq. 2.1 as well as the total free energy change are plotted in Figure 2.1 as a function of cluster size. At the freezing temperature ΔG_B is zero and it becomes more negative as the metal is undercooled below the freezing

temperature. On the other hand, the positive surface free energy inhibits the solidification process. Whenever the total free energy change reaches a critical value, G*, homogeneous nucleation occurs. In other words, homogeneous nucleation limits the degree to which a melt can undercool and is seldom observed. In practice, heterogeneous nucleation plays the most important role. In heterogeneous nucleation, besides the solid nucleus and the undercooled melt a third partner is involved. In particular, container walls and metal oxides can catalyze the heterogeneous nucleation process and limit the degree of undercooling of a melt.

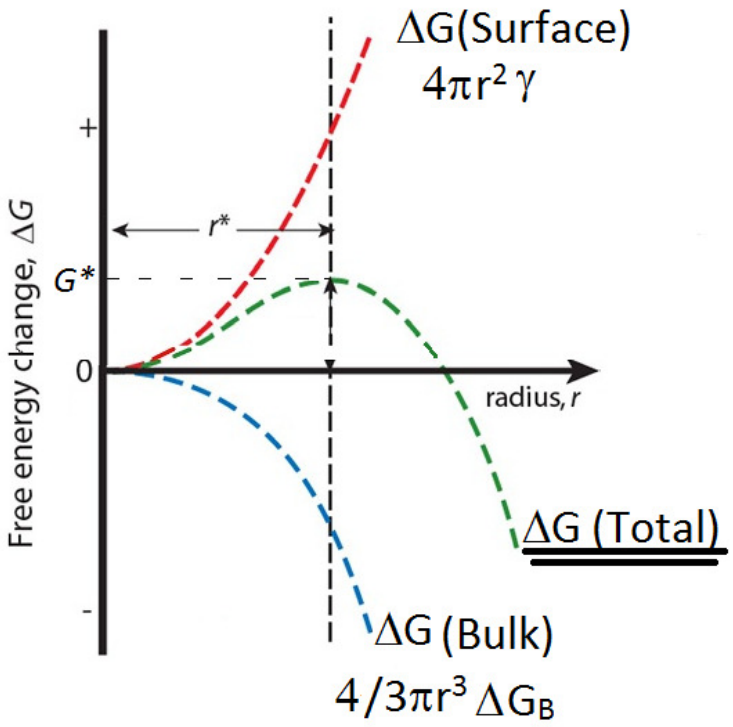

Figure 2.1. Free energy of formation of a nucleus as a function of its radius.

2.2. Constrained and Unconstrained Growth

During phase change, latent heat can be released through two different paths. When it is extracted through the solid phase, it is called constrained growth. Unconstrained growth is the extraction of latent heat through the liquid phase.

In constrained growth, the solidification of metals produces three different zones. At mould/metal interface, where the cooling rate is highest, a significant number of small grains form, named as the outer equiaxed zone. Such grains then grow in the opposite direction of heat transfer along their preferred crystallographic directions, which leads to the formation of a columnar zone. The third zone, called inner equiaxed zone is formed mainly as a result of the growth of detached dendrite arms in the remaining liquid [2.1]. To study the growth rate of solid/liquid interface in constrained growth Boettinger et al. [2.2] performed electron beam solidification passes on a series of Ag-Cu alloys. He showed that morphology and microsegregation in the rapidly solidified material change with the velocity of the solid-liquid interface.

In unconstrained growth that occurs in containerless solidification processes, the solid grows into an undercooled melt as the latent heat of solidification flows down the negative temperature gradient in the liquid. Rapid solidification for this kind of growth is less well understood than constrained growth, primarily due to practical difficulties in obtaining experimental information during unconstrained solidification for the validation of mathematical models [2.3]. The resulting microstructure of this form of the growth can be affected by undercooling and growth rate. A review on what have been done on

the study of the theory of unconstrained growth in an undercooled melt using containerless processing techniques will be discussed in this chapter.

2.3. Peritectic Solidification

A peritectic reaction, where solid 1 (α)+L (liquid) → solid 2 (β), is found in technically important alloy systems such as iron-carbon and iron-nickel-base alloys as well as copper-tin and copper-zinc alloys. However, not until recently has the possible range of complex solidification microstructures of these alloys come to be fully discussed. This section presents some of the complexities of this reaction. Figure 2.2a shows a phase diagram with a peritectic reaction. Under equilibrium condition all alloys to the left of I will solidify as α crystals. Solidification of alloys with composition between I and II starts with the formation of the α crystals. Then, some of these primary crystals react with the liquid and transform to β crystals. Similarly, alloys between lines II and III first solidify to α crystals and then β crystals start to form on the interface between α and the liquid. All the alloys to the right of III will result in β crystals. All alloy compositions between I and III will undergo a peritectic reaction.

2.3.1 Nucleation and Growth of the β Phase

It is believed that the nucleation of the β phase occurs at the interface between the liquid and primary α phases. That is due to the fact that the rejection of the solute from α phase facilitates the nucleation of β. Formation of the β phase at this stage

may be relatively quick, since diffusion can occur rapidly in the liquid.

When α phase is surrounded by β, further transformation can occur as a result of the diffusion through β. This is known as “peritectic transformation”. Upon further cooling more β phase may form directly from the liquid [2.4].

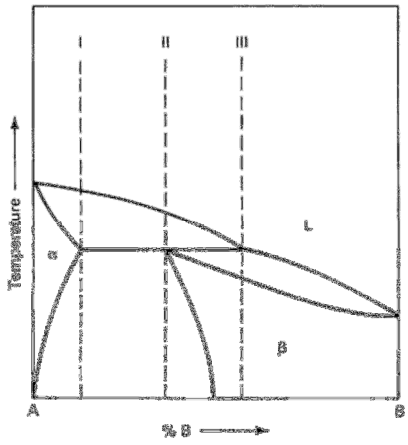

(a)

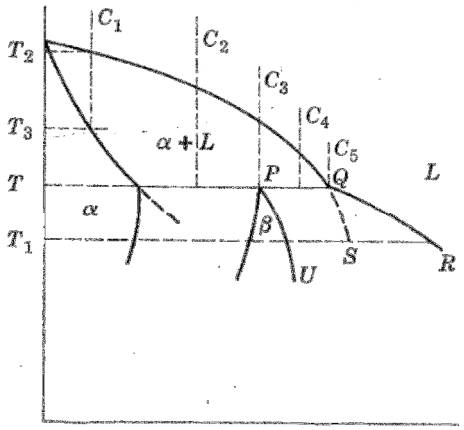

(b)

Figure 2.2. Schematic of a peritectic reaction.

The peritectic reaction is extremely slow, because after the formation of the first layer of β, the completion of the reaction demands the diffusion of solute through β. Therefore, in solidification of most alloys, the peritectic reaction cannot take place to an appreciable extent, because of incomplete diffusion in the solid. Under non-equilibrium conditions and assuming no diffusion in solid, it may be possible to simulate the peritectic reaction using Scheil-Gulliver model as discussed by Chen et al. [2.5]. The next section is devoted to this simulation.

2.3.2. Non Equilibrium Solidification in Peritectic alloys

The Scheil-Gulliver equation predicts solute redistribution during solidification of an alloy. In this approach the non-equilibrium solidification is approximated by using a local equilibrium at the solidification front, which allows the use of phase diagram in solidification analysis. However, Scheil-Gulliver assumes no diffusion in solid and complete mixing in liquid.

The Scheil-Gulliver model for an alloy with composition C_2 in Figure 2.2b as an example predicts the formation of primary α phase followed by the solidification of β phase. The liquid composition follows the liquidus line. Before reaching the peritectic temperature, the primary α phase solidifies from the liquid. Then, the solidification of β phase begins. Since Scheil-Gulliver assumes no diffusion in solid the solidified α phase is not allowed to react with the liquid to form the β phase. Therefore, in simulation of peritectic reaction using Scheil-Gulliver model the peritectic reaction does not take place [2.5].

Chalmers [2.6] discussed four possible scenarios for non-equilibrium solidification of alloys with a peritectic reaction assuming that no diffusion occurs in the solid while the liquid mixes only by diffusion.

1. If an alloy with composition C_1 (Figure 2.2b) is cooled to T_2, solid α may start to nucleate. While growing, solid α rejects B into the liquid. The composition of the solid α that is being formed moves to the right due to the incomplete diffusion in solid and constitutional undercooling will occur. The liquid, gradually, is being enriched in B and its composition may reach C_5 that is where β crystals start to form. The final microstructure consists of α and β phases.

2. For an alloy with composition C_2 Chalmers proposed a steady state formation of both α and β in a way that the resulting microstructure resembles a eutectic structure. Later, others such as Dolber et al. [2.7] using directional solidification showed under certain conditions it is possible to have peritectic coupled growth. In his experiments, Dolber observed that G/V ratio (thermal gradient/interface velocity) should be close or above the critical value for plane front growth of both solid phases.

3. An alloy with composition C_3 can reach a steady state in which the β phase forms at the interface which has the composition Q. At the final stage of the solidification of a sample with this composition, the final liquid to solidify moves the composition to the right on the QR line. The final solid forms in temperatures below T_1, and has composition on the line PU.

4. Alloy with composition C_4 starts to solidify by the formation of α. β is

formed from any liquid when its composition reaches Q. Eventually; the microstructure consists of primary crystal of α surrounded by the β crystals.

Based on different scenarios mentioned by Chalmers it is expected that the primary α phase persists, though it is not the stable phase. On the other hand, Löser et al. [2.8] investigated the change of the primary solidification mode in undercooled peritectic melts of three different alloys, Fe-Mo, Co-Si and Al-Co, using electromagnetic levitation. They observed that below a critical undercooling, the growth of the primary phase is suppressed and is replaced by the respective peritectic phase. In a different work, Chen et al. [2.9] undercooled Fe-4.35 at.%Ni using a glass fluxing technique. They found that above a critical undercooling the peritectic reaction is suppressed. They related this phenomenon to poor lattice match between γ (fcc) and δ (bcc). They believe that to start a peritectic reaction a small amount of γ phase has to deposit on the properitectic phase δ. They defined the time required to deposit this amount as an incubation time. If the time required for solidification of δ phase in certain undercooling is less than incubation time, the peritectic reaction will be suppressed. Biswas et al. [2.10] observed a different behavior in rapid solidification of Fe-Ge alloy droplets. He found that above certain undercooling the primary phase α is absent and only the peritectic phase (ε) is present. They concluded that the peritectic reaction α+liquid→ε is suppressed, however, the ε phase formed as a result of solid-state transformation.

So far, most of the studies on peritectic reaction have been done using directional solidification, which results in constrained growth. While this

technique provides valuable information about phase and microstructure selection in peritectic alloys, it lacks the ability to represent the containerless solidification. In the following sections, some containerless processes that can be utilized in studying peritectic reactions are presented. Also, in order to prevent repetition, more details about peritectic reactions will be given in the next chapters in order to better understand the experimental results.

2.4. Electromagnetic levitation (EML)

The levitation technique is used to suspend a drop without any contact to a solid or liquid medium. This technique offers the possibility of undercooling big droplets [2.11]. Two induction coils are used to levitate the sample (positioning) while heating it. After the droplet melts and reaches the desired temperature, it is cooled by the flow of inert gas. Nucleation starts either spontaneously or by any external means of triggering nucleation.

EML of droplets allows for direct observation of undercooling and solidification and can achieve very high undercoolings in large droplets (~6mm) that solidify in a containerless environment. However, the solidification of a droplet in such a system is strongly disturbed by large stirring effects from the electromagnetic forces used for positioning and heating the sample. It is possible to reduce the positioning-driven flows by performing experiments in microgravity. Reutzel et al. [2.12] used EML to measure the velocity of dendrite growth in undercooled Ni-Al alloy melts as a function of undercooling. The

experiments were performed on Earth and under reduced gravity conditions during parabolic flight campaigns. It was found that induced convection by electromagnetic forces leads to an increase of the heat and mass transport ahead of the solid-liquid interface; therefore, higher dendrite growth velocity was achieved in the terrestrial condition than that in reduced gravity. This is shown in Figure 2.3.

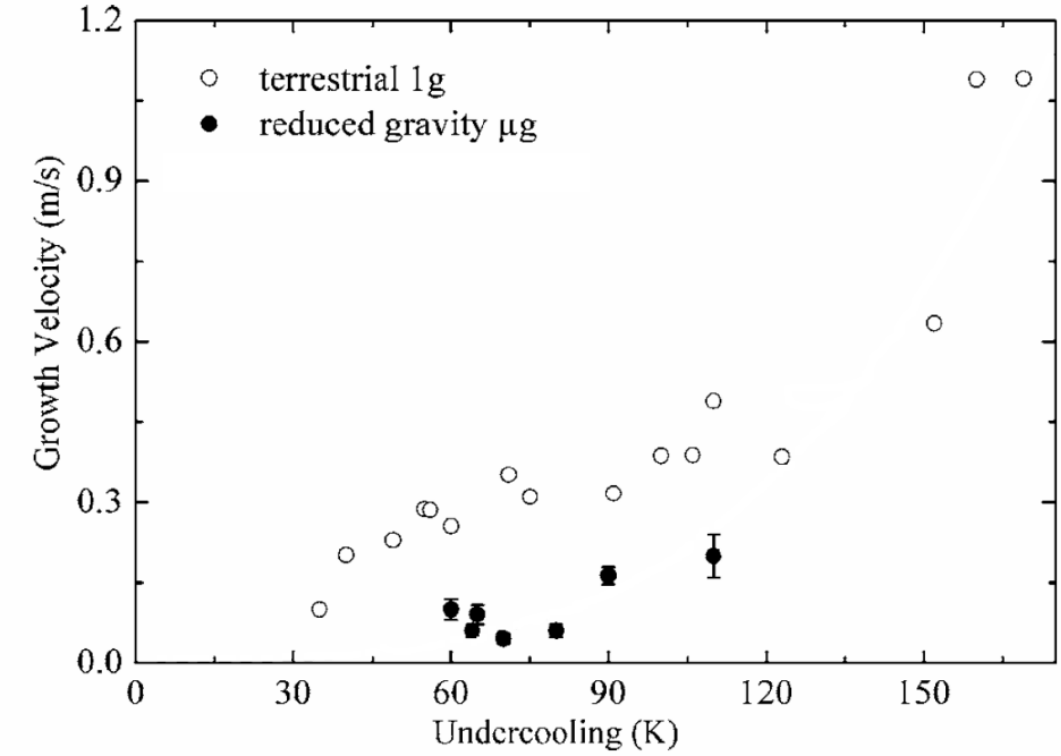

Figure 2.3. Dendrite growth velocity as a function of undercooling measured in $Ni_{50}Al_{50}$ alloy in terrestrial condition and reduced gravity [2.12]. 1g and μg in the legend represent terrestrial gravity and microgravity.

Also, Hanlon et al. showed that the internal flow induced by electromagnetic forces is strong enough to cause damage to the primary dendrite arms [2.13]. Therefore, performing experiment under microgravity will help reduce the disturbance from external forces during EML experiments.

2.5. Drop tube [1]

A combination of rapid cooling, containerless solidification and low gravity can be achieved during the falling of micron sized molten droplets in a drop tube. This technique has been used quite extensively to study containerless solidification of materials [2.14-15]. In this technique the material under study is loaded into the top of the drop tube, which is backfilled with inert gas or evacuated. Following melting, the sample is released to fall to the bottom of the tube.

The drop tube provides the simplest, safest and least expensive way of obtaining microgravity environment. The level of microgravity achievable using this technique is relatively high, i.e. up to 1×10^{-5} of the earth's gravity [2.16], which is difficult to reach in other microgravity platforms, and the test is reproducible. However, the duration of microgravity supplied by drop tubes is short and many of the samples tested cannot solidify while falling in an evacuated drop tube. For example, the temperature of a 2 mm droplet of aluminum with overheating of 0.1 T_m (melting point) decreases only 19 K during 50 meters

[1] A version of Sections 2.5, 2.6, 2.7, 2.8 and 2.9 has been submitted for publication. Containerless Undercooling of Drople and Droples. Edited by D.M. Herlach and D. M. Matson, Copyright © 2011 WILEY-VCH Verlag GmbH & Co. KGaA, Weinheim, ISBN 978-3-527-33122-2.

falling height [2.17]. Therefore, usually gases are introduced into the tube to ensure solidification of the falling molten droplets at the expense of deteriorating the low gravity level. In this condition, smaller sample size, higher gas pressure and faster initial falling velocity result in a faster disappearance of the microgravity condition. However, in spite of losing the microgravity condition as a result of the drag force applied on the particles, the solidification of materials in a drop tube filled with cooling gas is of great interest due to the containerless and high cooling rate conditions it supplies. Also, since the heat transfer conditions for movement of a hot spherical body in stagnant fluid are well understood, it is feasible to use experimental data to validate droplet cooling models. For this purpose, in large drop tower facilities, photodetectors are arranged at various places along the drop tube to measure the cooling rate and the sudden increase of temperature during recalescence. The latter is of great importance as it allows for evaluating the undercooling prior to nucleation. In drop tubes of smaller sizes, however, due to practical difficulties, it has been a common belief that it is not possible to record the thermal history during the solidification of the individual droplets. Apart from the thermal history, in-situ measurement of the droplets' diameter, initial velocity and instantaneous velocity is crucial in validating the heat transfer models.

2.6. Spray techniques

Spray techniques are considered containerless processing technique and are capable of producing rapidly solidified materials. The idea behind these

techniques is to destabilize a stream of liquid metal to form tiny droplets that are then made to lose heat rapidly by different means. Melt atomization is one of the most popular spray methods and can be used in studying the solidification with unconstrained growth. In this method, the melt is disintegrated by mechanical means (e.g., IA, centrifugal atomization, etc.) and is called single-fluid atomization. Two-fluid atomization is a spray technique where disintegration of the melt is achieved by blowing high pressure fluid (e.g., gas atomization and water atomization). After disintegration, the produced droplets fall through a much colder fluid medium and solidify. Melt atomization can create droplets with diameters of only a few microns. High degrees of cooling rate and undercooling can be achieved using this technique.

A large volume of a liquid sample contains a variety of nucleation centers that can prevent the liquid metal from attaining large undercoolings prior to solidification. Dispersing the bulk liquid into a collection of fine droplets is an effective approach to isolate potent nucleation sites into a small fraction of droplet population; therefore, a large number of droplets remain without any nucleating agent. Thus, when droplets are cooled, those containing a potent nucleating agent solidify at low undercooling while the majority of droplets attain maximum undercooling [2.18]. It is also believed that the reduction of particle size leads not only to an increase in the cooling rate, but also to a decrease in the probability for nucleation [2.19].

The gas atomization process is the most common powder production technique. However, industrial spray systems typically generate droplets of wide

size distribution that leads to a wide range of reaction or solidification times for droplets in the spray. It has been shown that in gas atomization, due to the blowing high pressure gas, there is a significant droplet velocity gradient in both the radial and axial directions [2.20-21], which varies according to the design of the atomization unit (e.g. the design of gas nozzles and the relative positioning between gas jets in gas atomization). Thus, a wide droplet size distribution is achieved and each droplet finds itself in a different local gas velocity and temperature. Consequently, depending on how the droplets couple and move with the atomizing gas, the microstructure varies. This makes it very difficult to identify how individual process variables can affect the resulting characteristics of individual, or group of, droplets [2.22]. A containerless solidification system based on a single fluid atomization approach can satisfy these requirements and will be discussed in the next section.

2.7. Description of IA

In recent years, atomization of melts (high temperature fluids such as metals, alloys and slags) has seen significant innovative revolutionary new breakthroughs, developments and capabilities. These are primarily with the single fluid atomization approach where a melt stream is rendered unstable in a static gas atmosphere or where individual drops are generated. Under the right atomizing conditions, a mono-size or a controlled and narrow size distribution of droplets is generated [2.23-27]. The droplets are either allowed to fall through a stagnant gas atmosphere and solidify or are deposited onto a substrate. This may be achieved

by allowing the droplets to free fall through a stagnant gas, in a vacuum or reduced pressure in the vessel.

The method that will be the focus of this section is IA[2.28]. IA was developed and patented [2-28, 2.32] at the University of Alberta, Canada. It is a single-fluid atomization technique where a melt stream is generated by pushing the melt out of orifices. Using conventional refractory materials, impulses are mechanically applied to a melt with low frequency and high amplitude (Figure 2.4). These impulses feed the melt through the orifices and provide the melt stream with the required instability for breakup. Thus, discrete lengths of streams generated from an orifice, breakup into droplets. Repeated application of this pressure at low frequency and high amplitude generates droplets as small as 100 μm [2.31]. Since the droplets accelerate under gravity, no droplet collisions occur despite a narrow spray angle (~5^{o}). Powders and granules have been produced with median size (d_{50}) of 100μm to 1.5mm and a lognormal distribution, (d_{84}/d_{50}), of about 1.4 using up to 100 orifices in nozzle plates of 2.5 cm diameter [2.29-31]. The generated droplets spheroidize and lose heat to the surrounding stagnant gas of choice while falling through a 4-meter-long drop tube. Schematics of the process and of the apparatus are shown in Figure 2.4. In this figure, the impulse generator, the plunger (driver), a metal tundish system and a nozzle plate complete with orifices are shown as well as a schematic of the instrumented drop tube.

IA is used to produce rapidly solidified metallic (or non-metallic) droplets and powders. This process can reproducibly yield powders of uniform size-

distribution with cooling rate as high as 10^4 K/s [2.28, 2.33-37]. The process has successfully been employed to produce a wide range of metal droplets including zinc, magnesium, neodymium-iron, lead-tin alloys, aluminum alloys, copper alloys, low carbon steel and tool steel. In the next section, some of the research efforts of other workers utilizing IA for powder production is described in order to better understand the capabilities and expected outcomes of this method.

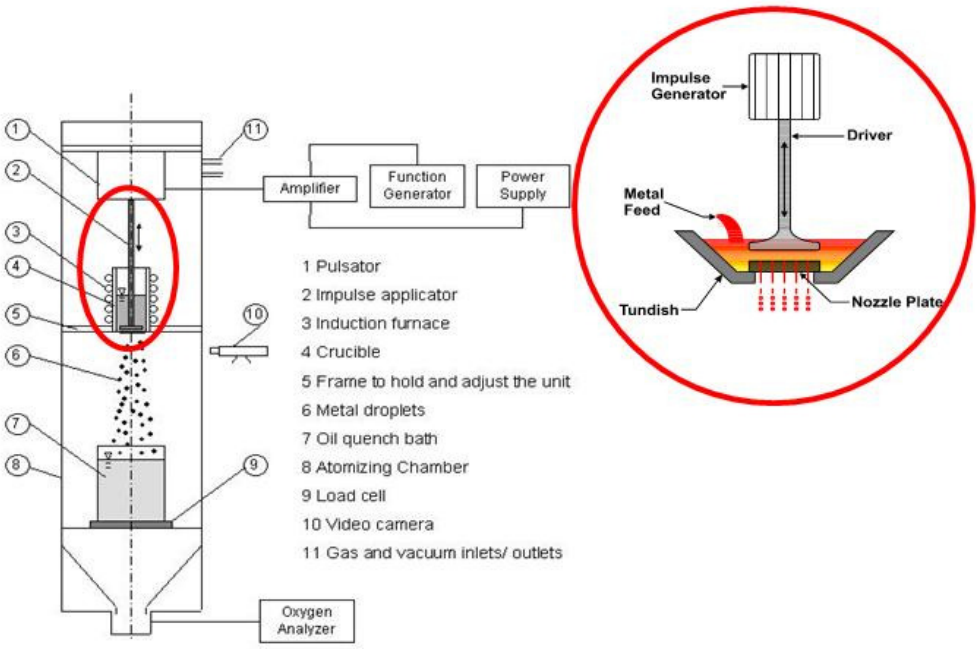

Figure 2.4. Schematic of IA unit [2.31].

Particles solidified using the IA technique experience very limited internal circulation as shown by Prasad et al. [2.36]. They showed that the internal circulation is a function of the ratio of viscosities of the droplet and the surrounding fluid. The high ratio in atomization of most metals results in

extremely limited internal circulation. This is considered an advantage over EML, in which particles experience strong internal flows. Using experimental data coupled with modeling it has also been shown that the IA particles of copper completely solidify while they are experiencing 70% of gravitational acceleration [2.38]. The amount of reduced-gravity achieved during solidification of falling particles can be manipulated by changing the gas type and gas pressure within the tower.

2.8. Powder characteristics

The break up mechanism in IA has been reported by Henein [2.31] and Yuan [2.28]. In IA, discontinuous streams, called ligaments, are produced by an impulse applicator. Without the application of the impulses no molten metal comes out of the orifices. Ligaments are formed out of the orifices during the downward cycle of an impulse. During the other half cycle of an impulse no fluid emanates from the orifices. The discharged ligaments have a sinusoidal natural disturbance on their surface due to the exit velocity of the ligament from the orifice and the applied frequency. The disturbance will have a wavelength λ. According to Rayleigh instability, the minimum theoretical wavelength of the disturbance required for breakup of a liquid stream is $\lambda=\pi d$, where d is the diameter of the ligament, or in other words, the orifice diameter. Hence, if the length of the ligament is smaller than its circumference, the ligament is expected to form only one droplet, and if it is larger than the circumference, the ligament will break up. It has been experimentally observed in IA that each ligament breaks up into

several droplets [2.28].

By varying the impulse driver acceleration, the orifice size, orifice shape, melt temperature and gas atmosphere, the shape, size distribution and microstructure of the powders atomized can be manipulated to the required specifications. IA experiments have been carried out with as many as 97 orifices in a 2.5 cm nozzle plate, producing tailored mass median particle size (D_{50}) and controlled log-normal standard deviations (S.D.) (D_{84}/D_{50}) of $1.1 \leq \sigma \leq 1.6$ [2.31]. Figure 2.5 displays the mass mean (D_{50}) particle size as a function of orifice diameter for aluminum, copper and iron alloys produced using IA. From the slope of the solid line, which represents a linear regression analysis of the data, the ratio between particle size and orifice diameter is about 1.28. In addition, the log-normal S.D. of particle size (D_{84}/D_{50}) for the same alloys and orifices sizes is shown in Figure 2.6. For the alloys atomized, the S.D. lies primarily between 1.3 and 1.5. The results at about 1.9, 1.7 and 1.65 are considered outliers and occurred during early atomization trials with the iron, copper and aluminum alloys, respectively.

Alloy composition also affects the mean droplet size. In Figure 2.7 the mass mean is plotted as a function of the iron content for binary aluminum alloys having iron content ranging from 0 wt% (commercially pure aluminum) to 1.9 wt% for samples atomized in nitrogen and helium. The trend is clear. The mass mean increases with iron content. There is no appreciable effect of atomizing inert gas. An increase in melt surface tension would result in greater droplet sizes during the disintegration of ligaments during atomization. It appears, therefore,

that the presence of iron increases the surface tension of the alloy [2.34], which would result in larger mass median particle size.

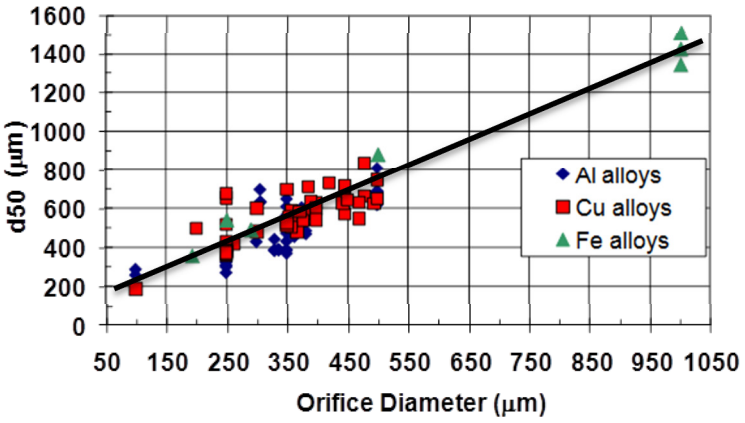

Figure 2.5. Mass mean (D_{50}) particle size as a function of atomizing orifice diameter [2.31].

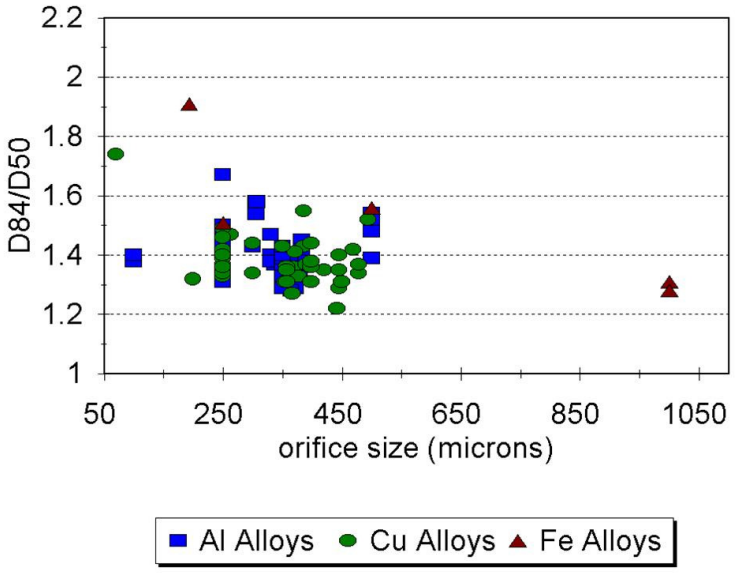

Figure 2.6. Log-normal standard deviation as a function of orifice size [2.31].

Figures 2.8 and 2.9 show the shape and surface structure of copper powders and an Al-17 wt% Cu powder atomized using IA. Both samples were atomized in a nitrogen atmosphere and show highly spherical shaped powders. The Al-17 wt%Cu sample clearly shows a very fine dendritic structure on the surface of the particle. Primary dendrite trunks and secondary dendrite arms are clearly visible. Quantifying the scale of the microstructure and of the fraction of various phases present in these particles will provide valuable data for model verification.

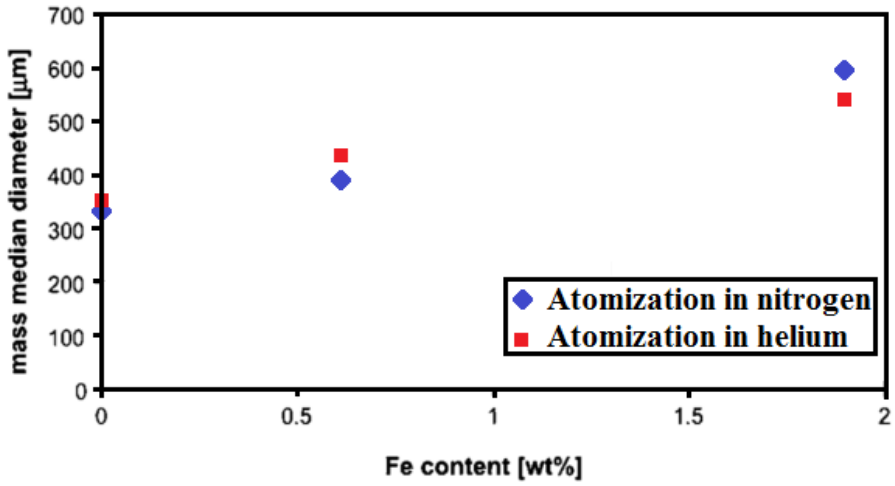

Figure 2.7. Mass median diameter as a function of the iron content in Al-Fe powders atomized in nitrogen and helium [2.34].

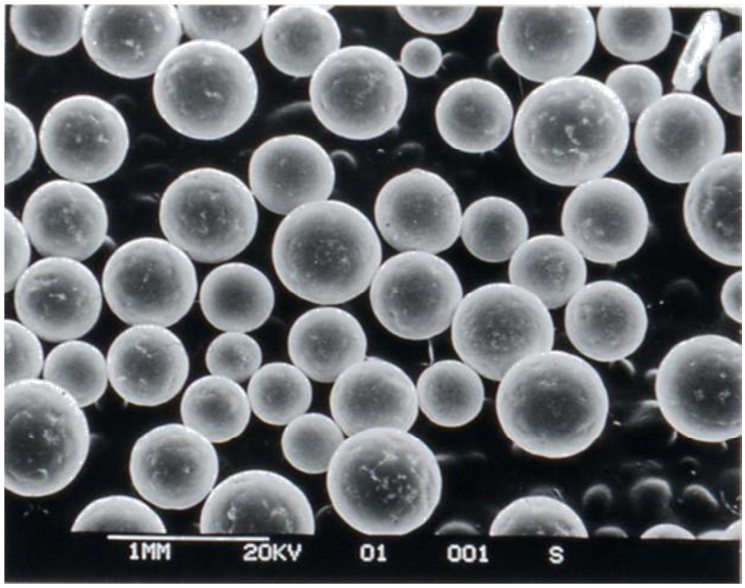

Figure 2.8. SEM image of IA copper powder that was atomized at 1200°C (run#060793) into a nitrogen atmosphere [2.39].

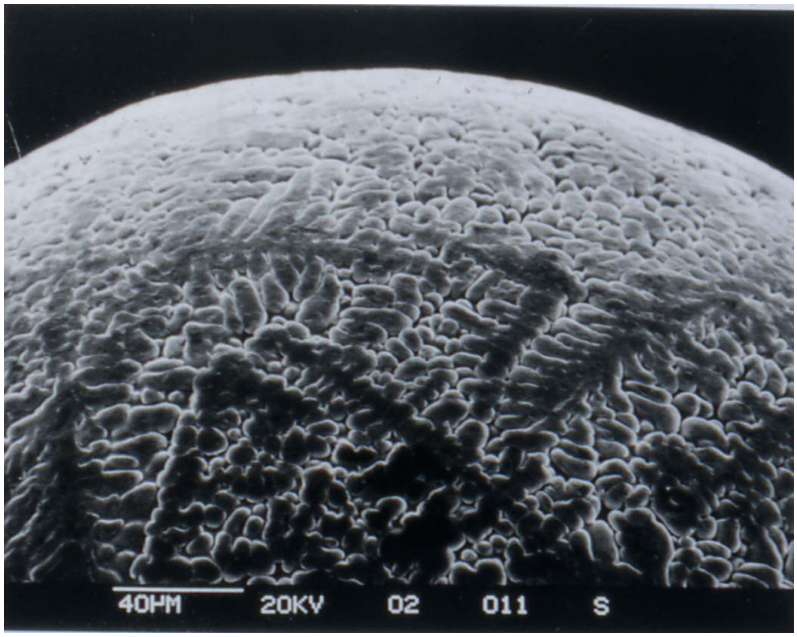

Figure 2.9. SEM image of a 475 µm IA-Al-17 wt% Cu powder that was atomized at 700°C (run#042893) into a nitrogen atmosphere [2.39].

2.9. Quantification of Microstructure

In this section the numerous methods utilized to identify the various phases in the microstructure and to quantify their relative amounts will be presented. The methods used range from the very well established methods such as image analysis on images from scanning electron microscopy (SEM) to state of the art techniques. With SEM images, a sufficient number must be taken in order to ensure that the result is representative of the structure of the sample being studied. State of the art methods include 3 dimensional (3D) x-ray micro-tomography and ND. For both special beam lines must be accessed in order to carry out the desired measurements. Subsequent to data collection of x-ray tomography from synchrotrons, rigorous image analysis must be carried out on large files (about 8 to 16 GB) representing the structure in micron sized particles. From these images, microstructural features such as dendrite trunks, nucleation sites, porosity and degree of microstructure anisotropy may be isolated and quantified as to scale, relative amount and location for example. For ND, Rietveld analysis is carried out to identify the phases present as well as their relative amounts.

2.9.1. Secondary dendrite arm spacing (SDAS)

Figure 2.10 shows a comparison of SDAS measurements done on different particle sizes obtained from different atomizing techniques. It is interesting to note that although Alcoa gas atomized powders and centrifugally atomized powders seemed to yield a similar relationship between dendrite arm spacing and

particle size, the powder generated using IA appears to have a finer structure than those from the other atomizing techniques. An etched cross section of an IA phosphorous bronze powder, Figure 2.11, clearly shows two regions having structures with different length scales. The finer scale structure must have formed under faster cooling or dendrite growth conditions than the coarser structure [2.31]. Quantifying the different phases and the scale of the structure is key to understanding the microstructure evolution under rapid solidification.

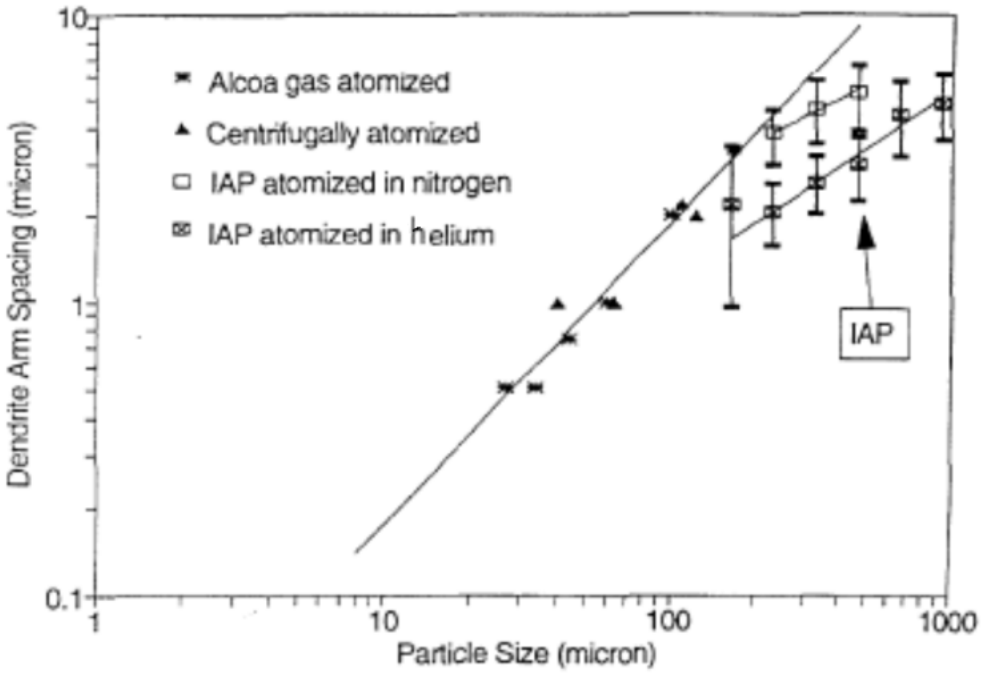

Figure 2.10. Comparison of the scale of the microstructure for difference atomization methods for an Al-Ni-Fe alloy [2.35].

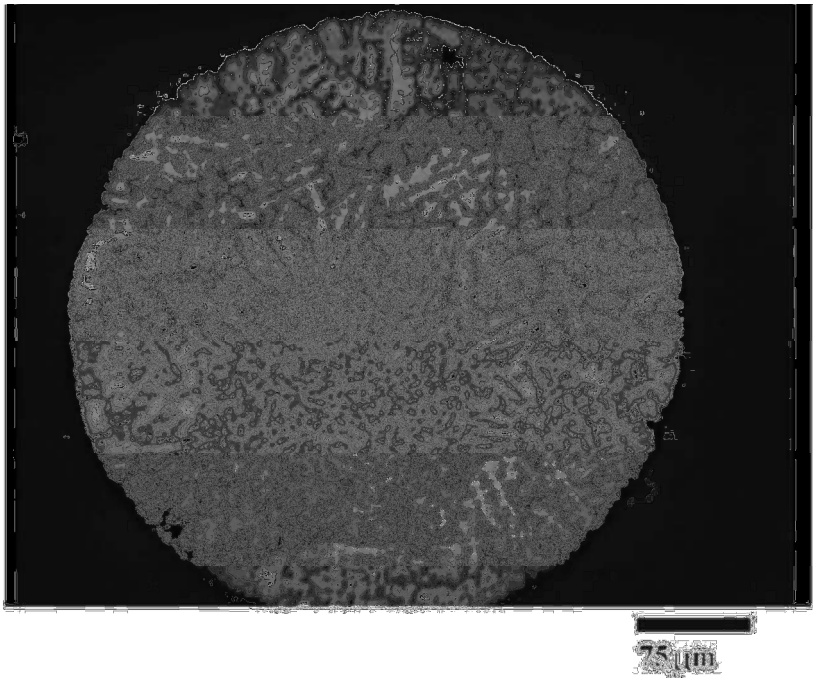

Figure 2.11. An etched cross section of an IA phosphorous bronze powder atomized in nitrogen at 950°C (971031). Two size scales of structure are evident [2.31].

The rate of cooling has been shown to be dependent on the particle size, cooling gas and the composition of falling droplets. Henein et al [2.34] studied the droplet solidification of IA Al-0.61wt%Fe and Al-1.9wt%Fe. Figures 2.12 and 2.13 show the cell spacing measurements as a function of the average particle size for both compositions atomized in nitrogen and helium atmosphere. The plots clearly show that powders atomized in helium have finer cell spacing than those atomized in nitrogen. Also, cell spacing in the alloys with higher iron content is smaller than that of the alloy with lower iron content. In addition, the gap between the two increases with increasing the particle size.

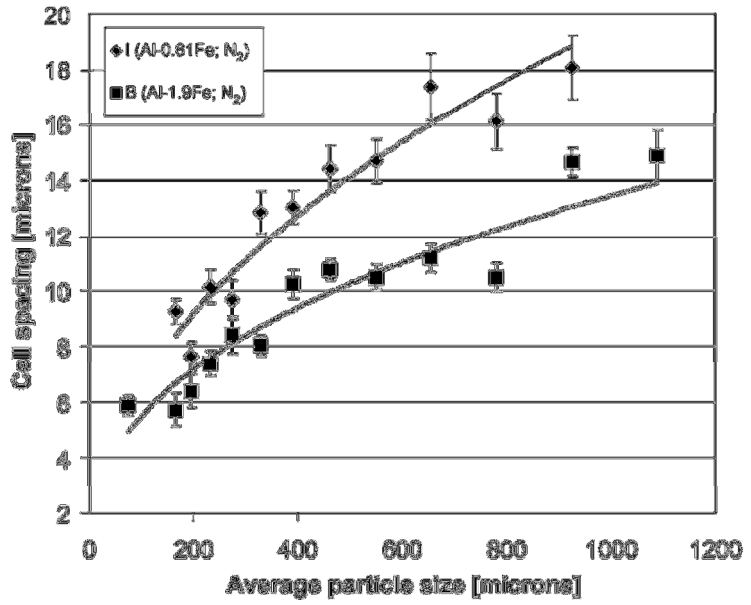

Figure 2.12. Effect of composition and particle size on the cell spacing for Al-0.61Fe and Al-1.9Fe alloys atomized in nitrogen [2.34].

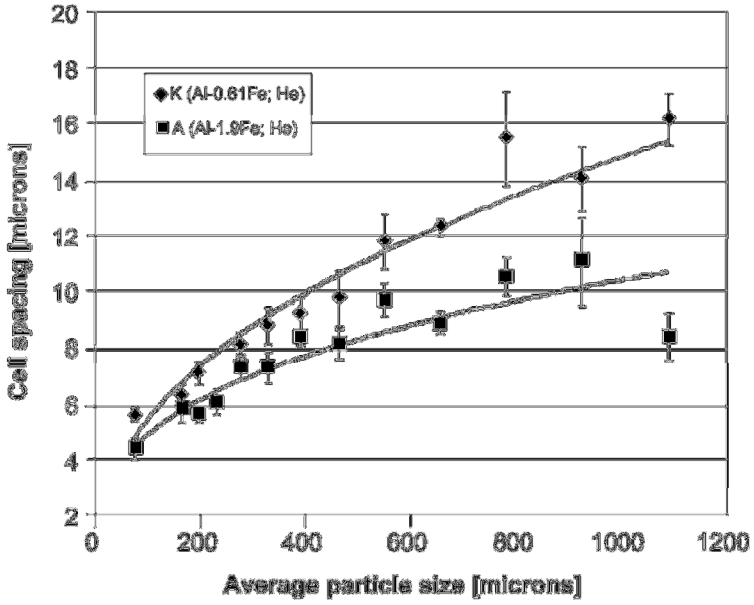

Figure 2.13. Effect of composition and particle size on the cell spacing for Al-0.61Fe and Al-1.9Fe alloys atomized in helium [2.34].

To better understand the solidification process of atomized droplets it is very important to utilize characterization techniques that can provide information about the whole volume of a droplet, or group of droplets. In the following two sections, applications of two important characterization techniques with such capabilities are discussed.

2.9.2. X-ray Micro-tomography

Microscopy can be used to gather information about solidification characteristics (e.g. cell spacing), but is constrained by the small number of sections that can be viewed from a given sample.

Analysis of solidification characteristics such as nucleation, recalescence, microsegregation and porosity formation in atomized droplets can be performed using a 3D visualization technique, which can provide information about the entire solidified volume. X-ray micro-tomography is a non-destructive technique that allows for gathering information from the entire sample volume. Hence, if a powder particle exhibits anisotropy in its structure such as shown in Figure 2.11, it will be clearly apparent using 3D X-ray micro-tomography, while using an SEM one would have to resort to a large number of samples of 2D cross-sections. Despite such efforts, a definitive determination of the microstructural evolution of a droplet cannot be made.

Henein et al. [2.34] used this technique to study the eutectic in the droplets of Al-0.61Fe and Al-1.9Fe. A sequence of images of a 550 μm droplet of Al-

0.61Fe from micro-tomography is shown in Figure 2.14. A single nucleation point for the entire droplet was identified very near the periphery of the surface of the droplet. The arrow in slice '1011' points to the nucleation point. Also clearly visible are the primary dendrites growing from the region of nucleation and initial growth. The lighter color represents the eutectic in the droplet. It can be seen that in some regions in the droplet a higher eutectic fraction has formed. This is evident by the various shades of color in the sequence of images. From the images it was found that there are two regions where there is a high concentration of eutectic. These regions are obviously those that were last to solidify in the droplet. This was determined by imaging both these regions of high eutectic concentration and the regions of porosity. The 3D rendering of these images were superimposed as seen in Figure 2.15 and were observed to be coincident.

Prasad et al. also investigated the solidification of Al-Cu using the tomography technique [2.36-37]. Observations were made on the droplet using X-ray beams of 1 μm resolution. X-Ray tomography was performed on the ID19 beam line at European Synchrotron Radiation Facility (ESRF) in Grenoble, France. Tomography was carried out on Al-5wt%Cu and Al-17wt%Cu atomized droplets 500μm in diameter. The X-ray tomography provided additional information about solidification that was not possible to get from conventional 2D techniques. Using tomography images it was possible to clearly locate the nucleation site, which was found to be within the droplet, as it can be seen in Figure 2.16. It must be noted that nucleation in IA is heterogeneous as the amount of oxygen in the system is high enough (more than 10 ppm) that can create oxide

layer on the surface, which will likely act as a surface to promote heterogeneous nucleation. This study also showed that none of the particles analyzed had multiple nucleation sites. This definitive conclusion illustrates one of the key advantages of the 3D micro-tomography technique over 2D visualization methods. Note that an additional advantage of 3D micro-tomography over serial sectioning techniques is that it is a non-destructive technique.

2.9.3. Neutron Diffraction

Bulk penetration by neutrons provides information about the entire volume of the droplet, whereas X-ray diffraction is primarily a near-surface analysis. Due to the anisotropy visible in powder structure observed in 3D micro-tomography, clearly 3D bulk diffraction information is required in order obtain a representative analysis of rapidly solidified samples.

Since a powder diffraction pattern is basically a set of peaks, some of which are overlapped and superimposed on a smooth and slowly varying background, a Rietveld refinement can be thought of as a very complex curve fitting problem. It uses a least squares approach to refine a theoretical line profile until it matches the experimental diffraction profile. In principle, the Rietveld method minimizes a function M (Eq. 2.2), which represents the difference between a calculated profile *y(calc)* and the observed profile *y(obs)* [2.40].

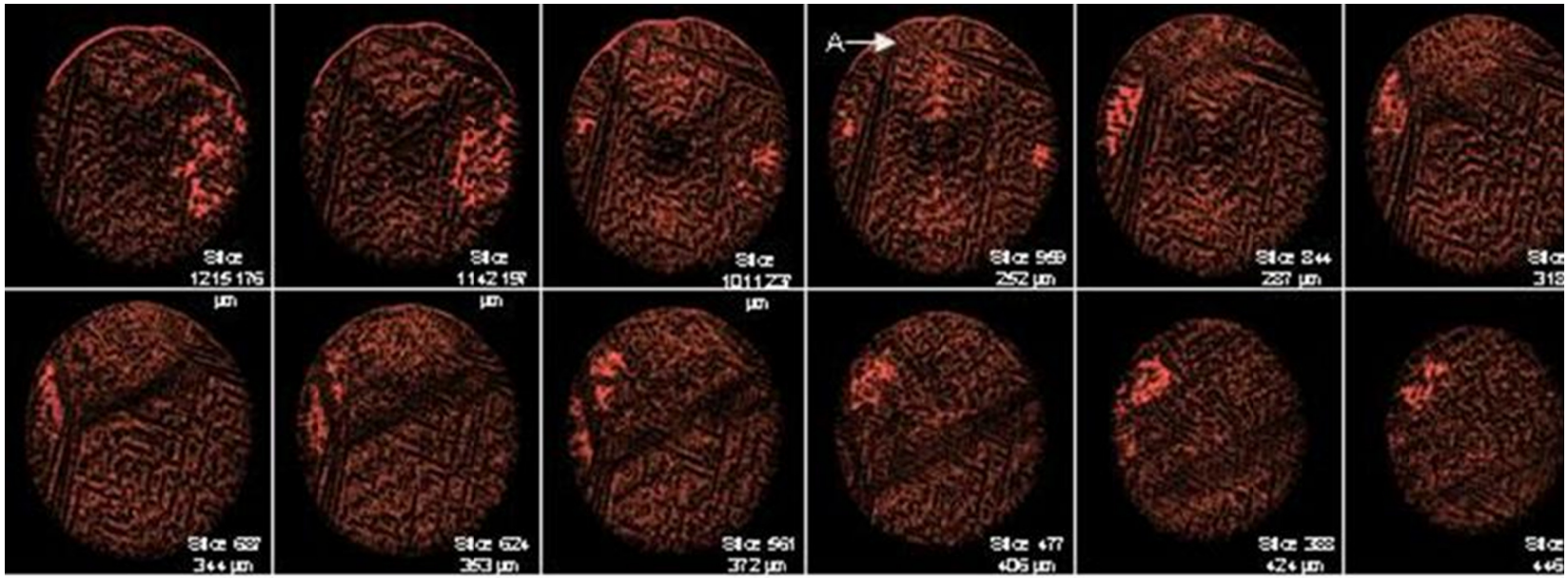

Figure 2.14. Tomographic images of Al-0.61Fe shown in a sequence of slices from of a 550 µm powder atomized in nitrogen. The lighter color in the particle represents the eutectic. Point A identifies the region where nucleation and initial growth was initiated [2.34]

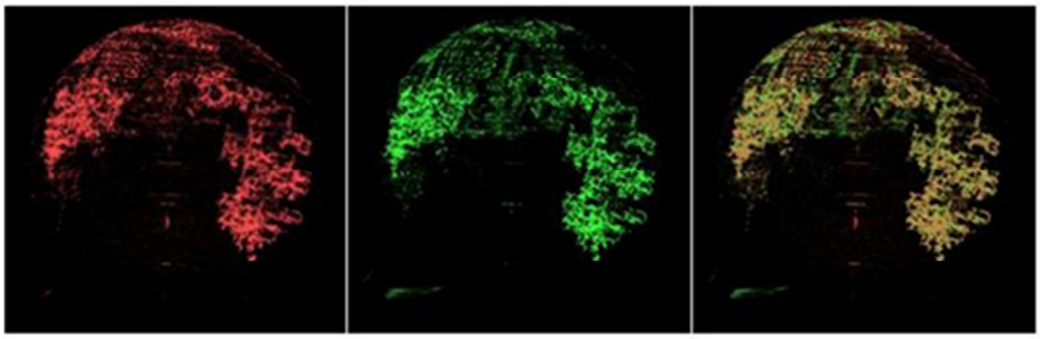

Figure 2.15. Full volumes of the 550 μm Al-0.61Fe particle highlighting the highest concentration of eutectic, porosity and a superimposition of eutectic and porosity [2.39].

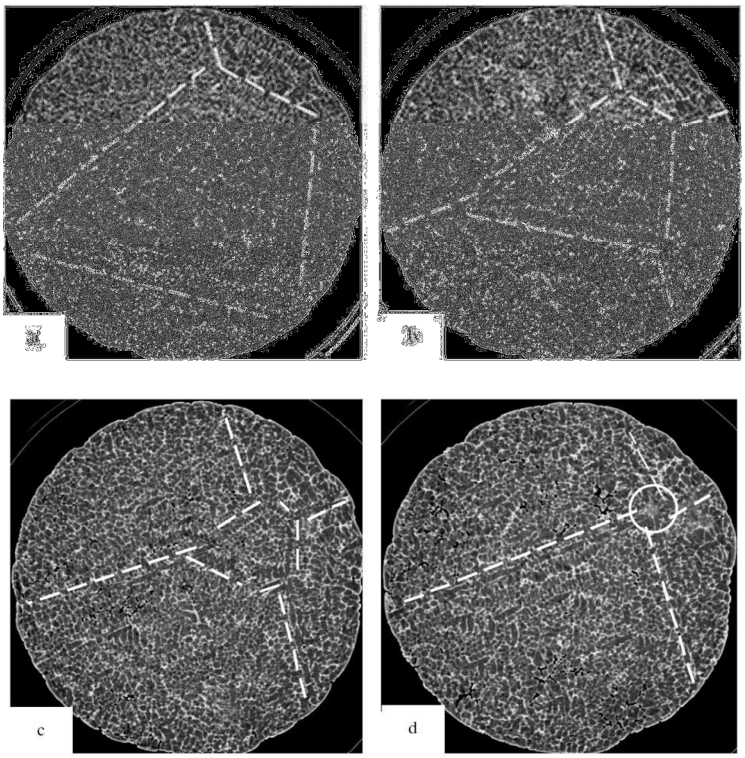

Figure 2.16. The progressive movement of a multiple equiaxed pattern (white dotted lines) converging to a nucleation site in Al5wt%Cu droplet. The encircled region in (d) shows the nucleation site. (a), (b), (c) and (d) are image numbers 430, 460, 495 and 520, respectively, out of a stack of 660 for a 660 μm Al5wt%Cu droplet viewed along the axial direction [2.36].

$$M = \sum_i W_i \left\{ y_i^{obs} - \frac{1}{C} y_i^{calc} \right\}^2 \quad (2.2)$$

where, W_i is weighting factor for each observation point.

A diffraction pattern includes information about peak position and intensity. With the development of Rietveld refinement techniques, quantitative phase analysis has become one of the most important applications of powder diffraction. For powders generated using IA, ND has been used for phase identification and phase quantification using Rietveld analysis.

Prasad et al. [2.41] quantified microsegregation for the rapid solidification of Al-Cu alloys. IA was used to generate Al-Cu alloys of three nominal compositions, 5 wt% Cu, 10 wt% Cu and 17 wt% Cu in nitrogen and helium gas. This quantification required application of Rietveld analysis on ND data that provided weight percent of $CuAl_2$, as well as calculation on SEM images that yields volume percent of eutectic. Using these data, it was possible to determine the weight percent eutectic. Figure 2.17 shows the variation of weight percent of eutectic as a function of alloy composition. Each data point represents a droplet size atomized in a given gas type, and therefore represents the effect of cooling rate. Solid data points represent He gas whereas the hollow points represent N_2. Scheil-Gulliver and equilibrium predictions are also presented in Figure 2.17. Clearly, there is a distinct relative decrease in microsegregation with increasing composition as seen by the increasing difference between experimentally determined amount of eutectic or $CuAl_2$ and the Scheil-Gulliver prediction.

Furthermore, there is only a small effect of cooling rate on the microsegregation and it is not as significant as the effect of alloy composition on microsegregation.

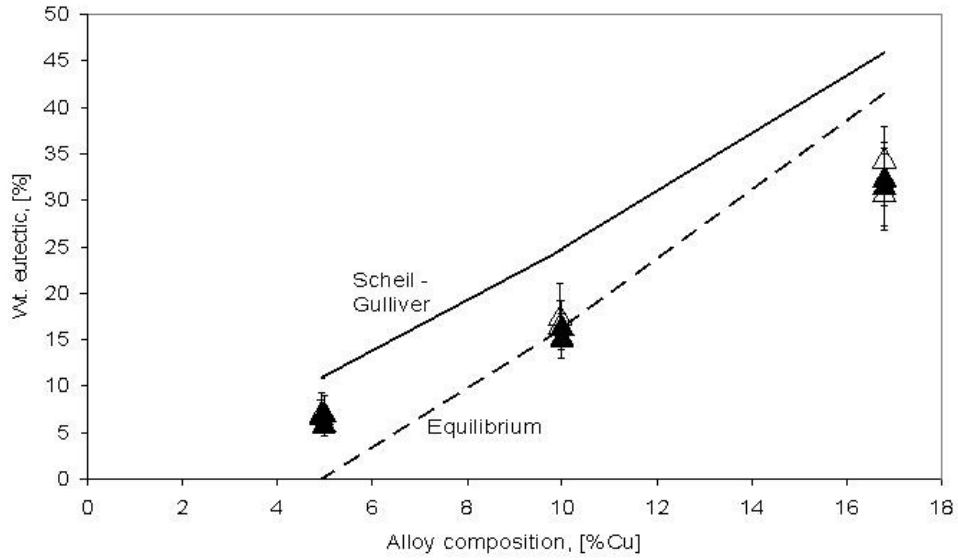

Figure 2.17. Weight percent eutectic in the atomized droplets as a function of alloy composition. Solid points, ▲, are for the He atomized droplets while the open points, Δ, represent droplets atomized in N_2 [2.41].

2.10. Thesis Objective

In light of the previous work discussed above, the IA technique was chosen as a method for creating rapidly solidified particles of peritectic alloys, specifically Al-Ni, to achieve the following goals:

- To characterize the phase formation and microstructure evolution during containerless rapid solidification of peritectic alloys

- To explore the effect of alloy composition on microstructural evolution
- To study the effect of cooling rate on phase fractions
- To study porosity formation within the solidifying droplets as a result of processing parameter and peritectic solidification

Al-Ni alloys are practically significant for their high temperature strength and heat resistance [2.42] and also for their catalytic capability [2.43]. While the peritectic reaction is still not very well understood, the aluminum-rich side of the aluminum-nickel alloy system with two peritectic reactions offers a valuable opportunity to understand this solidification phenomenon.

The outcome of this research will contribute to understanding the effects of cooling rate on microstructure evolution and phase fractions changes during solidification of alloys with one and two peritectic reactions, which have not been studied extensively. The advantage of the technique, IA, used for powder production in this research is that while it is a containerless processing technique, solidification occurs with very low disturbance from external forces; therefore, it allows for better understanding of processing parameters effects. Also, utilizing state of the art 3D characterization techniques, such as X-ray micro-tomography and ND, provides information about the entire volume of the solidified body, which has obvious advantages over conventional 2D characterization methods.

2.11. References

2.1. Kurz, W., Fisher, D. J., “Fundamentals of Solidification”, Trans Tech Publications, Switzerland, (1986).

2.2. Boettinger, W. J., Shechtman, D., Schaefer, R. J., Biancaniello, F. S., “The effect of rapid solidification velocity on the microstructure of Ag-Cu alloys”, Metallurgical Transactions A (Physical Metallurgy and Materials Science), Vol. 15A, No. 1, (1984), 55-66.

2.3. Prasad, A., Henein, H., Gandin, Ch.-A., “Microsegregation modeling of rapidly solidified Al-Cu droplets”, Modeling of Casting, Welding, and Advanced Solidification Processes-XI, TMS (The Minerals, Metals & Materials Society), (2006), 577-584.

2.4. Ha, H. P., Hunt, J. D., “A Numerical and Experimental Study of the Rate of Transformation in Three Directionally Grown Peritectic Systems”, Metallurgical and Materials Transactions A, Vol. 31A, (2000), 29-34.

2.5. Chen, S. L., Yang, Y., Chen, S. W., Lu, X. G. and Chang, Y. A., “Solidification Simulation Using Scheil Model in Multicomponent Systems”, Journal of Phase Equilibria and Diffusion, Vol. 30, No. 5, (2009), 429-434.

2.6. Chalmers, B., “Physical Metallurgy”, John Wiley & sons, Inc., New York, (1959), 271.

2.7. Dobler, S., Lo, T. S., Plapp, M., Karma, A., Kurz, W., “Peritectic Coupled Growth”, Acta Materiallia 52, (2004), 2795-2808.

2.8. Löser, W., Leonhardt, M., Lindenkreuz, H. G., Arnold, B., "Phase Selection in Undercooled Binary Peritectic Alloy Melts", Materials Science and Engineering A, Vol. 375-377, (2004), 534-539.

2.9. Chen, Y. Z., Liu, F., Yang, G. C., Liu, N., Yang, C. L., Zhou, Y. H., "Suppression of Peritectic Reaction in the Undercooled Peritectic Fe-Ni Melts", Scripta Materialia, 57, (2007), 779-782.

2.10. Biswas, K., Phanikumar, G., Chattopadhyay, K., Volkmann, T., Funke, O., Holland-Moritz, D., Herlach, D. M., "Rapid Solidification Behaviour of Undercooled Levitated Fe-Ge Alloy Droplets", Materials Science and Engineering A, Vol. 375-377, (2004), 464-467.

2.11. Herlach, D. M., Galenko, P., Holland-Moritz, D., "Metastable Solids from Undercooled Melts", Pergamon, (2007).

2.12. Reutzel, S., Hartmann, H., Galenko, P. K., Schneider, S. and Herlach, D. M., "Change of the Kinetics of Solidification and Microstructure Formation Induced by Convection in the Ni-Al System", Applied Physics Letters 91, 041913 (2007).

2.13. Hanlon, A. B., Matson, D. M. and Hyers, R. W., "Microgravity Experiments on the Effect of Internal Flow on Solidification of Fe-Cr-Ni Stainless Steels", Ann. N.Y. Acad. Sci. 1077: (2006), 33–48.

2.14. Volkmann, T., Loser, W., Herlach, D. M., "Nucleation and phase selection in undercooled Fe-Cr-Ni melts. II. Containerless solidification experiments", Metallurgical and Materials Transactions A 28(2) (1997)

461. Copyright Wiley-VCH Verlag GmbH & Co. KGaA. Reproduced with permission.

2.15. Vinet, B., Cortella, L., Favier, J. J., Desre, P., "Highly undercooled W and Re drops in an ultrahigh-vacuum drop tube", Applied Physics Letters 58(1) (1991) 97. Copyright Wiley-VCH Verlag GmbH & Co. KGaA. Reproduced with permission.

2.16. Van Zoest, T., Gaaloul, N., Singh, Y., Ahlers, H., Herr, W., Seidel, S. T., Ertmer, W., asel, E., Eckart, M. et al., "Bose-Einstein Condensation in Microgravity", Science 328 (5985) (2010) 1540. Copyright Wiley-VCH Verlag GmbH & Co. KGaA. Reproduced with permission.

2.17. Chen, L., Luo, X. H., "A new way to explore microgravity effect by drop tube experiment", Acta Metallurgica Sinica **43**(7) (2007) 769. Copyright Wiley-VCH Verlag GmbH & Co. KGaA. Reproduced with permission.

2.18. Perepezko, J. H., Sebright, J. L., Hockel, P. G., Wilde, G., "Undercooling and Solidification of Atomized Liquid Droplets", Materials Science and Engineering A, 326, (2002), 144-153. Copyright Wiley-VCH Verlag GmbH & Co. KGaA. Reproduced with permission.

2.19. Pryds, N. H., Pedersen, A. S., "Rapid Solidification of Martensitic Stainless Steel Atomized Droplets", Metallurgical and Materials Transactions, Vol. 33A, 12, (2002), 3755-3761. Copyright Wiley-VCH Verlag GmbH & Co. KGaA. Reproduced with permission.

2.20. J. Ziesenis, J. Tillwick, M. Krauss, V. Uhlenwinkel, Atomization: fundamentals and practice, eds. K.P. Cooper et al. (2000), TMS,

Warrendale, PA, p. 61. Copyright Wiley-VCH Verlag GmbH & Co. KGaA. Reproduced with permission.

2.21. Ting, J., Connor, J., Ridder, S., "High-speed cinematography of gas metal atomization", Materials Science and Engineering A-Structural Materials Properties Microstructure and Processing 390 (2005) 452. Copyright Wiley-VCH Verlag GmbH & Co. KGaA. Reproduced with permission.

2.22. Freyberg, A.V., Henein, H., Uhlenwinkel, V. and Buchholz, M., "Droplet solidification and gas-droplet thermal coupling in the atomization of a Cu-6Sn alloy", Metallurgical and Materials Transactions B 34 (2003) 243. Copyright Wiley-VCH Verlag GmbH & Co. KGaA. Reproduced with permission.

2.23. Kawasaki, A., Watanabe, R. and Kuroki, Y., "Preparation of monosized spherical powders of Pb-Sn alloy by pulsated orifice injection method", Powder Metallurgy World Congress, Editions de Physique, Fr., (1994) P. 365. Copyright Wiley-VCH Verlag GmbH & Co. KGaA. Reproduced with permission.

2.24. Miura, A., Dong, W., Fukue, M., Yodoshi, N., Takagi, K., Kawasaki, A., "Preparation of Fe-based monodisperse spherical particles with fully glassy phase", Journal of Alloys and Compounds, 509 (2011) 5581. Copyright Wiley-VCH Verlag GmbH & Co. KGaA. Reproduced with permission.

2.25. Liu, Q. and Orme, M., "On precision droplet-based net form manufacturing technology", Proceedings of the Institution of Mechanical Engineers, Part B: Journal of Engineering Manufacture 215 (2001) 1333. Copyright Wiley-VCH Verlag GmbH & Co. KGaA. Reproduced with permission.

2.26. Muntz, E. P. and Orme, M., "Charateristics, control and uses of liquid streams in space", AIAA Journal 25 (1987) 746. Copyright Wiley-VCH Verlag GmbH & Co. KGaA. Reproduced with permission.

2.27. Yim, P., Chun, J.-H., Ando, T. and Sikka, V. K., "Production and characterization of mono-sized Sn-Pb alloy balls", The International Journal of Powder Metallurgy 32 (1996) 155. Copyright Wiley-VCH Verlag GmbH & Co. KGaA. Reproduced with permission.

2.28. Yuan, D., "The novel Impulse Atomization Process", PhD thesis, University of Alberta (1997). Copyright Wiley-VCH Verlag GmbH & Co. KGaA. Reproduced with permission.

2.29. Morin, L. C., Reider, M., Meja, J. and Henein, H., "Impulse Atomization: A Novel Technique to Economically Produce Powders with a Desired Size Distribution", Advances in Powder Metallurgy & Particulate Materials, APMI, Princeton, NJ, (1996) 1-185.

2.30. Olsen, K., Sterzik, G. and Henein, H., "Upgrading Scrap Automotive Aluminum Alloys with the Impulse Atomization and Quench Technique", Third International Symposium: Recycling of Metals and Engineered Materials, P.B. Queneau and R.D. Peterson, Eds, TMS,

Warrendale, PA, (1995) 67. Copyright Wiley-VCH Verlag GmbH & Co. KGaA. Reproduced with permission.

2.31. Henein, H., "Single fluid atomization through the application of impulses to a melt", Materials Science and Engineering A 326 (2002) 92. Copyright Wiley-VCH Verlag GmbH & Co. KGaA. Reproduced with permission.

2.32. Ding, Y., Henein, H. and Fallavollita, J. A., "Methods and apparatus for producing droplets", US Patent 5,609,919 (1997); Canadian Patent 2,147,407 (2003). Copyright Wiley-VCH Verlag GmbH & Co. KGaA. Reproduced with permission.

2.33. Wiskel, J. B., Navel, K., Henein, H. and Maire, E., |Solidification study of aluminum alloys using Impulse Atomization: Part II. Effect of cooling rate on microstructure", Canadian Metallurgical Quarterly 41 (2) (2002) 193. Copyright Wiley-VCH Verlag GmbH & Co. KGaA. Reproduced with permission.

2.34. Henein, H., Buchoud, V., Schmidt, R.-R., Watt, C., Malakhov, D., Gandin, Ch.-A., Lesoult, G., Uhlenwinkel, V., "Droplet solidification of impulse atomized Al-0.61Fe and Al-1.9Fe", Canadian Metallurgical Quarterly 49(3) (2010) 275, Reproduced with permission of the Canadian Institute of Mining, Metallurgy and Petroleum. www.cim.org". Copyright Wiley-VCH Verlag GmbH & Co. KGaA. Reproduced with permission.

2.35. Ding, Y., Fallavollita, J., Henein, H. and Eadie, R., “On the Generation of Narrow Sized Droplets by the Impulse Atomization Process”, Recent Developments in Non-Ferrous Pyrometallurgy, I.A. Cameron and J.M. Toguri, eds., Metallurgical Society of CIM (1994) paper 49.4, Reproduced with permission of the Canadian Institute of Mining, Metallurgy and Petroleum. www.cim.org“. Copyright Wiley-VCH Verlag GmbH & Co. KGaA. Reproduced with permission.

2.36. Prasad, A., Henein, H., Maire, E. and Gandin, C. A. “X-ray tomography study of atomized al-cu droplets”, Canadian Metallurgical Quarterly, 43(2), (2004), 273-282, Reproduced with permission of the Canadian Institute of Mining, Metallurgy and Petroleum. www.cim.org“.Copyright Wiley-VCH Verlag GmbH & Co. KGaA. Reproduced with permission.

2.37. Prasad, A., Henein, H., Maire, E. and Gandin, C. A., “Understanding the rapid solidification of al-4.3Cu and al-17Cu using X-ray tomography”, Metallurgical and Materials Transactions A, 37(1) (2006) 249-257. Copyright Wiley-VCH Verlag GmbH & Co. KGaA. Reproduced with permission.

2.38. Delshad Khatibi, P., Ilbagi, A. and Henein, H., "In-situ measurement of cooling rate during solidification of Copper in a drop tube-impulse system", 4th International Symposium on Physical Sciences in Space (ISPS), July 2011, Bonn, Germany, Accepted for publication in J. Phys: Conf. Ser.

2.39. Prasad, A. and Henein, H., unpublished work. Copyright Wiley-VCH

Verlag GmbH & Co. KGaA. Reproduced with permission.

2.40. Rietveld, H. M., “Line profiles of neutron powder-diffraction peaks for structure refinement”, Acta Crystallographica, Vol. 22, 1967, 151-152.

2.41. Prasad, A., Henein, H. and Conlon, K. “Quantification of microsegregation during rapid solidification of al-cu powders”, Metallurgical and Materials Transactions A, 37(5) (2006) 1589. Copyright Wiley-VCH Verlag GmbH & Co. KGaA. Reproduced with permission.

2.42. Povarova, K. B., Lomberg, B. S., Filin, S. A., Kazanskaya, N. K., Shkol'nikov, D. Y. and Bespalova, M. D., “Structure and properties of Ni-Al-Co system (β+γ)- alloys”, Izvestia Akademii nauk SSSR. Metally, (1994), No. 3, 77-84.

2.43. Devred F, Reinhart G, Iles G N, Van D K, Adkins N J, Bakker J W, Nieuwenhuys B E, “Synchrotron X-ray microtomography of Raney-type nickel catalysts prepared by gas atomisation: Effect of microstructure on catalytic performance”, Catalysis Today, (2011) 163(1) 13-19.

Chapter 3

3. Experimental Procedures

Rapid solidification of the Al-Ni system with desired compositions, produced using a containerless solidification technique, was studied. Powders of Al-Ni alloys were produced using IA techniques. Then, the powders were washed, sieved into appropriate size range and were analyzed, either in the as-atomized form (for tomography and ND) or mounted, ground and polished for optical or electron microscopy. This chapter describes these experimental procedures in detail. The powder generation is described first. Following this, the details on SEM, X-ray micro-tomography and ND are described.

3.1. Impulse Atomization

In the previous chapter, a detailed description of IA was described. In this section more details about the probes and sensors installed on the atomization tower are given. Then, the experiments to produce Al-Ni samples are outlined.

Previously the most attractive benefits of on-line sizing and its application in gas atomization process control had been investigated [3.1-2]. It was shown that the implementation of on-line measurement tools can lead to decreased operating costs and to higher yields of powder in a target size range. Such measurements in an IA system, where the droplet-gas heat transfer may be

accurately characterized, can lead to valuable experimental data, which in turn can be used to validate the droplet solidification models.

Several different probes and sensors have been implemented to collect data from different parts of the atomization tube. Thermocouples read the temperature of the melt within the tundish and the gas within the tube. An oxygen sensor measures the amount of remaining oxygen in the tower. Two other probes measure the amplitude, acceleration and applied force of the moving plunger and a load cell at the bottom of the drop tube measures the mass flow rate. Also, a 3D translation stage was designed, constructed and installed in the drop tube to allow for measurements of radiant energy using a two-color pyrometer, DPV-2000 (Tecnar Automation Ltée), and velocity and droplet size in flight using a Shadowgraph (Sizing Master Shadow from LaVision GmbH in Gottingen, Germany). Figure 3.1 shows actual views of the translation stage designed for this experiment.

The importance of using these on-line measurement tools is that they provide valuable information regarding the actual changes in droplet radiant energy, which is a function of its temperature. In-situ characterization of falling particles is still underway. Some preliminary results have been published elsewhere [3.3], however, since these measurements have been performed on metals that are not studied in this dissertation, the reader is referred to the published article for more information. In the following sections, details of atomization runs and characterization performed are described.

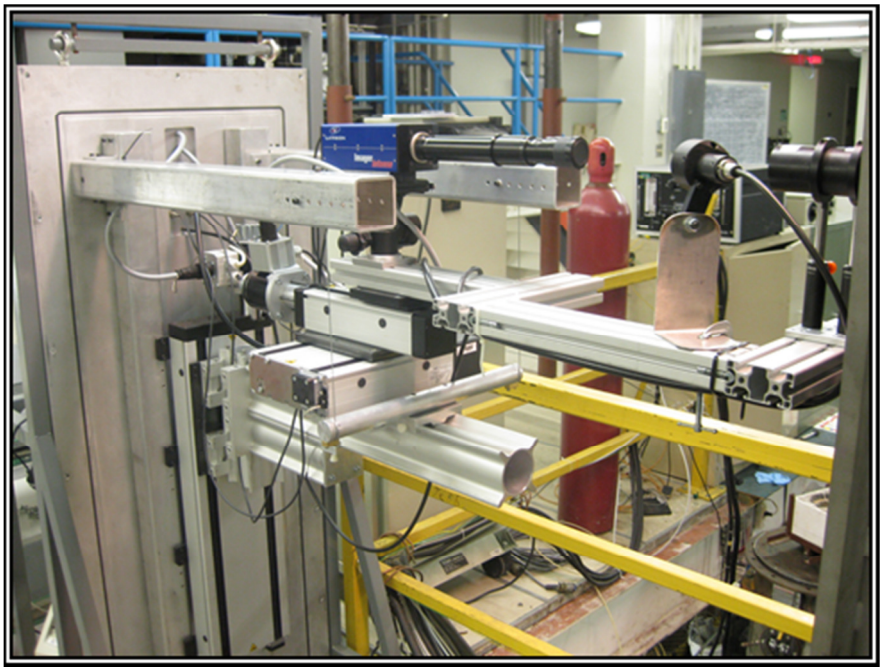

Figure 3.1. Actual view of the translation stage installed on the tower's door.

3.1.1. Melting and atomization

The IA runs were carried out to generate binary alloys of Al-Ni with two different nominal compositions: Al-36 wt%Ni and Al-50wt%Ni. For a desired alloy composition the appropriate weights of Al granules (99.9% pure) and Ni shots (99.9% pure) were mixed inside a zirconia coated graphite crucible. Typically, 500 grams of melt material were used in one run. Therefore, an Al-36 wt%Ni alloy would have 180 g of Ni and 320 g of Al inside the crucible. The nozzle plate at the bottom of the crucible was drilled with 37 holes with a diameter of 250 µm each. The crucible was then placed inside a copper coil, which was connected to an induction generator, at the top of the atomization tower. The atomization tower was then closed, sealed, evacuated and filled with nitrogen or helium. The oxygen

level within tower was reduced down to 10 ppm. The crucible was then heated until the entire load was melted. Each alloy was then kept at 100 K above its liquidus temperature for 30 minutes. An oscillating alumina plunger was used to push the molten alloy out of the nozzle plate's orifices. The amplitude and frequency of the plunger movement were controlled using a VR9500 Revolution VibrationVIEW Controller. The oscillation of the plunger results in ligaments of molten alloy exiting from the nozzle plate. These ligaments break and turn into small droplets that cool and solidify as they fall through the atomization chamber. The solidified droplets are collected in a beaker containing oil (Galden perflourinated fluid - HT230 supplied by Ausimont).

3.1.2. Powder washing, drying and sieving

The produced powder was washed in several cycles using toluene and ethanol to ensure the oil was removed from the surface of the powders. The powder was then placed on Whatman filter paper 2 (l25 mm diameter) to dry. It was then weighed and sieved according to ASTM E-11 specifications in a RO-TAP sieving machine. For sieving, a set of Gilson sieves with stainless still frame and steel wire grid was placed in RO-TAP for 20 minutes. Then, powders of different size range were weighed and placed in separate glass vials. Table 3.1 gives the atomization run conditions and the resulting average droplet size measured using sieve analysis.

Table 3.1. Alloy compositions and atomization conditions.

Atom. Run #	Atomization Gas /Temp.	Ni. (wt%)	Number of holes, Nozzle diameter (μm)	Average droplet size (μm)
080731	He/1673K	50	37, 250	436
080916	N2/1673K	50	37, 250	402
100920	He/1673K	50	37, 250	411
100908	N2/1673K	50	37, 250	419
080804	He/1373K	36	37, 250	343
100824	N2/1373K	36	37, 250	375

3.1.3. Characterization

3.1.3.1. SEM

Powders of desired size ranges were either used as-atomized for X-ray micro-tomography and ND or were mounted in epoxy for SEM imaging. The powder of interest, epoxy resin (West systems 10SA) and hardener (West Systems 20SA), with a ratio of 2.5:1, were mixed slowly so that minimal gas bubbles were formed. This mix was then poured into the plastic molds and was left for 1 hour for the epoxy mount to set. The mounted samples were then ground using 600 grit SiC paper. The next step was polishing that was done using 6 and 1 μm diamond slurry on soft cloth followed by final polishing using 0.5μm Al_2O_3 slurry. The polished samples were not etched. Optical microscopy was done using a Leica DM ILM and scanning electron microscopy was performed using Zeiss Evo MA15 SEM with 20 keV electron beam energy.

In order to compare the scale of microstructure in solidified samples, dendrite arm spacing measurements and cell spacing measurements were

performed. In the samples that clearly contained dendrites, see Figure 3.2 that shows microstructure of particles of Al-36 wt%Ni and Al-50 wt%Ni with diameter of 850 and 150 μm, respectively, lines were drawn parallel to the primary dendrite and then, distances between secondary dendrites at the places highlighted on the Figure 3.2 were measured using ImageJ 1.45h. This procedure was performed for at least 30 dendrites.

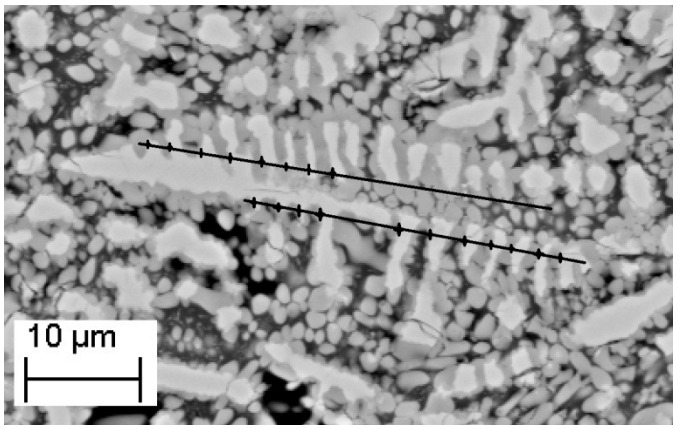

(a)

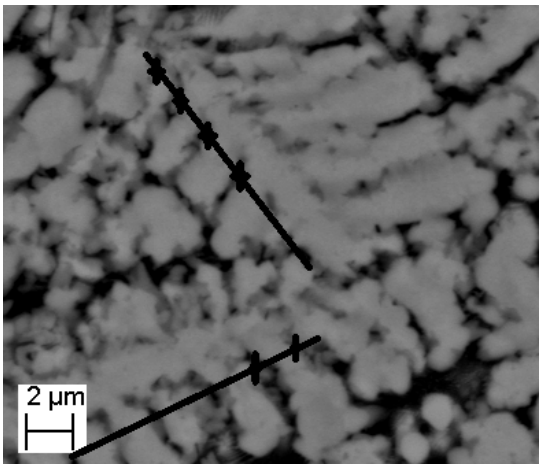

(b)

Figure 3.2. SDAS measurement on (a) particle of Al-36 wt%Ni with diameter of 850 μm, (b) particle of Al-50 wt%Ni with diameter of 150 μm.

In few samples, the number of distinguishable dendrites was so low that it was needed to use cell spacing measurement in addition to dendrite arm spacing measrurement. This was done by drawing tens of random lines within cells using software ImageTool version 3.0. The length of the drawn lines was automatically measured by the software and the average and standard deviation were calculated. Figure 3.3 shows an example of how the cell sizes were measured. The measured cell spacings were constantly compared with those from few SDAS measured on distinguishable dendrites in order to ensure the accuracy of the measurements.

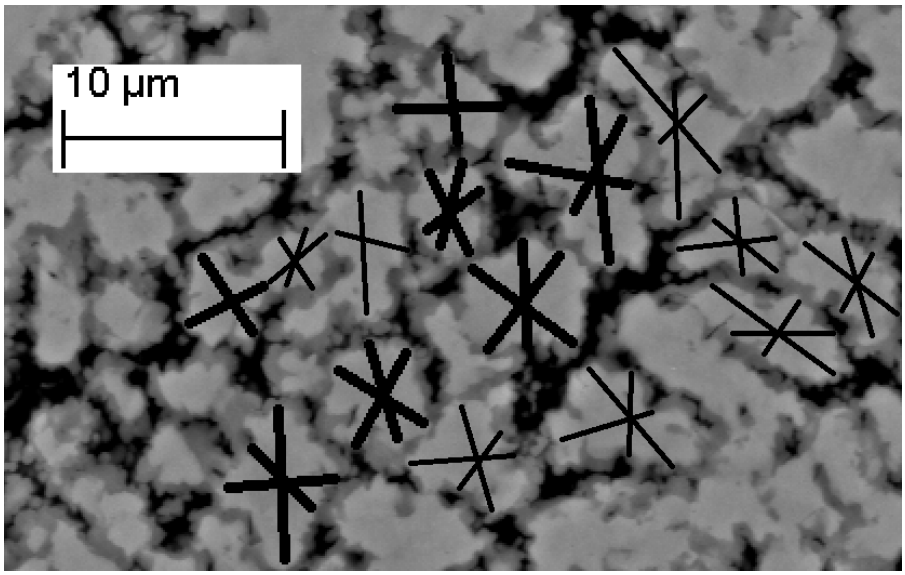

Figure 3.3. Cell size measurement in the sample with cell structure. A particle of Al-50 wt%Ni with 328 µm diameter.

3.1.3.2. X-ray micro-tomography

The working principle of micro-tomography is based on X-ray radiography. The local fluctuations of the X-ray absorbance create the contrast that is observed in a simple X-ray projection. A number of radiographs taken under different viewing angles are combined to reconstruct a 3D map of the local attenuation coefficient of the X-rays. A very high resolution stack of images, called slices, of the specimen is obtained by using an intense and highly energetic source. The experiments used in this work were performed on the ID19 beam line at the European Synchrotron Radiation Facility (ESRF) in Grenoble (France) (0.28 μm resolution) and on the beam line Tomcat, X02DA at Swiss Light Source, Paul Scherrer Institut, Villigen (Switzerland) (0.37 μm resolution). For these experiments, samples were poured into tiny capillary glass tube, which were held vertical to the surface of a disk using a thin vertical pin that was glued on one end to the disk and on the other end to the inside of the capillary glass tube.

High resolution stack of 2048 images with the size of 8 to 16 Giga Bytes were achieved. Appendix A describes details of pre-processing steps required for analysis of X-ray micro-tomography images.

3.1.3.3. Neutron diffraction

ND experiments were performed on the atomized droplets to gather information on the weight fraction of the phases exist in the solidified droplets. About 2-3 grams of powder from size range of interest were analyzed using ND. Neutrons are produced in a nuclear reactor and they are made to move at relativistic speeds.

When the neutron beam is focused on the sample, diffraction occurs from the atomic arrangements in the phases of the sample. Therefore, the diffraction patterns obtained from the neutron beam can be analyzed to achieve information regarding the phases present in the sample.

The ND experiments were conducted using a C2 neutron powder diffractometer located at National Research Council of Canada - Canadian Neutron Beam Centre (NRC-CNBC) in Chalk River, ON. C2 neutron powder diffractometer consists of an 800-wire BF3 detector that floats on an epoxy dance floor. A wavelength of 1.33 Å taken from a Si531 monochromator at 92.7 deg 2q were used for measurements. The powders were placed inside a vanadium can of 5-mm internal diameter, and 1 cm^3 volume. Samples were placed on a sample changer, consisting of a linear translator that was bolted to the sample table of the diffractometer. Beam-defining slits were used to illuminate only the sample volume. The aluminum posts were shielded with cadmium. These precautions ensure that the diffraction pattern is obtained only from phases in the analyzed sample. Rietveld analysis was then performed using the software GSAS (General Structure Analysis System) to find the weight fraction of different phases within the samples. For this analysis Crystallographic Information Files (i.e. ".cif" files) of AlNi, Al_3Ni_2, Al_3Ni and Al were used as model to perform diffraction pattern refinement. The steps taken in Rietveld refinement are as follows:

1. Scale parameter
2. Background
3. Lattice parameters of the phases

4. Peak shape
5. Position of the atoms in the lattice

In the next chapter the effect of cooling rate on the microstructure evolution, phase fractions and porosity formation in the IA particles of Al-36 wt%Ni will be discussed.

3.2. References

3.1. Kawasaki, A., Watanabe, R. and Kuroki, Y., "Preparation of monosized spherical powders of Pb-Sn alloy by pulsated orifice injection method", Powder Metallurgy World Congress, Editions de Physique, Fr., (1994) P. 365.

3.2. Miura, A., Dong, W., Fukue, M., Yodoshi, N., Takagi, K., Kawasaki, A., "Preparation of Fe-based monodisperse spherical particles with fully glassy phase", Journal of Alloys and Compounds, 509 (2011) 5581.

3.3. Ilbagi, A., Delshad Khatibi, P. and Henein, H., "In-situ measurement of cooling rate during solidification of Copper in a drop tube-impulse system", 4th International Symposium on Physical Sciences in Space (ISPS), July 2011, Bonn, Germany, Accepted for publication in J. Phys: Conf. Ser.

Chapter 4

4. Neutron diffraction and X-ray micro-tomography characterization of Al-36 wt% Ni[2]

4.1. Introduction

Peritectic solidification reactions appear in many metallic systems such as Al-Ni alloys. However, microstructural development and effects of processing parameters on phase selection during peritectic reaction are not well understood [4.1-2]. Al-Ni alloys are practically significant due to their high temperature strength, heat resistance and catalytic capability [4.3-4]. These capabilities are affected by solidification processing parameters, which also affect the amount and morphology of the solidified phases. For example, Devred et al. [4.4] showed that the best activity of Al-Ni catalysts for the hydrogenation of nitrobenzene and butyraldehyde is achieved when Al_3Ni/Al_3Ni_2 ratio in the precursor alloy, which was produced using gas atomization, is 2.3. Also, the grain size in the gas atomized precursor alloy that results in the best catalytic activity is between 106 and 150 µm [4.4].

To better investigate the effects of processing parameters during the solidification process it is very important to utilize characterization techniques that can provide information about the whole volume of the specimen. ND is a

[2] A major part of this chapter was published at ***Canadian Metallurgical Quarterly***, Vol. 50, No. 3, 2011, 295-302. Re produced with permission of Canadian Institute of Mining, Metallurgy and Petroleum. www.cim.org. Reformatted according to thesis requirements.
http://www.ingentaconnect.com/content/maney/cmq/2011/00000050/00000003/art00013

characterization technique that is used to obtain information from the bulk of a specimen. In this technique, 3D bulk diffraction information enables phase identification and phase quantification using Rietveld analysis. Effects of processing parameters on the phase fractions formed during the solidification of atomized particles of Al-Ni alloys have been investigated using ND [4.5]. In this chapter, the effect of cooling rate on microstructure, phase fractions and metastable phase formation in Al-36 wt%Ni will be discussed.

A 3D technique was used for microstructural characterization of IA particles. Microscopy can be used to gather information about solidification characteristics like cell spacing and micro segregation (using quantitative metallography), but is constrained by the small number of sections that can be viewed from a given sample. Analysis of solidification characteristics such as nucleation, recalescence, microsegregation and porosity formation can be performed using X-ray micro-tomography. This non-destructive technique, which can provide information about the entire solidified volume, has been extensively used to study porosity formation and microstructure evolution of IA particles of Al-Cu [4.6-7], Al-Fe [4.8] and Al-Si [4.9] alloys. In this Chapter, X-ray micro-tomography is used to analyze the rapid solidification and porosity formation of IA Al-36 wt%Ni alloy.

Due to similarity of X-ray absorbance of Al_3Ni_2 and Al_3Ni, it is difficult to distinguish these phases in X-ray micro-tomography images. In this chapter, a new method will be introduced that may be used for phase fraction analysis from X-ray micro-tomography images.

4.1.1. Solidification Path

St John and Hogan [4.10] in 1987 showed that the composition gradient within the peritectic phase would strongly influence the rate of peritectic transformation. Based on their analysis, a peritectic reaction is extremely slow when the product is of fixed composition or has very narrow homogeneity range. This is the case for Al_3Ni. This intermetallic has a fixed composition at 42 wt% Ni, rendering its formation from the peritectic reaction at 854 ºC very sluggish. In such cases, the undercooling and/or high cooling rates can result in metastable conditions. This metastability may occur in the form of a new phase, different proportions of phases or higher solute content. The following sections describe the solidification path of Al-36wt%Ni using equilibrium phase diagram and Scheil-Gulliver model.

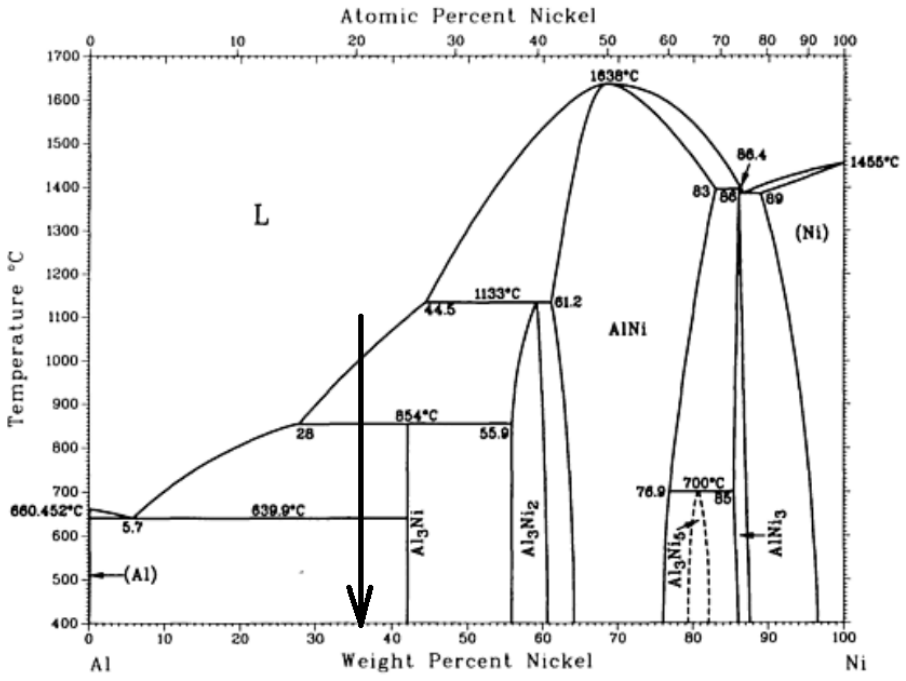

Figure 4.1. Al-Ni phase diagram [4.13].

4.1.1.1. Equilibrium

The equilibrium phase diagram, Figure 4.1, shows that during cooling of an alloy with the composition of Al-36 wt%Ni, Al_3Ni_2 forms as the primary phase. It then goes through the peritectic reaction at 854 ºC, where it is expected to transform entirely to Al_3Ni. The remaining liquid solidifies in a eutectic reaction into Al and Al_3Ni. The resulting composition at the end of equilibrium solidification, as predicted by the phase diagram, must contain almost 85 wt% Al_3Ni and 15 wt% Al and no primary Al_3Ni_2.

4.1.1.2. Scheil-Gulliver Equation

The Scheil-Gulliver equation is used to describe solute redistribution during solidification of an alloy. This model assumes perfect mixing in liquid and no diffusion in solid to predict solute distribution during solidification. However, for example, in the case of Al-36 wt%Ni, the initial reaction of the liquid with the pro-peritectic phase, Al_3Ni_2, would leave an envelope of the peritectic product, Al_3Ni, around the primary phase, Al_3Ni_2. Further transformation requires the diffusion of Ni through Al_3Ni envelope. This does not follow the Scheil-Gulliver assumption. Hence, the peritectic reaction does not proceed in the simulation of solidification using a Scheil-Gulliver model. Therefore, the fraction of the peritectic product, Al_3Ni, predicted by the Scheil-Gulliver equation, will be an underestimation of the Al_3Ni phase fraction produced during equilibrium cooling. However, in some cases this might be a good estimate. In this chapter, the extent

to which the Scheil-Gulliver equation can predict the phase fractions in Al-36 wt%Ni will be investigated by comparing the phase fractions measured using ND with those calculated by the Scheil-Gulliver equation.

To calculate the phase fractions using Scheil-Gulliver model, in the case of Al-36 wt%Ni, at 854 ºC the fractions of solid (Al_3Ni_2) can be calculated using Eq 4.1.

$$C_s=kC_0(1-f_s)^{k-1} \quad (4.1)$$

where C_s is the composition of solid, k is partition coefficient, C_0 is the overall composition of alloy and f_s is the fraction of solid formed. The same calculation can be performed at 639.9 ºC. From these calculations, the ratio of Al_3Ni to Al_3Ni_2 for Al-36 wt% Ni is 1.74.

4.1.2. Al_3Ni_2 Lattice Parameter

In this chapter, the effect of cooling rate and composition on the lattice parameter of Al_3Ni_2 is also investigated.

It is known that the Al_3Ni_2 structure is similar to that of AlNi structure with 33% of the nickel sites vacant at the stoichiometric composition. The vacancies are ordered in a way that every third sheet of nickel atoms perpendicular to one of the three-fold axes of the cube is absent. The unit cell of AlNi and the process of its transformation to Al_3Ni_2 is shown in Figure 4.2[3]. This

[3] Images were generated using CrystalMaker®: a crystal and molecular structures program for Mac and Windows. CrystalMaker Software Ltd, Oxford, England (www.crystalmaker.com).

ordering transforms the crystal structure from cubic to rhombohedral by unequal changes of the parameters *c* and *a* [4.11]. The cube diagonal in AlNi becomes the *c* axis in Al_3Ni_2 ($c = a'\sqrt{3}$, where a' is the cube edge) and the cube face diagonal becomes *a* axis of Al_3Ni_2 unit cell ($a = a'\sqrt{2}$). Therefore, it is expected that the axial ratio will be *c/a*=1.225. However, due to the collapse along the *c* axis, as a result of the missing planes, it drops to 1.2132 at stoichiometric Al_3Ni_2 [4.12]. Taylor and Doyle also showed that the *c/a* ratio falls continuously across the phase with increasing aluminum content of Al_3Ni_2 [4.12].On the other hand, Bao et al [4.5] showed that the stoichiometric amounts of aluminum and nickel in Al_3Ni_2 are sensitive to the cooling rate. They applied Rietveld refinement to neutron and X-ray diffraction patterns from gas atomized powders to show that by decreasing particle size from 500 μm to 25 μm, which corresponds to increasing cooling rate, the ratio of Al/Ni decreases. However, the effect of cooling rate on the lattice parameter of Al_3Ni_2 has not yet been established very well.

In this work, the lattice parameters ratio of Al_3Ni_2 was measured using the Rietveld refinement on ND patterns and the effect of cooling rate on *c/a* ratio at two different compositions, Al-36 wt%Ni and Al-50 wt%Ni, will be discussed.

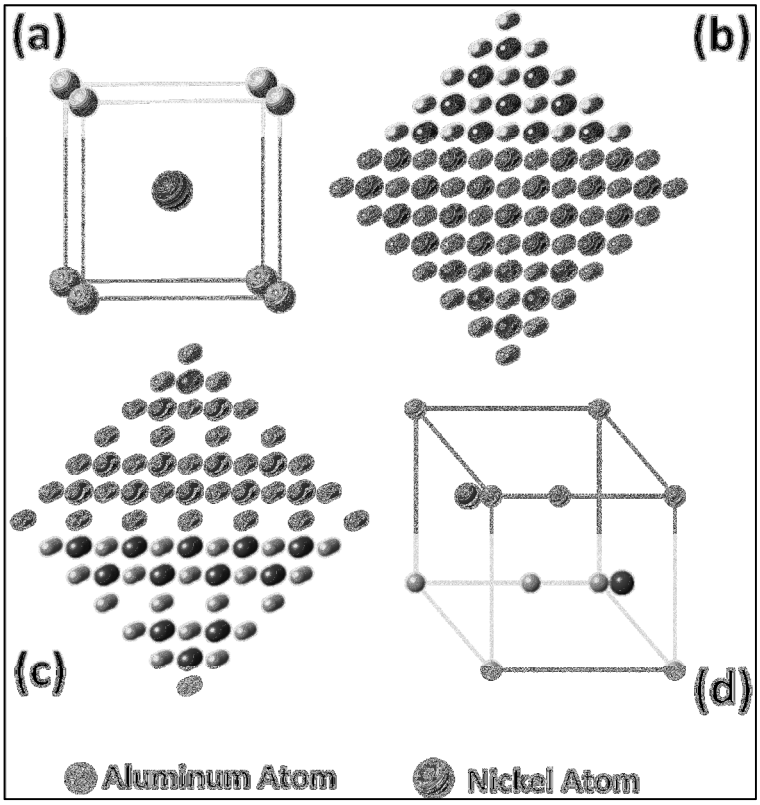

Figure 4.2. (a) Unit cell of AlNi, (b) several unit cells of AlNi, (c) formation of Al_3Ni_2 from AlNi by removing every third sheet of nickel atoms perpendicular to one of the three-fold axes of the cube, (d) unit cell of Al_3Ni_2 The difference in size of aluminum and nickel atoms was dictated by the drawing software and has no scientific meaning.

4.2. Experimental

A 4-meter-high drop tube was filled with inert gas and the oxygen content was reduced to less than 10 ppm. An induction furnace located at the top of the drop tube then started heating the 99.9% pure Al and Ni (Alfa Aesar) to make Al-36 wt%Ni melt. The alloy was held for 30 minutes at 100 K above its liquidus

temperature. Afterwards, the liquid was pushed through orifices at the bottom of the crucible to generate liquid streams, which subsequently broke up into spherical droplets by Rayleigh instability. The droplets lose their heat as they fall through the stagnant gas atmosphere. For the details of the technique see [4.14]. The solidified particles were subsequently washed and sieved into different sizes. See Table 3.1 for run conditions and average particle sizes.

To study the microstructure, scanning electron microscopy was performed using a Zeiss Evo MA15 SEM with a 20 keV electron beam energy. ND was used to characterize the phases formed during solidification. The experiments were conducted using a neutron beam of 1.33 Å wavelength at National Research Council of Canada - Canadian Neutron Beam Centre (NRC-CNBC) in Chalk River, ON. To obtain the weight fraction of the phases formed under different conditions, Rietveld analysis was performed using the GSAS (General Structure Analysis System) software [4.15].

The micro-tomography experiment was performed at the beam line Tomcat, X02DA at Swiss Light Source, Paul Scherrer Institut, Villigen, Switzerland with resolution of 0.37 μm.

4.3. Results and discussion

4.3.1. SEM

Figure 4.3 shows two Al-36 wt%Ni particles of different sizes, atomized in helium. Three different gray scales representing three different phases can be seen

in these images. EDX analysis of the white phase observed in the core of dendrites showed that it contains 39 at% nickel, which is close to that of Al_3Ni_2. These dendrites are surrounded by a light gray phase. From EDX it was found that this phase contains 24 at% nickel. The morphology and the composition of this phase suggest that it is the peritectic product, Al_3Ni. The dark gray structure, which contains more than 95 at% aluminum is the eutectic that formed during the last stage of the solidification.

Comparing the scale of these microstructures shows that the smaller the particle, the finer the microstructure. Figure 4.4 shows the SDAS of different particle sizes of Al-36 wt%Ni atomized in helium and nitrogen. Also, it is evident that decreasing particle size also resulted in finer microstructure.

Kurz and Fisher [4.16] showed that the SDAS (λ) is proportional to the cube root of solidification time (t) as it is a function of the extent of coarsening that occurs during solidification (see Eqs. 4.2 and 4.3).

$$\lambda = 5.5(\mathrm{Mt})^{\frac{1}{3}} \tag{4.2}$$

with

$$\mathrm{M} = \frac{\mathrm{D}\Gamma \ln\left(\frac{\mathrm{C}_l^{\mathrm{m}}}{\mathrm{C}_0}\right)}{\mathrm{m}(1-\mathrm{k})(\mathrm{C}_0 - \mathrm{C}_l^{\mathrm{m}})} \tag{4.3}$$

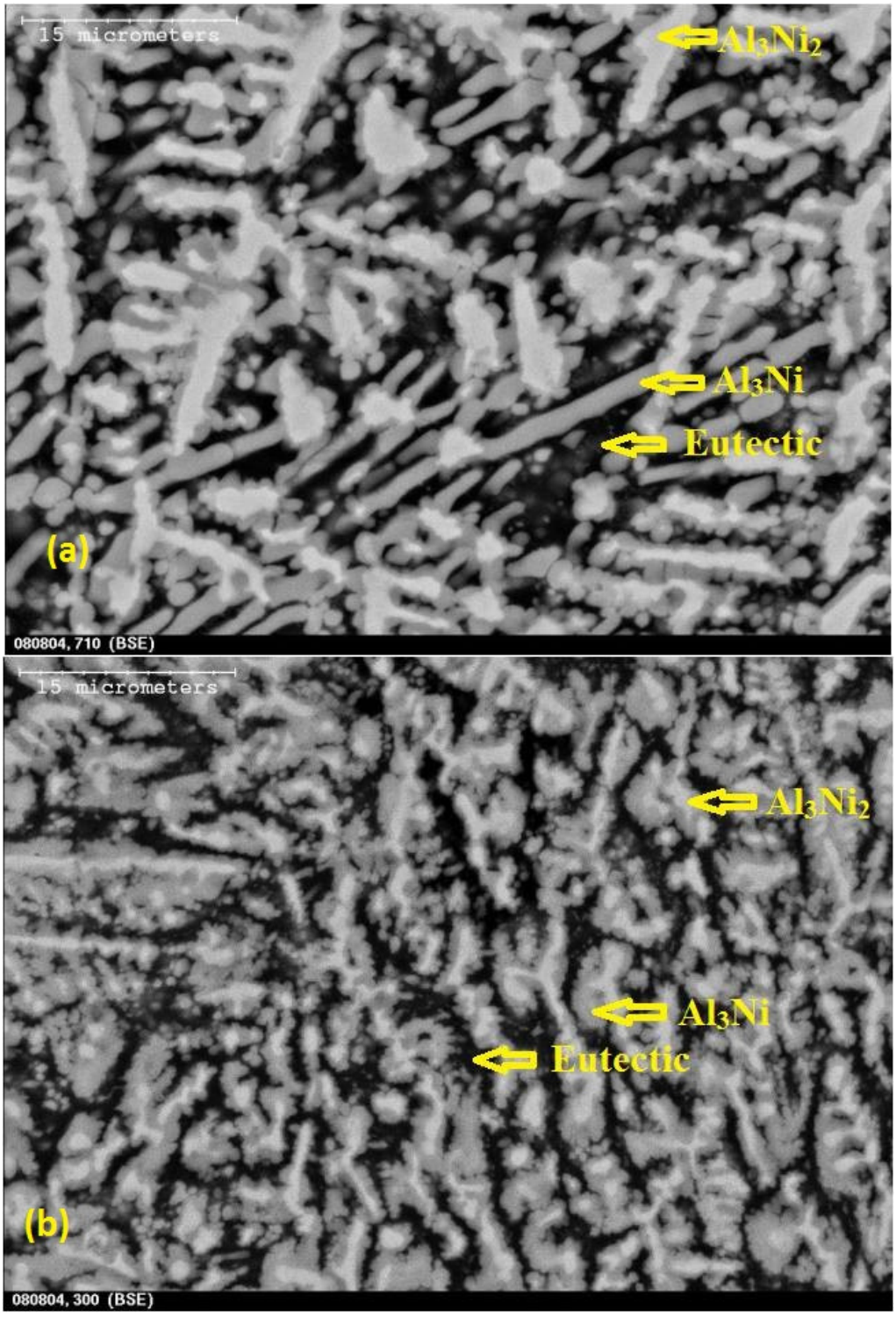

Figure 4.3. Two particles of Al-36 wt%Ni atomized in helium: (a) particle size: 780 μm and (b) particle size: 328 μm.

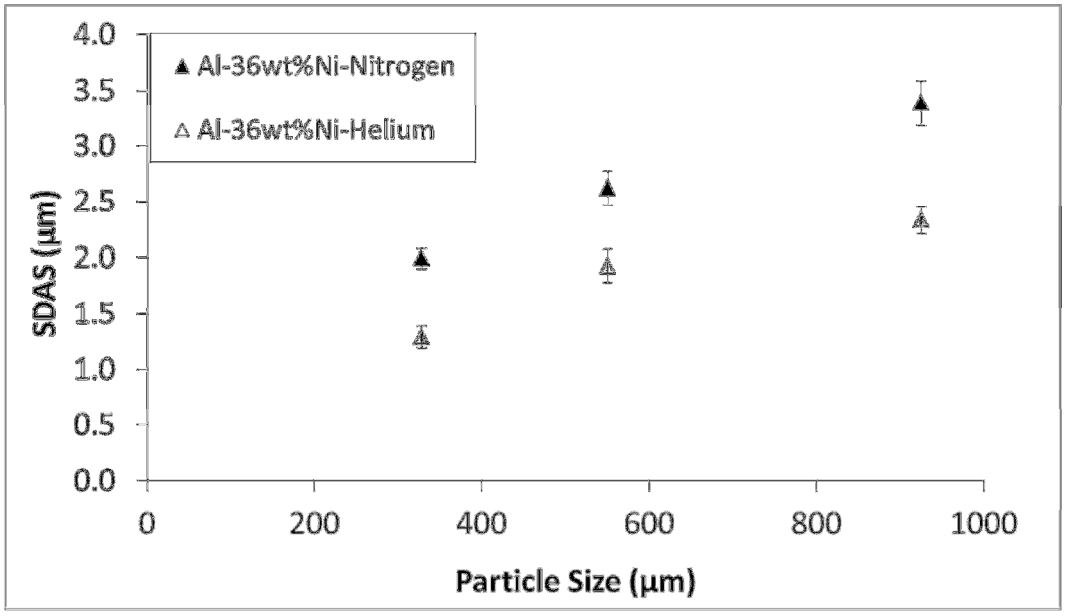

Figure 4.4. Effect of particle size, gas type and composition on the SDAS.

where Γ is the Gibbs-Thomson coefficient, D is the diffusion coefficient of solute in the liquid, m is the slope of the liquidus line (prior to peritectic reaction), k is partition coefficient, C_l^m is the composition of the last liquid to solidify and C_0 is the overall composition. Except for Γ and D, the rest of the parameters in Eq. 4.3 can be found from the phase diagram, where it was assumed that the liquidus line is linear. Also from [4.17] for Al-Ni system, $\Gamma=1\times10^{-8}$ mK and D= 1×10^{-8} m^2s^{-1}. The accuracy of the values used for Γ and D will be addressed in chapter 6.

Using the calculated values of M, the measured SDAS and Eq. 4.2 the solidification time of the primary phase can be calculated. It is assumed that the dendrite arm coarsening has generally occurred before the first peritectic reaction takes place. Dividing the solidification range of the primary phase by the

calculated solidification time gives the primary phase cooling rate. The measured SDAS as a result of different cooling rates was plotted in Figure 4.5. It can be seen that the particles atomized in helium, which results in finer structure, have experienced higher cooling. From Figure 4.4 the SDAS can be related to the cooling rate using Eq. 4.4.

$$\lambda = 69.58\dot{T}^{-0.33} \tag{4.4}$$

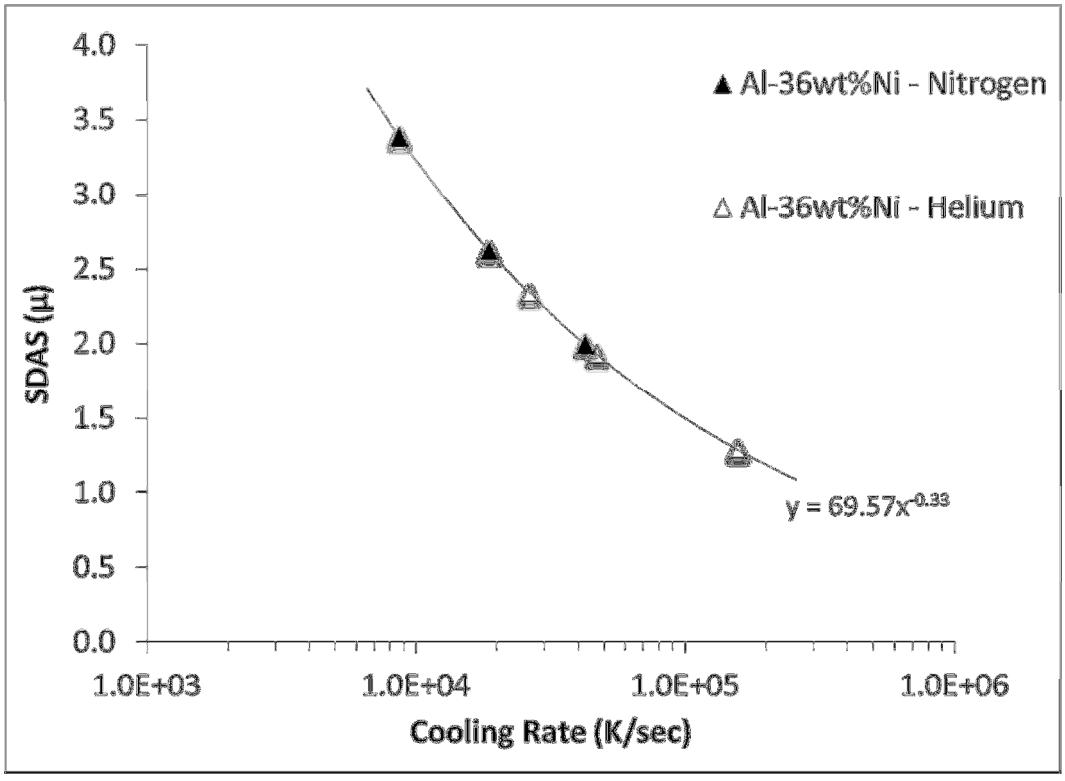

Figure 4.5. The calculated cooling rate of Al-36 wt%Ni, atomized both in helium and nitrogen.

Particles of Al-36 wt%Ni with diameters smaller than 180 µm were found to have a very different microstructure than those observed in Figure 4.3. Figures 4.6 shows the microstructure of an IA particle of Al-36 wt%Ni with diameter of 165 µm. Only two shades of grey color can be identified. The EDX analysis showed that the phase with lighter grey color is Al_3Ni and the darker grey color is the eutectic structure. Considering the increase of cooling rate as a result of decreasing particle size, it seems that the formation of Al_3Ni_2 may be suppressed at high cooling rates. This will be further investigated in this chapter.

Figure 4.6. Al-36 wt%Ni particle with diameter of 165 µm cooled in helium.

4.3.2. Neutron Diffraction

Profile refinement was carried out using the software GSAS on ND patterns from particles of Al-36 wt%Ni atomized in helium and in nitrogen. Three phases (i.e. Al_3Ni_2, Al_3Ni and Al) were identified. Figure 4.7 shows an example of measured ND pattern of 5 grams of IA particles with diameter of 500 μm along with the calculated diffraction pattern. The top line shows the calculated diffraction pattern as obtained from GSAS software and the bottom line represents the difference between the observed and calculated diffraction pattern. The few and low oscillation peaks in this curve indicate a satisfactory agreement between measured and refined patterns.

The weight fraction of each phase was then calculated from Rietveld refinement to investigate the effect of cooling rate on the phase fractions after solidification. Figure 4.8 shows the ratio of Al_3Ni to Al_3Ni_2 as a function of cooling rate for the particles atomized in helium. Since no Al_3Ni_2 was found in the sample with particle size smaller than 180 μm, it is not shown in Figure 4.8. It appears that the ratio decreases and approaches Scheil-Gulliver's prediction as the cooling rate decreases.

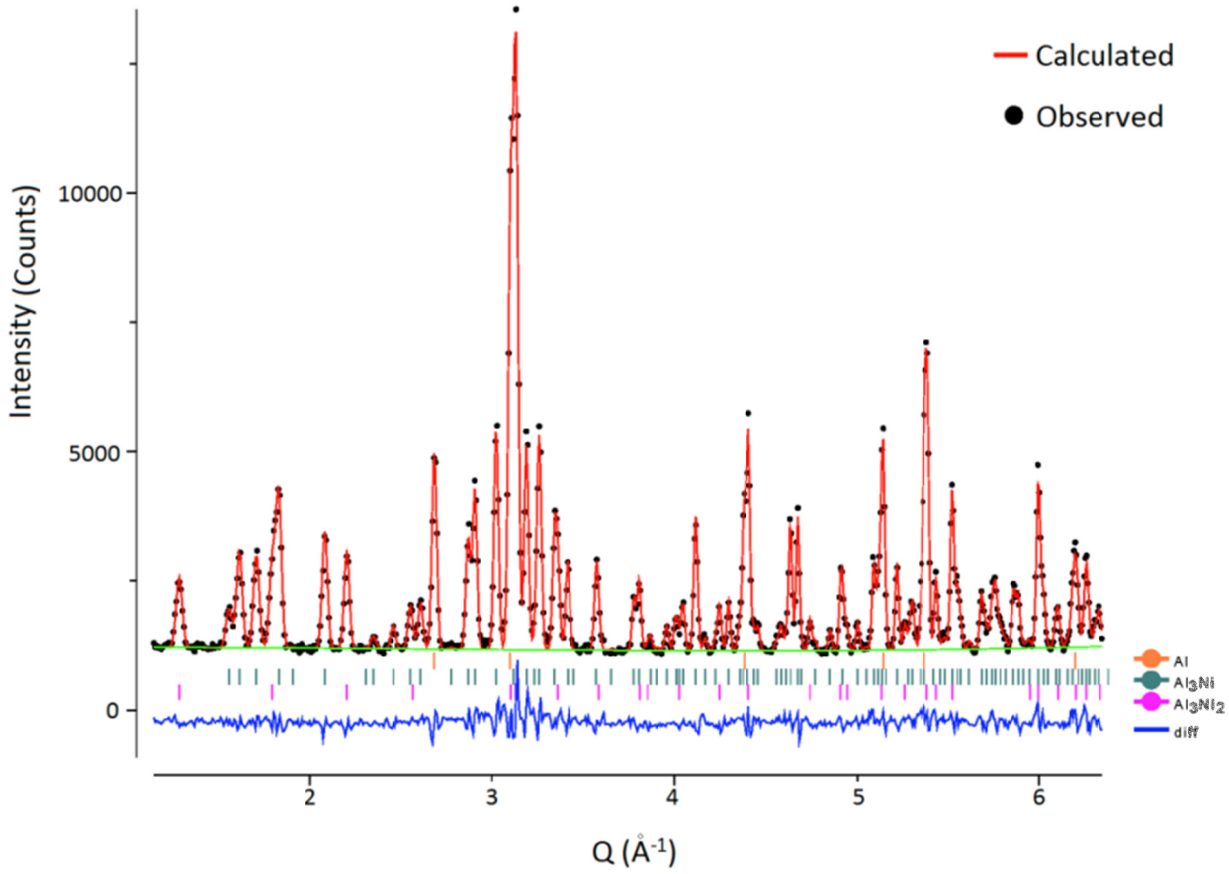

Figure 4.7. Profile refinement of Al-36 wt%Ni with the diameter of 500 μm using the GSAS computer code. The top line shows the calculated diffraction pattern as obtained from GSAS software and the bottom line represents the difference between the observed and calculated diffraction pattern. The small vertical bars indicate the positions of diffraction peaks of the Al (top), Al_3Ni (middle) and Al_3Ni_2 (below). wRp=%5.61, χ^2=6.63.

Since the overall composition for this alloy is very close to the liquidus line, increasing cooling rate reduces the time available for Al_3Ni_2 nucleation and growth to a point at which Al_3Ni_2 does not form as the primary phase any more (Figure 4.6). Generally, for the IA droplets of Al-36 wt%Ni, the cooling rate is so high that it is very unlikely that any time-dependent process (e.g. diffusion) can advance. Also, approaching to Scheil-Gulliver's prediction, which assumes no solid state diffusion, at lower cooling rates shows that the diffusion was not responsible for the observed phase selections. Therefore, it is suggested that the main parameter that affects the Al_3Ni/Al_3Ni_2 ratio is the solidification interval of the primary phase Al_3Ni_2 which will vary with primary phase undercooling. In the range of cooling rates studied in this chapter, lower cooling rate allows for further growth of Al_3Ni_2. Since peritectic reaction requires solid state diffusion, the primary Al_3Ni_2 can hardly transform to Al_3Ni and remains in the system, which results in smaller Al_3Ni/Al_3Ni_2 ratio.

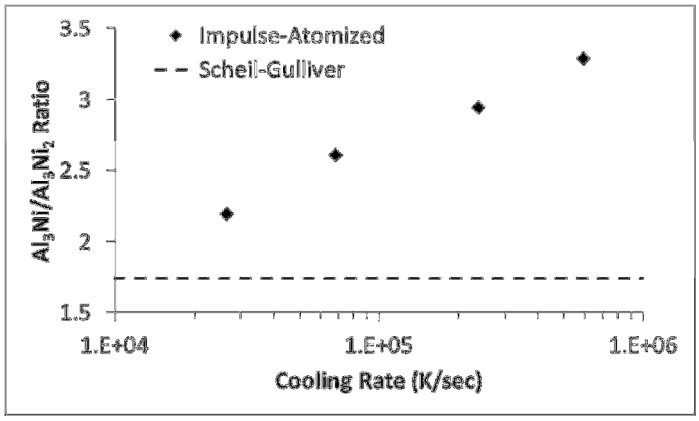

Figure 4.8. ND results for the ratio of Al_3Ni to Al_3Ni_2 as a function of cooling rate for Al-36 wt%Ni cooled in helium.

4.3.2.1. Metastable phase formation

Figure 4.9 shows part of neutron diffractogram of various particle sizes of IA Al-36 wt-%Ni alloy, in which particles with diameter smaller than 275 μm have an unidentified peak at ~3.5 $Å^{-1}$. This peak and other characteristic peaks observed at higher 2θ angles correspond to the formation of a quasicrystalline phase known as D-phase, which has close structural relationship to Al_3Ni_2 [4.18-21]. The formation of the D-phase requires very high undercooling. It has been shown that even in splat-cooled samples the D-phase forms in the thin external layers [4.19]. Shuleshova et al. [4.21] showed that this metastable phase forms within temperature interval 925-975 K, which corresponds to the undercooling of 150-200 K below the peritectic temperature at 1127 K. They also cited that Devred et al. found retained D-phase in gas atomized particles with diameter smaller than 38 μm. Since for IA particles, even in particles as large as 275 μm diameter, the peaks corresponding to D-phase exist, it can be concluded that these particles have experienced very high cooling rates during their fall inside the IA chamber.

4.3.2.2. Lattice parameter of Al_3Ni_2

By carrying out experiments approaching equilibrium conditions, Taylor and Doyle [4.12] showed that the *c/a* ratio for Al_3Ni_2 structure continuously decreases as the nickel content of Al_3Ni_2 decreases. They also suggested that the substitution of nickel atoms by aluminum atoms is responsible for the decrease of *c/a* ratio at the aluminum-rich side of stoichiometric Al_3Ni_2.

Figure 4.10 illustrates the effect of cooling rate on the lattice parameter ratio (*c/a*) of Al_3Ni_2 in droplets of Al-36 wt%Ni. From this figure it is evident that the *c/a* ratio for Al_3Ni_2 is significantly smaller than 1.2132, the stoichiometric *c/a* ratio of Al_3Ni_2, and it decreased with increasing cooling rate. It was shown that in Al-36 wt%Ni, with increasing cooling rate, the weight fraction of Al_3Ni increases. Therefore, it seems that by increasing the weight fraction of Al_3Ni, the *c/a* ratio decreases.

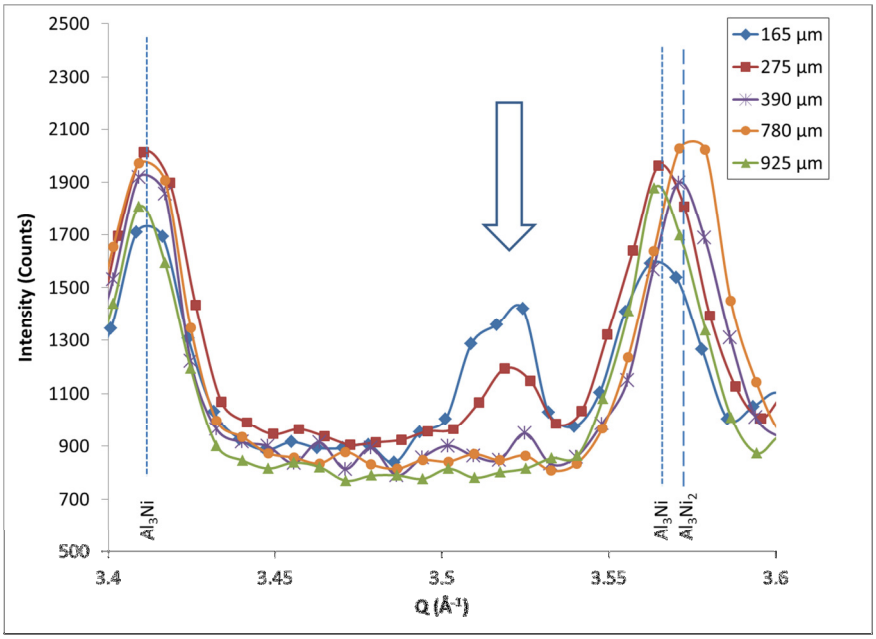

Figure 4.9. Part of neutron diffractogram of various particle sizes of IA Al-36 wt-%Ni, showing peak position of different phases. Note the unindexed peak at ~3.5$Å^{-1}$.

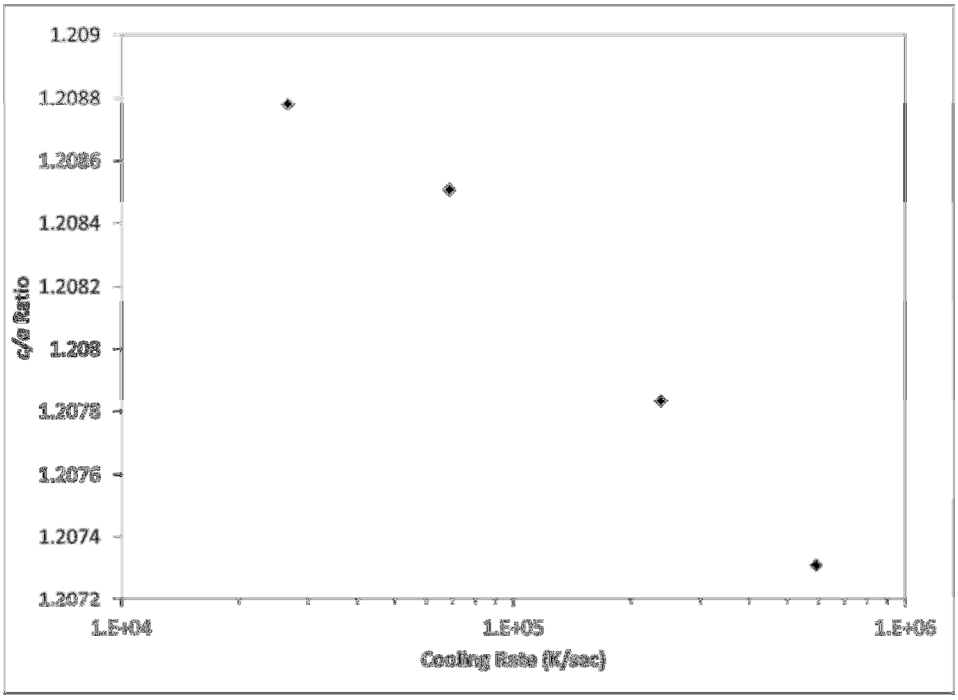

Figure 4.10. Lattice parameter ratio (*c/a*) of the phase Al_3Ni_2 in Al-36 wt%Ni.

4.3.3. X-ray micro-tomography

4.3.2.1. Microstructural analysis

The IA particles with diameters up to 550 µm were poured into a glass capillary tube for X-ray micro-tomography. Figure 4.11 shows one image, called slice, out of 2048 slices taken from particles of Al-36 wt%Ni. The size of each stack of 2048 images is 8 Gigabytes. From the figure, it is evident that in order to analyze individual particle it is necessary to perform a pre-processing procedure to separate the particle from the background noise, X-ray artifacts and other observed particles. MATLAB and Avizo™ were used to undertake this procedure. In brief, a clean mask file of the droplet was generated using

MATLAB image toolbox and then applied to the original data to eliminate all but the structural features of interest (see Appendix A and B for more details and the codes used).

High performance visualization software, Avizo®, was then used to visualize the porosity distribution within the droplets. Also, efforts were made to perform phase analysis using the X-ray micro-tomography images.

Figure 4.12 shows seven different slides out of 921 micro-tomography generated slides after performing the pre-processing procedure. Two very interesting features can be seen in the Figure 4.12. It seems that the particle shown in this figure has more than one nucleation site. In the slides shown at the top of Figure 4.12 several primary dendrite trunks are emanating from a nucleation point on the surface (top left, A), while in the slides shown at the bottom of Figure 4.12 primary trunks are emanating from a nucleation site inside the particle (top right, B). Previously, both Prasad et al. [4.6-7] and Henein et al. [4.8] had reported only single nucleation sites for Al-Cu and Al-Fe alloys. This suggests that in solidification of Al-Ni particles more heterogeneous nucleation sites , such as oxides, were available.

Another interesting point in Figure 4.12 is that porosity tends to form close to the nucleation site and the primary dendrite trunks. This is again opposite to the observations in eutectic alloys where porosity formed away from the nucleation site [4.6-8]. It seems that in Al-36wt%Ni alloy, nucleation and growth of the peritectic product and its morphology that grows freely into the melt, Figure 4.3, results in separation of the remaining liquid between the trunks and

the liquid pool ahead of the solidification front. Therefore, the liquid pool is not able to feed the solidification shrinkage in the space between the primary trunks, and hence, porosity forms in this area.

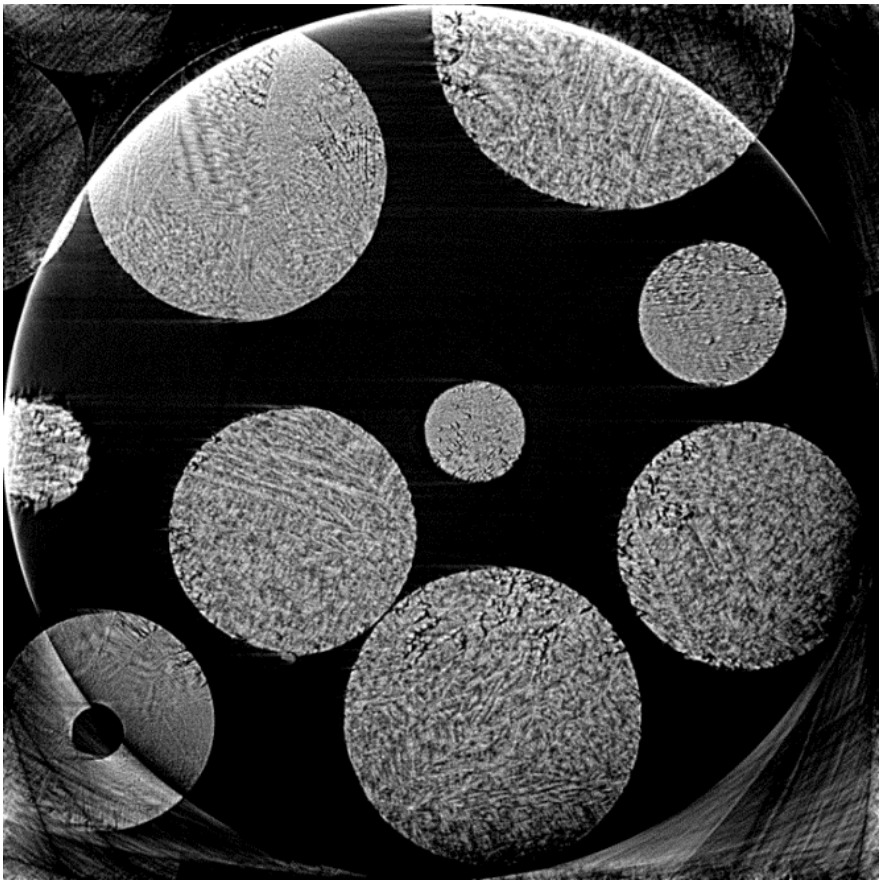

Figure 4.11. One slice out of stack of 2048 slices of particles of Al-36 wt%Ni.

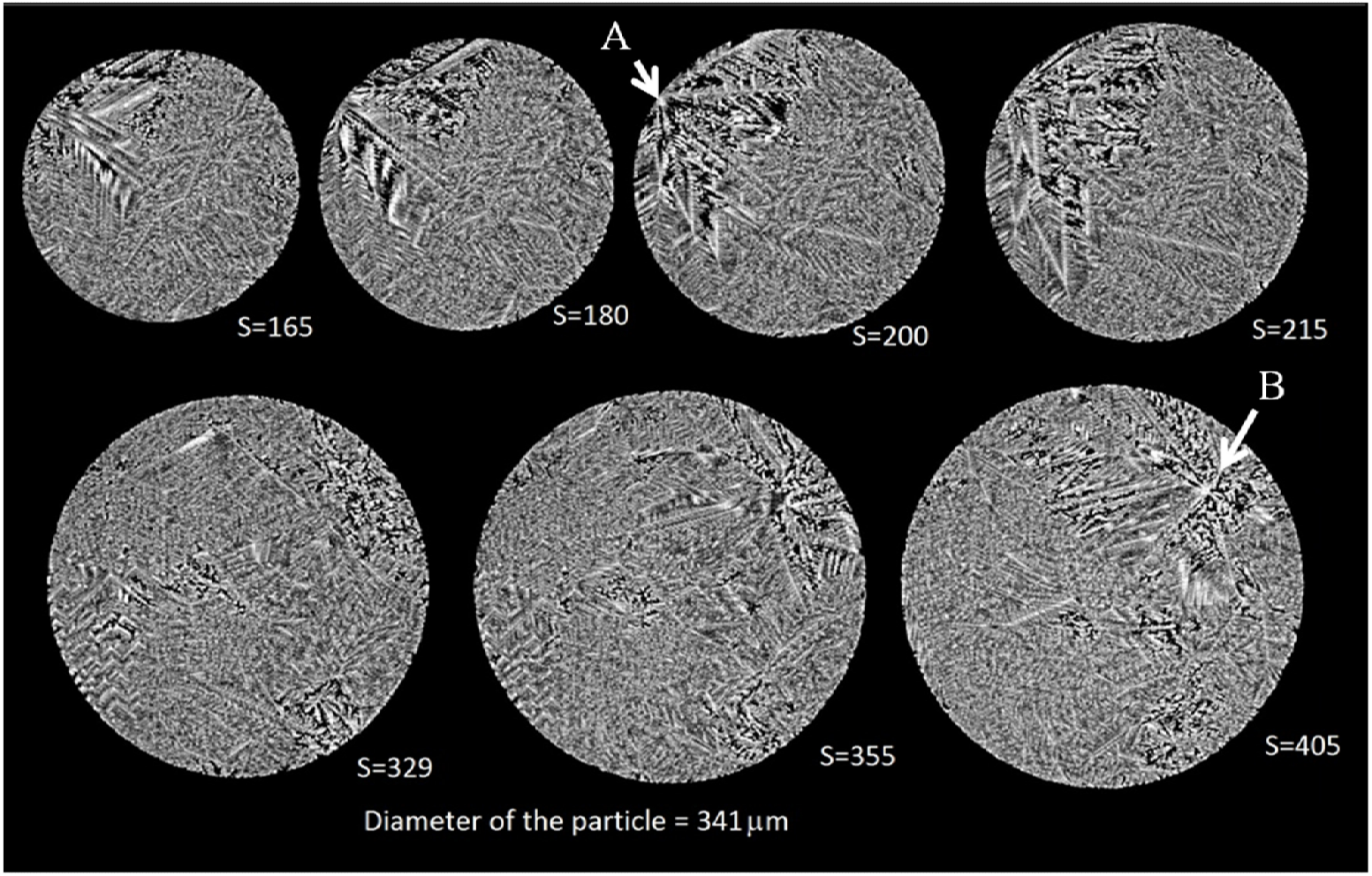

Figure 4.12. Slides number 165, 180, 200, 215, 329, 355 and 405 of an IA particle of Al-36wt%Ni with diameter of 341 µm. A and B are the only nucleation points in this droplet.

The results of X-ray micro-tomography of a particle that was solidified at higher cooling rate is shown in Figure 4.13. This figure shows five slides out of 486 slides from a particle with diameter of 180 μm. Detailed analysis of the micro-tomography results revealed that in this particle only one nucleation site exists, which is not surprising considering the smaller size of this particle [2.18] compared to that in Figure 4.12. However, a significant difference can be observed between Figure 4.12 and Figure 4.13. While in the particle seen in Figure 4.13 porosity forms close to the nucleation site and the primary dendrite trunks, in the small particle shown in Figure 4.13 porosity is observed away from the nucleation site. It must be noted that in this particle formation of Al_3Ni_2 and, hence, the peritectic reaction, was suppressed. The resulting microstructure, therefore, is similar to those observed in eutectic alloys such as Al-Cu and Al-Fe [4.6-8]. As was mentioned in the previous section, increasing cooling rate as a result of decreasing particle size results in the suppression of the primary Al_3Ni_2, and as a result, Al_3Ni forms directly from the liquid.

It seems that for the particle shown in Figure 4.13, solidification started from the nucleation point on the left side of the particle and it advanced to the right. The last liquid to solidify was on the right side of the particle, where shrinkage porosity was formed. This can be better seen by 3D visualization of porosity shown in Figure 4.14. To construct the Figure 4.14, only voxels that have grayscale similar to that of porosity are shown. It is evident that almost all porosity was formed on the opposite side of the nucleation point.

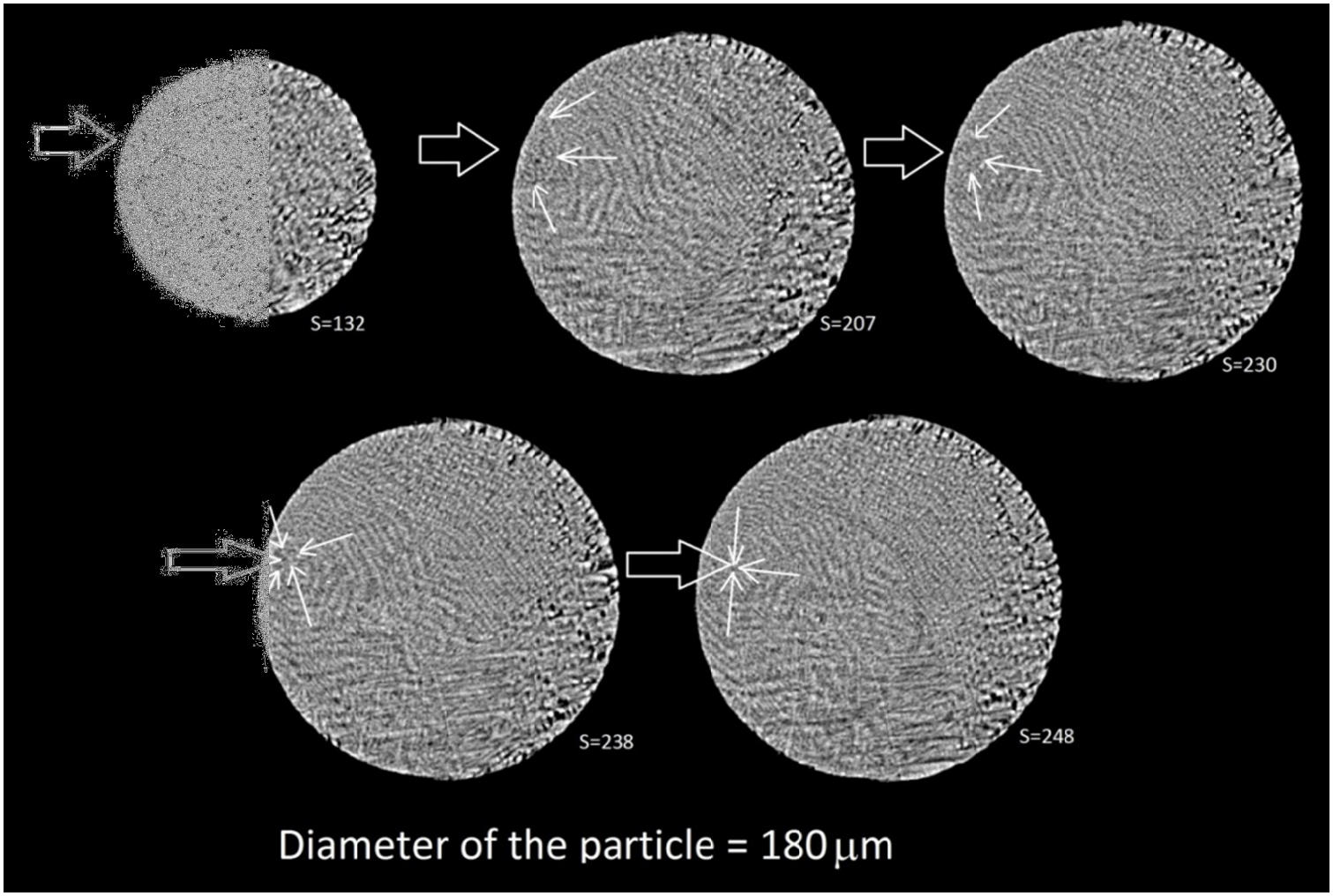

Figure 4.13. Slides number 132, 207, 230, 238 and 248 of an IA particle of Al-36wt%Ni with diameter of 180 µm.

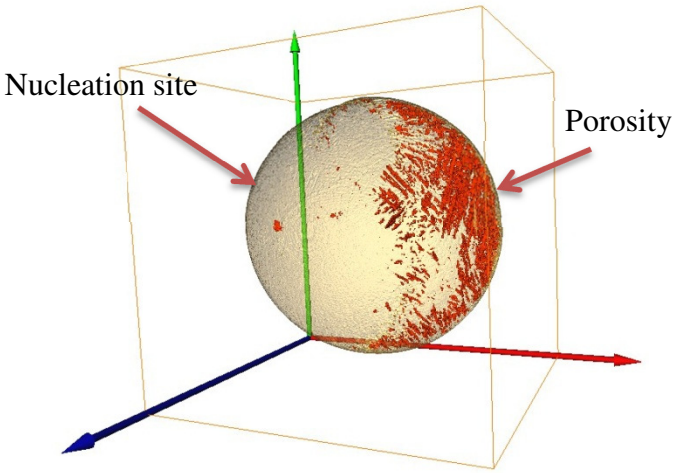

Figure 4.14. 3D visualization of the particle shown in Figure 4.13. Almost all porosity was formed on one side of the particle's sphere.

The size of the particle in Figure 4.12 was 341 µm and the size of the particle in Figure 4.13 was 180 µm. In Figure 4.15 different slides from a particle with the diameter of 216 µm are shown. Two distinct regions in this particle can be observed. While the left side of this particle has a microstructure similar to that of the particle in Figure 4.12, the right side of the particle resembles the particle in Figure 4.13. It seems that in this particle size (216 µm), initially, solidification started with such high undercooling that the peritectic reaction was suppressed. Then, the heat released as a result of recalescence caused temperature increase to rise above the peritectic reaction and as a result, the left side of the particle solidified has similar microstructure to Figure 4.12. It is also interesting that almost no porosity is observed in the right hand region, where the structure is similar to Figure 4.13.

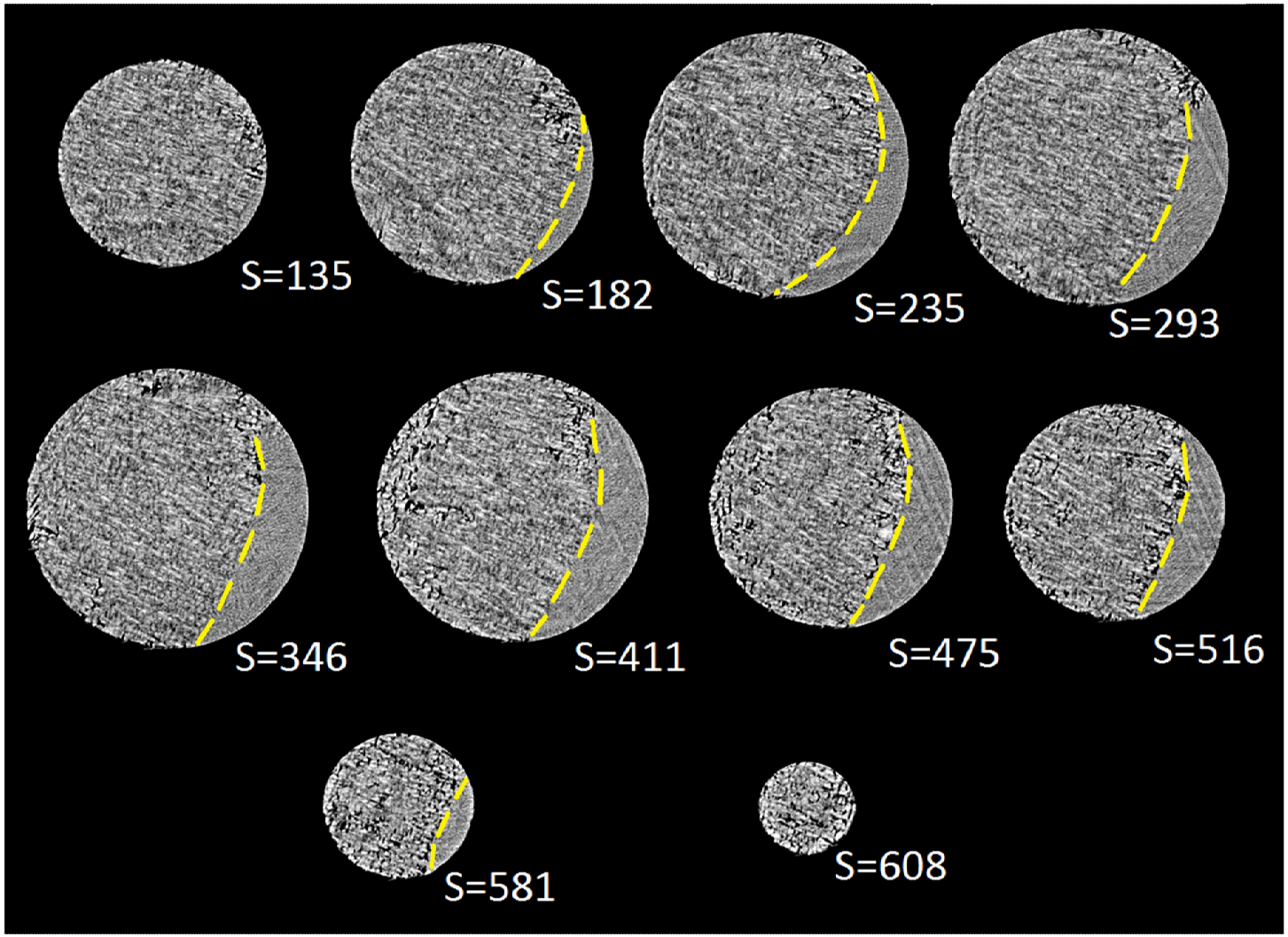

Figure 4.15. Slides number 135, 182, 235, 293, 346, 411, 475, 516, 581 and 608 of an IA particle of Al-36wt%Ni with diameter of 216 µm showing two distinct regions.

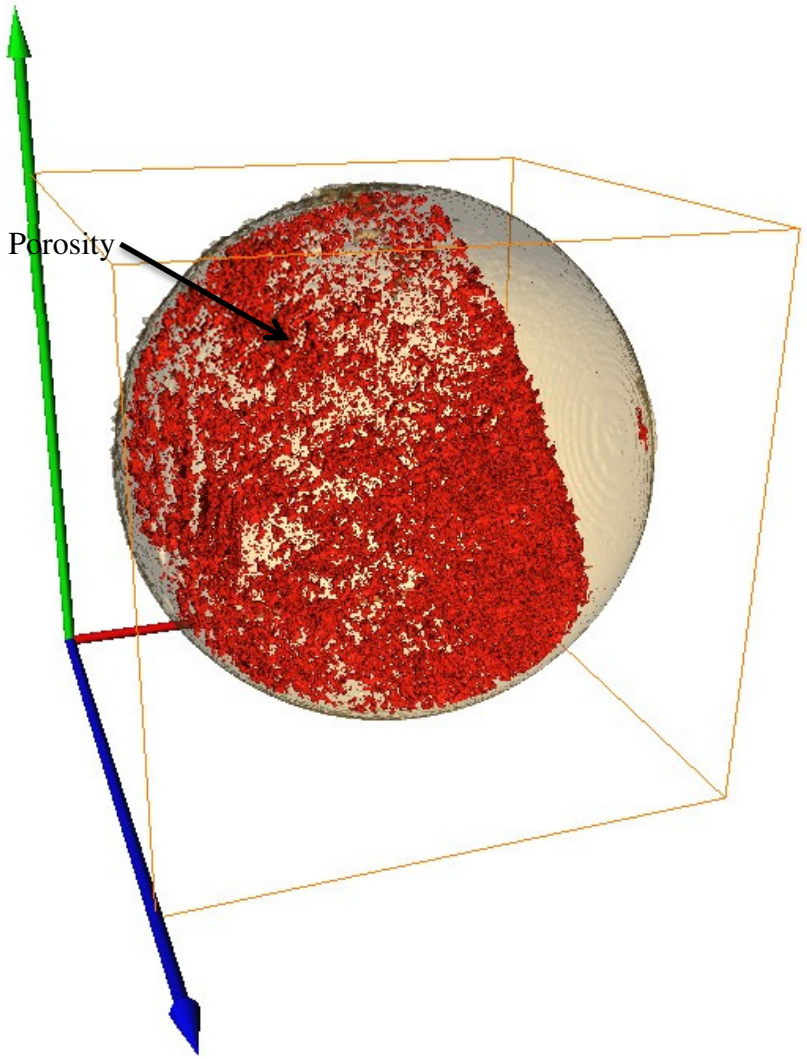

Figure 4.16. 3D visualization of the porosity in the particle shown in Figure 4.15. While the particle has spherical shape, almost no porosity is observed on the right side of the particle.

3D visualization of porosity, shown in Figure 4.16, also confirms this observation. It is evident that almost no porosity was formed in the region that the peritectic reaction was suppressed.

The average volume fraction of porosity was also quantified to explore the effect of cooling rate on the amount of porosity formed within the atomized droplets. The procedure involves calculating the number of pixels with gray scale levels matching that of porosity within the entire droplet volume. The results are shown in Figure 4.17. Quantitative analysis of these images revealed that the volume percent of porosity decreases with increasing cooling rate. This is in agreement with the generally accepted effect of higher cooling rate on reducing porosity [4.20]. In the case of Al-36 wt%Ni, at a smaller cooling rate, the alloy experiences a larger freezing range, which results in the formation of more Al_3Ni_2. Formation of more Al_3Ni_2 followed by the peritectic reaction makes the feeding of the shrinkages more difficult, and as a result, the volume percent of porosity increases.

4.3.2.2. Phase analysis

Preforming phase analysis on the X-ray micro-tomography images is difficult. Firstly, because of the fineness of the structure, sometime the size of the feature of interest is close to the resolution of the technique, which is 0.37 µm in this case. Secondly, the X-ray absorbance of Al_3Ni_2 and Al_3Ni are close, which makes it difficult to distinguish the two phases. In order to perform the phase analysis on tomography images it is required to have distinguishable peaks for phases in the histogram in order to choose a proper threshold value. In the case of Al-36 wt%Ni a histogram is shown in Figure 4.18, which is for the particle shown in Figure 4.12. From the figure, it is obvious that allocating a gray scale range from this

result alone to a particular phase is arbitrary and cannot be used for phase analysis.

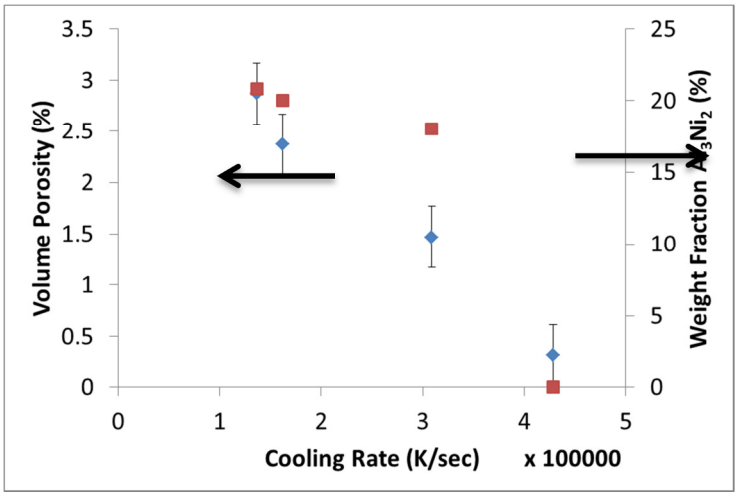

Figure 4.17. Quantification of porosity as a function of cooling rate resulted from image analysis on X-ray micro-tomography data. Error bars represent one S.D.

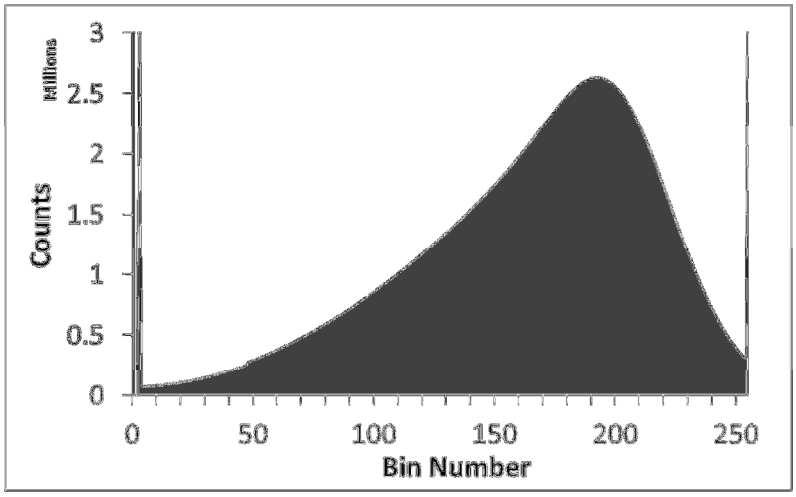

Figure 4.18. Histogram from stack of 921 slides of an IA particle of Al-36wt%Ni with diameter of 341 µm.

A new method was used in order to find the proper threshold values for phase separation. For this purpose, the phase fractions that were found from Rietveld analysis on ND patterns were used. The threshold values from tomographic scans were chosen in a way that similar phase fractions to those found from Rietveld analysis is achieved. These threshold values are then applied to the other particles for validation. It must be noted that the particles must be of same composition. Also, all tomography experiments for one alloy must be done under similar condition for the purpose of this analysis; otherwise the threshold values from one particle cannot be applied to other particles of the same composition. The preliminary result for this analysis is shown in Figure 4.19. Figure 4.19(a) shows one slide from 921 slides of the particle shown in Figure 4.12. Figure 4.19(b) is the same slide after segmentation. The grayscale threshold values that produce similar results to those found from Rietveld analysis are listed in Table 4.1.

Table 4.1. The grayscale threshold values used for image segmentation.

Phases	**Grayscale threshold value**
Background - Porosity	0
Porosity - Eutectic	5
Eutectic – Al_3Ni	105
Al_3Ni – Al_3Ni_2	190

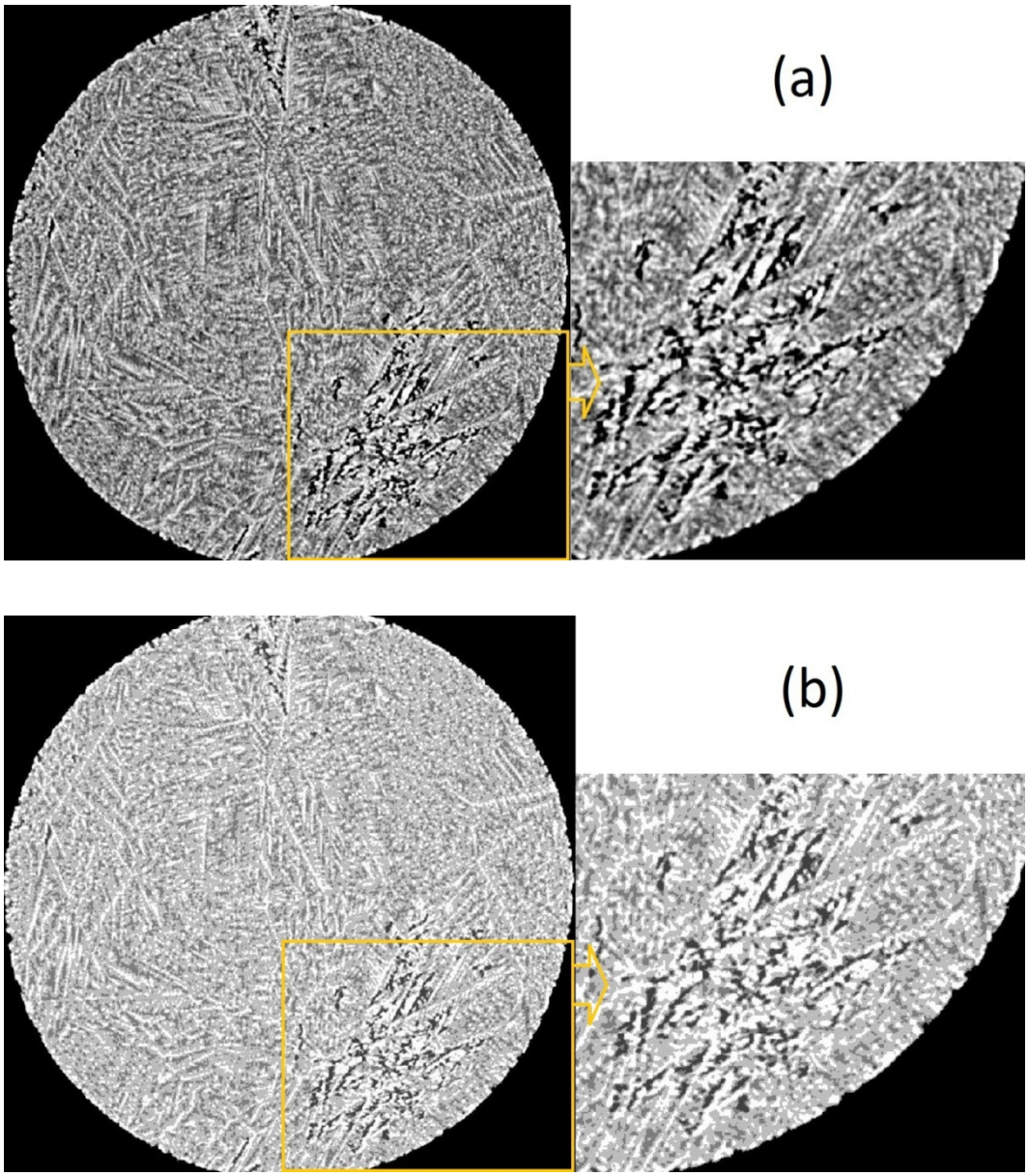

Figure 4.19. One slide from stack of 921 slides of an IA particle of Al-36wt%Ni with diameter of 341 μm. (a) Original image (b) after phase separation using the values found from Rietveld analysis.

From Figure 4.19, it is evident that the segmentation threshold values that can provide similar phase fractions to those achieved using ND would produce

visually acceptable segmentation of the original image. In order to further investigate this technique, the threshold values of Table 4.1 were applied to four other particles and the phase fractions were calculated. The results for measured Al_3Ni to Al_3Ni_2 ratio are shown in Figure 4.20. In this figure, the results from Rietveld analysis that were shown in Figure 4.8 were also re-plotted.

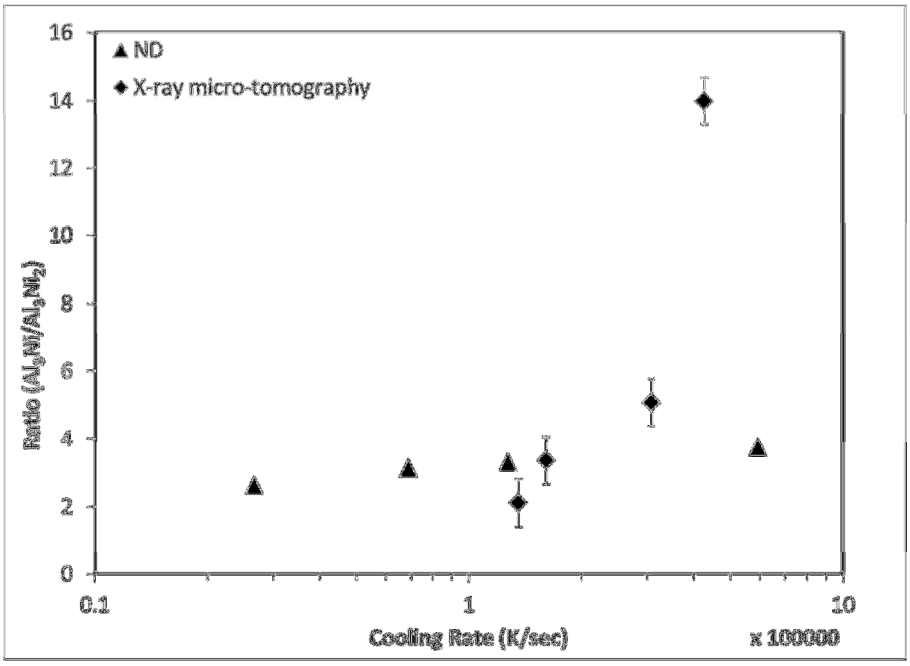

Figure 4.20. Phase fraction analysis using X-ray micro-tomography images and ND.

It is evident that Al_3Ni to Al_3Ni_2 ratio increased with increasing cooling rate, similar to the trend observed in Figure 4.8. However, phase ratios at similar cooling rates from the image analysis technique are larger at the highest cooling rate than that from ND. The reason for such a difference in result is likely due to

the reduced scale of the microstructure at high cooling rates compared to the resolution used for x-ray tomography. Specifically, the cell spacing for the 4.3×10^5 K/s sample is 0.92 microns and the x-ray tomography resolution was 0.37 μm.

The new method for phase separation in X-ray micro-tomography images showed some promising results. In order to further investigate this technique, X-ray micro-tomography from more particles is required.

4.4. Conclusions

In this chapter, effects of cooling rate on microstructure and phase fraction of an alloy with one peritectic reaction was investigated. Rapidly solidified particles of Al-36 wt%Ni were produced using IA technique. The microstructure of the produced particles was analyzed using SEM and X-ray micro-tomography and SDAS was used to estimate the solidification cooling rate. Also, ND was used to investigate the phases formed during solidification. Rietveld analysis was then applied using the GSAS software to measure the ratio of Al_3Ni to Al_3Ni_2. Also, Scheil-Gulliver equation was applied to investigate the extent to which it can predict the phase fractions in these alloys.

It was found that by increasing cooling rate the ratio of Al_3Ni to Al_3Ni_2 also increases. It was suggested that the time available for solidification and growth of Al_3Ni_2 is likely to be responsible for the observed changes. It was also found that particles with diameter smaller than 275 μm contain some peaks that

correspond to the formation of a quasicrystalline phase, known as D-phase. It was also found that at high cooling rate the formation of the primary Al_3Ni_2 was suppressed.

X-ray micro-tomography was used to investigate the 3D structure of the solidified particles. Also, porosity within the particles was quantified and the distribution of porosity with regard to the nucleation site and cooling rate was discussed. Multiple nucleation sites were observed in large particles (341 μm) while in small particles (180 μm) only one nucleation site was found. The distribution of porosity within these two particles was found to be significantly different, which corresponds to the suppression of the primary phase in the latter particle. Quantitative analysis of the micro-tomography images revealed that the volume percent of porosity increases with increasing particle size. A new method for phase analysis using X-ray micro-tomography was presented.

In the next chapter, the solidification of an alloy with two peritectic reactions will be studied.

4.5. References

4.1. Kerr, H. W., Kurz, W., "Solidification of Peritectic Alloys", International Materials Reviews, Vol. 41, No. 4, (1996), 129-164.

4.2. Umeda, T., Okane, T. and Kurz, W., "Phase selection during solidification of peritectic alloys", Acta Materialia 44(10), (1996), 4209-4216.

4.3. Povarova, K. B., Lomberg, B. S., Filin, S. A., Kazanskaya, N. K., Shkol'nikov, D. Y. and Bespalova, M. D., "Structure and properties of Ni-Al-Co system (β+γ)- alloys", Izvestia Akademii nauk SSSR. Metally, (1994), No. 3, 77-84.

4.4. Devred F, Reinhart G, Iles G N, Van D K, Adkins N J, Bakker J W, Nieuwenhuys B E, "Synchrotron X-ray microtomography of Raney-type nickel catalysts prepared by gas atomisation: Effect of microstructure on catalytic performance", Catalysis Today, (2011) 163(1) 13-19.

4.5. Bao, C. M., Dahlborg, U., Adkins, N., Calvo-Dahlborg, M., "Structural Characterization of Al-Ni Powders Produced by Gas Atomisation", Journal of Alloys and Compounds, 481, (2009), 199–206.

4.6. Prasad, A., Henein, H., Maire, E. and Gandin, C. A. "X-ray tomography study of atomized al-cu droplets", Canadian Metallurgical Quarterly, 43(2), (2004), 273-282.

4.7. Prasad, A., Henein, H., Maire, E. and Gandin, C. A., "Understanding the rapid solidification of al-4.3Cu and al-17Cu using X-ray tomography", Metallurgical and Materials Transactions A, 37(1), (2006), 249-257.

4.8. Henein, H., Buchoud, V., Schmidt, R.-R., Watt, C., Malakhov, D., Gandin, Ch.-A., Lesoult, G., Uhlenwinkel, V., "Droplet solidification of impulse atomized Al-0.61Fe and Al-1.9Fe", Canadian Metallurgical Quarterly 49(3), (2010), 275.

4.9. Ilbagi, A., Delshad Khatibi, P. and Henein, H., "The effect of hydrogen evolution during the rapid solidification of Al-9.5Si alloy", Proc. of

PowderMet2011 (San Francisco, CA), (2011).

4.10. St John, D. H. and Hogan, L. M., "A Simple Prediction of the Rate of the Peritectic Transformation", Acta Metallurgica, Vol. 35, Issue 1, (1987), 171-174.

4.11. Thevand, A., Poize, S., Crousier, J. -P. and Streiff, R., "Aluminization of nickel-formation of intermetallic phases and Ni2Al3 coatings", Journal of Materials Science, vol. 16, issue 9, (1981), 2467-2479.

4.12. Taylor, A. and Doyle, N. J., "Further studies on the nickel-aluminum system. I. β-NiAl and δ-Ni2Al3 phase fields", Journal of Applied Crystallography (1972). 5, 201-209.

4.13. Nash, P., Singleton, M. F. and Murray, J. L., Phase Diagrams of Binary Nickel Alloys. In: ASM, Materials Park, OH, (1991), 3.

4.14. Henein, H., "Single Fluid Atomization through the Application of Impulses to a Melt", Materials Science and Engineering: A, Vol. 326, No. 1, (2002), 92-100.

4.15. Von Dreele, R. B., Neutron Diffraction in Materials Science and Technology: A Comprehensive Treatment, Vol. 2B, Wiley–VCH, New York, NY, (1994).

4.16. Kurz, W. and Fisher, D. J. Fundamentals of solidification, Aedermannsdorf, Transaction Technical Publication, (1989), p 88.

4.17. Tourret, D., Gandin, Ch.-A., "A generalized segregation model for concurrent dendritic, peritecticand eutectic solidification", Acta Materialia, 57, (2009), 2066–2079.

4.18. Pohla, C. and Ryder, P. L., “Crystalline and quasicrystalline phases in rapidly solidified Al-Ni alloys”, Acta Materialia 45, (1997), 2155-2166.

4.19. Grushko, B. and Holland-Moritz, D., “Decagonal quasicrystals in Al-Co, Al-Ni and in their ternary alloys”, Materials Science and Engineering A 226-228, (1997), 999-1003.

4.20. Pohla, C. and Ryder, P. L., “Quasicrystals in Al-Ni alloys”, Materials Science and Engineering A, 134 (1991), 947-950.

4.21. Shuleshova, O., Holland-Moritz, D., Loser, W., Reinhart, G., Iles, G. N. and Buchner, B., “Metastable formation of decagonal quasicrystals during solidification of undercooled Al-Ni melts: in situ observations by synchrotron radiation”, Europhysics Letters, 86(3), (2009), p 36002 (4 pp.).

4.22. Han, Q., Shrinkage Porosity and Gas Porosity, Casting, Vol. 15, ASM Handbook, ASM International, (2008), p 370–374.

Chapter 5

5. Phase Quantification of Impulse-Atomized Al-50 wt%Ni Alloy [4]

5.1. Introduction

In the previous chapter, solidification of an alloy with one peritectic reaction was studied and the effect of cooling rate on phase fractions and microstructure was investigated. In this chapter, solidification of a more complex alloy will be studied. While a peritectic reaction during solidification is still not very well understood [5.1-2], the Al-50 wt%Ni alloy has two of these reactions, which presents a bigger challenge to understand and quantify the solidification path of this alloy. Al-Ni alloys are used as a heterogeneous catalyst in a variety of organic syntheses. The phase fractions of Al_3Ni_2, Al_3Ni and Al formed during solidification has an important effect on the performance of these alloys in their applications. For example, Devred et al. [5.3] found that the catalytic activity of Raney Nickel (Al-50 wt%Ni) was very sensitive to initial alloy composition and it increased with increasing fraction of Al_3Ni phase. It is, therefore, vital to know and to predict the phase fractions formed during the solidification of Al-Ni alloys under a range of cooling conditions.

Rapid solidification of materials can produce a refined microstructure, extension of solid solubility, change in morphology and formation of metastable phases. With such significant advantages, many rapid solidification techniques

[4] A major part of this chapter was published at ***J. Mater. Sci.*** 46:6235–6242 and reformatted according to thesis requirements.

have been used to study phase selection during solidification of Al-Ni alloys. Patchett and Abbaschian [5.4] studied the rapid solidification of Al-30 to 60 wt.% Ni using splat cooling and drop tube experiments. They found that cooling rate can greatly alter the volume fractions of pro-peritectic, peritectic and eutectic phases. Bao et al [5.5] analyzed Al-Ni powders produced by gas atomization having different compositions on the Al-rich side of the phase diagram. They used ND and XRD to identify the existing phases at the surface and in the bulk of the particles. Their results show a significant dependence of phase selection during the solidification of different sized gas atomized particles. Other scientists simulated the solidification of Al-Ni alloys using microsegregation [6] and phase field [7] models, and showed that there is a strong influence of cooling rate and temperature gradient on the solidification path of these alloys.

Although some papers have been published on this subject, the effect of rapid solidification conditions on the resulting phase selection and the associated shrinkage porosity is still not well understood. In this chapter, first the solidification path of Al-50 wt%Ni is outlined. Then, a relatively new technique called IA is used to generate rapidly solidified particles of Al-50 wt%Ni alloy. The details of the technique can be found elsewhere [5-8-9]; however, it is briefly discussed in the following section. The powders are then characterized using ND, SEM, optical microscope (OM) and X-ray micro-tomography to measure the weight fractions of different phases and to investigate the porosity formation as a function of cooling rate. Also, the effect of cooling rate on the lattice parameter of Al_3Ni_2 will be discussed.

5.1.1. Solidification Path

5.1.1.1. Equilibrium

From the phase diagram, the solidification of an Al-50 wt%Ni alloy can be explained as follows (see Figure 5.1). At 1133 ºC the primary AlNi dendrites, which had started to solidify at about 1300 ºC, react with the surrounding liquid in a peritectic reaction to form Al_3Ni_2. It is expected that at this composition the entire primary AlNi phase transforms to Al_3Ni_2. The peritectic product grows until it reaches the second peritectic reaction at 854 ºC, where it reacts with the remaining liquid to form Al_3Ni. At this composition, this reaction is not expected to go to completion, and a final composition consisting of 58 wt% Al_3Ni_2 and 42 wt% Al_3Ni should form. The equilibrium phase diagram predicts no eutectic aluminium for this composition.

5.1.1.2. Scheil-Gulliver Equation

To calculate the phase fractions using Scheil-Gulliver model, in the case of Al-50 wt%Ni, at 1133 ºC, the fractions of solid (AlNi) and liquid can be calculated using the compositions shown on the phase diagram (C_S=57.97at% Al, C_L=73.07at% Al and C_0=68.50 at% Al).

For the next reaction, at 854 ºC, C_0 has the composition of the remaining liquid from the previous step, which was 73.07 at% Al. At this temperature C_L=84.83 at% Al and C_S=63.18 at% Al. Using Scheil-Gulliver equation, the amount of Al_3Ni_2 that has formed is calculated. Since it was previously shown

[5.5] that all AlNi transforms to Al_3Ni_2, the total amount of Al_3Ni_2 is calculated by adding the results of the first two steps together. Step 3, at 639.9 ºC, gives the fraction of pro-eutectic Al_3Ni and it is similar to step two. In this case, the last liquid composition from step 2, 84.83 at% Al, is used as the initial composition for step 3. C_S is 75.03 at% Al and C_L is 97.30 at% Al. The remaining liquid of this step transforms to Al and Al_3Ni in a eutectic transformation. From these calculations, the ratio of Al_3Ni to Al_3Ni_2 for Al-50wt%Ni is 0.33.

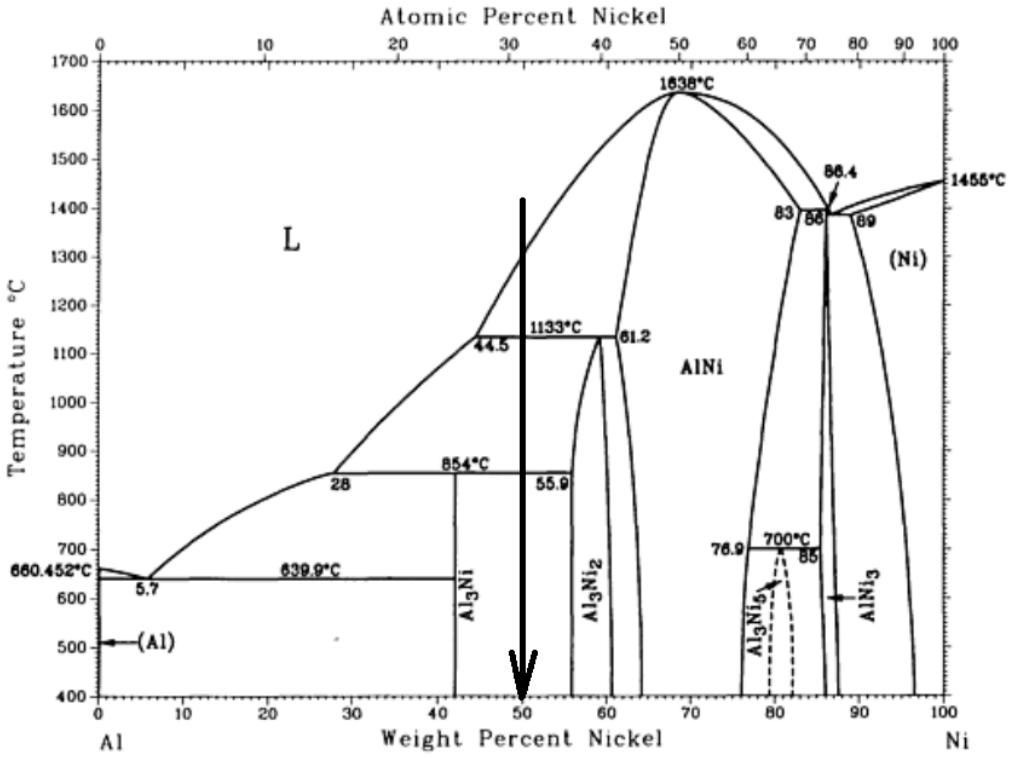

Figure 5.1. Al-Ni phase diagram [5.10]. Arrow shows the composition investigated in this chapter.

5.2. Experimental

Powders of Al-50 wt%Ni were produced by melting aluminum granules (99.9% pure) and nickel shot (99.9% pure) in an induction furnace under different atmospheres of helium and nitrogen. The IA was performed by holding the alloy at 100ºC above the liquidus temperature for 30 minutes. Then, the liquid was pushed through orifices at the bottom of the crucible to generate a liquid stream, which subsequently broke up into spherical droplets by Rayleigh instability. The droplets lose their heat as they fall through a stagnant gas atmosphere of either helium or nitrogen having a maximum oxygen content of 10 ppm. The powders are solidified by the time they reach an oil quench bath at 4m from the atomizing nozzle. The solidified droplets are subsequently washed and sieved into different sizes based on MPIF Standard 05 [5.11]. The actual composition of each alloy was measured using the inductively coupled plasma atomic emission spectroscopy (ICP-AES) technique.

Samples of different sized powders were mounted in epoxy and then ground and polished for microstructural analysis. SEM was performed using a Zeiss Evo MA15 to study the microstructure of the different sized particles and to measure the SDAS. EDX analysis on the SEM was done using a Bruker Silicon Drift Detector with a peak resolution of 125 eV.

In order to investigate the effect of processing parameters and particle size on the phase fractions of the solidified droplets ND was conducted on different size ranges of particles. Experiments were performed at the Oak Ridge National Laboratory (ORNL) in Oak Ridge, Tennessee, and Atomic Energy of Canada

Limited (AECL) in Chalk River, Ontario. The ND experiment was conducted using a neutron beam of 1.33 Å wavelength. To obtain the weight fraction of the phases formed under different conditions, Rietveld analysis was performed using the GSAS software [5.12].

Optical microscopy using Leica DM ILM was utilized to investigate the porosity fraction within the cross section of the particles. Image analysis on these images was performed using the ImageJ software. Further investigations on the amount and distribution of porosity were conducted using X-ray micro-tomography on the droplets of diameter of 181 and 328 μm. The experiments were carried out on the ID19 beam line at the European Synchrotron Radiation Facility (ESRF) in Grenoble, France (0.28 μm resolution) and on the beam line Tomcat, X02DA at Swiss Light Source, Paul Scherrer Institut, Villigen, Switzerland (0.37 μm resolution). Quantitative analysis of this data required a tedious and memory intensive pre-processing to remove background noise and X-ray artifacts. The method used to ease this process is explained in detail elsewhere [5.13] (see Appendix A). In brief, a clean mask file of the droplet was generated using MATLAB image toolbox and then applied to the original data to eliminate all but the structural features of interest. High performance visualization software, Avizo®, was then used to visualize the porosity distribution within the droplets.

5.3. Results

Table 3.1 shows the conditions of specific IA runs, as well as the actual

composition of the particles measured using ICP-AES technique. The mass mean droplet diameter (D_{50}) and the log normal standard deviation (σ) were calculated from the powder size distribution fitted to a log-normal function.

Table 5.1. Alloy compositions and atomization conditions.

Atomization run number	Atomization atmosphere	Nominal Composition	Number of Orifices	Actual Composition	D_{50}/σ^*
080731	He	$Al_{68.5}Ni_{31.5}$	37	Al-31.3at%Ni	436/1.46
080916	N_2	$Al_{68.5}Ni_{31.5}$	37	Al-31.1at%Ni	402/1.39

*$\sigma=D_{84}/D_{50}$

5.3.1. SEM

The effect of cooling gas and particle size on the scale of the microstructure was investigated. In brief, microstructural analysis of the produced particles using SEM showed that the particles have almost perfect spherical shape with an internal dendritic microstructure, the size of which is dependent on the cooling rate. Figure 5.2 shows an example of the effect of cooling gas, where using helium (a) as opposed to nitrogen (b) resulted in a refined microstructure for particles of the same size. Both micrographs seem to have a typical peritectic structure, in which the light gray phase is surrounded by dark gray phase. EDX analysis showed that the dark grey phase contain 24 at% nickel, which can be attributed to Al_3Ni, while the core of the dendrites has 42 at% nickel, close to that of Al_3Ni_2. The area between the dendrites is the non-equilibrium eutectic, shown as the black phase and contains more than 96 at% aluminum. An interesting point is

the morphology of the dark grey phase in Figure 5.2b that apparently, grew freely into the liquid.

Besides changing the type of the cooling gas, decreasing the particle size was also found to affect the microstructure of the atomized particles. This is evident from the changes in the SDAS values. Figure 5.3 shows the SDAS values as a function of particle size in both helium and nitrogen. Also, using the data listed in Table 5.2 and the equilibrium phase diagram, the cooling rates of the particles were calculated. Details of this calculation were discussed in the previous chapter. In Chapter 6, the accuracy of the assumed values for Γ and D was investigated. Also, it was assumed that for both compositions studied in this research, same values of Γ and D can be used as they are representing the change in solidification temperature of liquid and diffusion of elements within liquid phase, respectively.

The measured SDAS as a result of different cooling rates is plotted in Figure 5.4. It can be seen that the particles atomized in helium experienced higher cooling rates than those atomized in nitrogen. From Figure 5.4 the SDAS can be related to the cooling rate using the Eq. 5.1.

$$\lambda = 75.38\dot{T}^{-0.33} \tag{5.1}$$

Table 5.2. Values used to calculate the cooling rate of atomized particles.

Name	Symbol	Value	Unit
Diffusion Coefficient	D	10^{-8}	m^2s^{-1}
Gibbs–Thomson coefficient	Γ	10^{-8}	mK

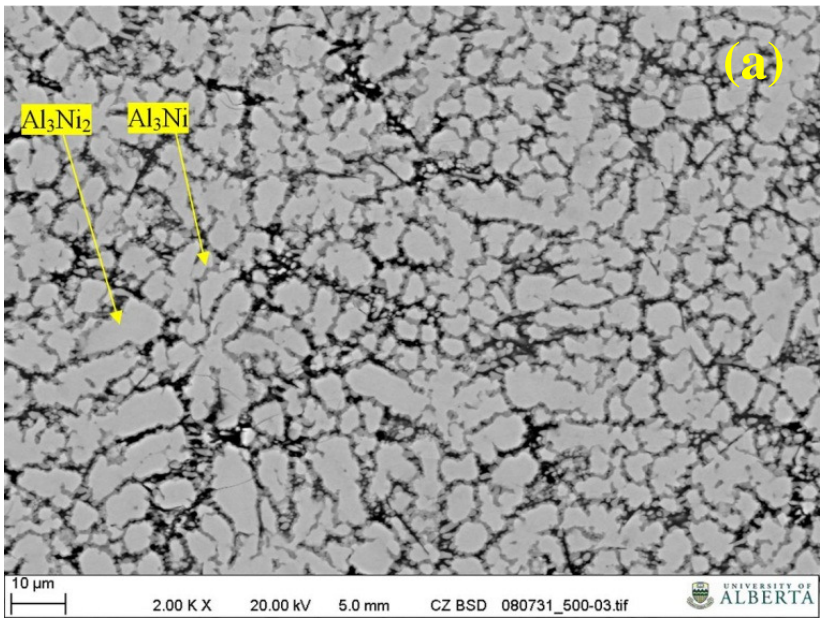

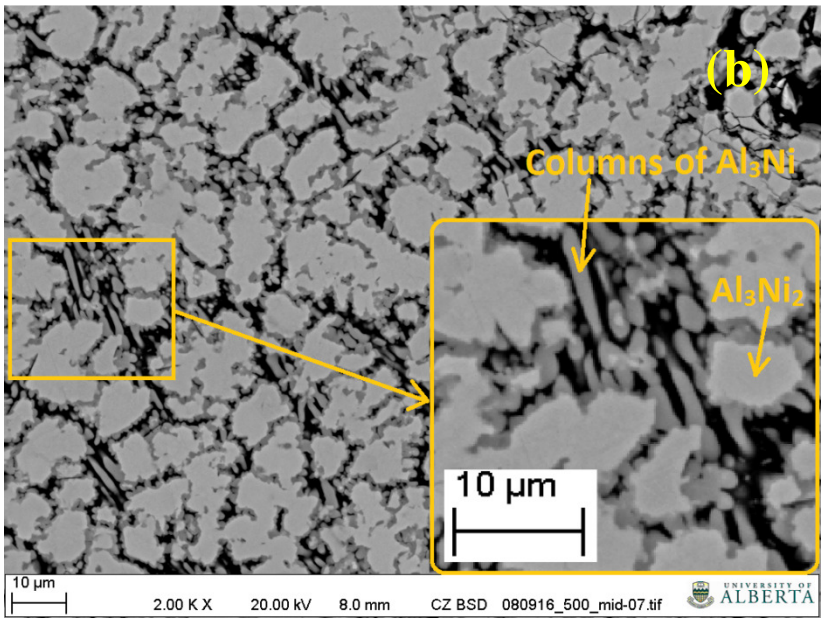

Figure 5.2. Microstructure of atomized particle of Al-50 wt%Ni, (a) atomized in helium (b) atomized in nitrogen. The diameter of both particles is 550µm.

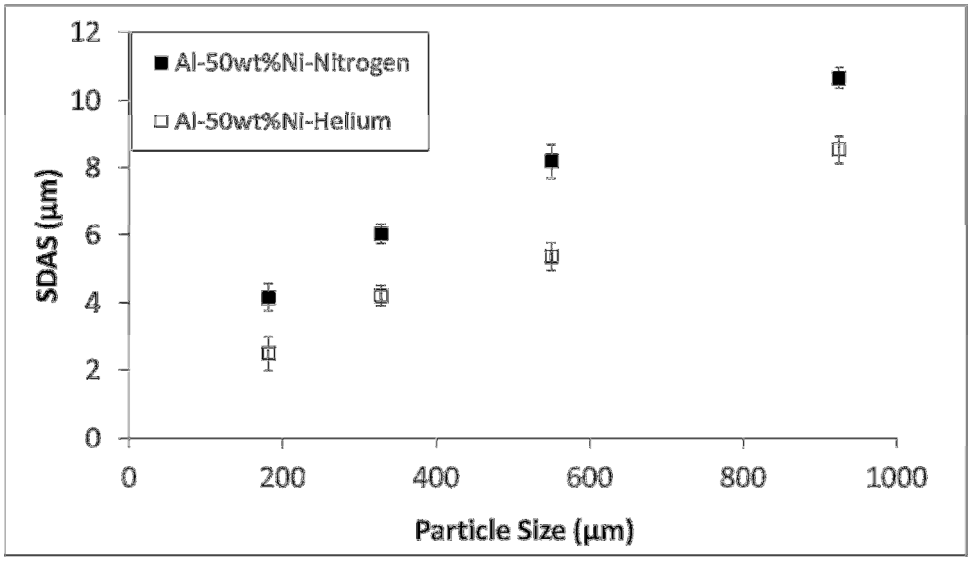

Figure 5.3. Effect of particle size and gas type on the SDAS.

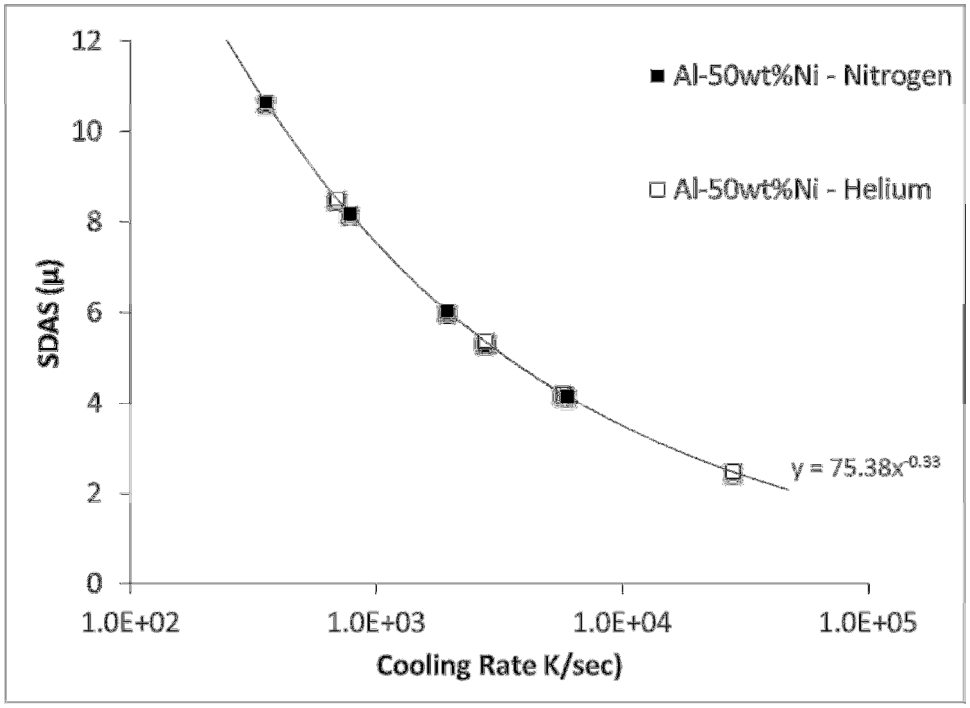

Figure 5.4. The calculated cooling rate of Al-50 wt%Ni atomized both in helium and nitrogen.

5.3.2. Neutron diffraction

Rietveld analysis was carried out using GSAS on both ND data from different particle sizes atomized in helium and nitrogen. Figure 5.5 shows one example of the measured ND pattern of Al-50 wt%Ni with the diameter of 328 μm and cooled in helium. A profile refinement using the GSAS computer code showed that only three phases (i.e. Al_3Ni_2, Al_3Ni and Al) existed in the entire size range (256, 390, 463, 550, 780, 925 μm) that was investigated. In Figure 3.3, the top line shows the calculated diffraction pattern as obtained from GSAS software and the bottom line represents the difference between the observed and calculated diffraction pattern. The small vertical bars indicate the positions of diffraction peaks of the Al_3Ni_2 (top), Al_3Ni (middle) and Al (below). No sign of AlNi was observed in the diffraction pattern. Similar results have been reported in the literature for gas atomization of Al-Ni alloys [5.5], in spite of the fact that AlNi has been found to be the primary phase formed in a wide range of undercooling up to 320K [5.14]. The mechanism of transformation of AlNi to Al_3Ni_2 is still not clear.

Figure 5.6 shows the ratio of Al_3Ni/Al_3Ni_2 as a function of cooling rate. It is obvious that the ratio decreases and is better predicted by the Scheil-Gulliver model as the cooling rate increases.

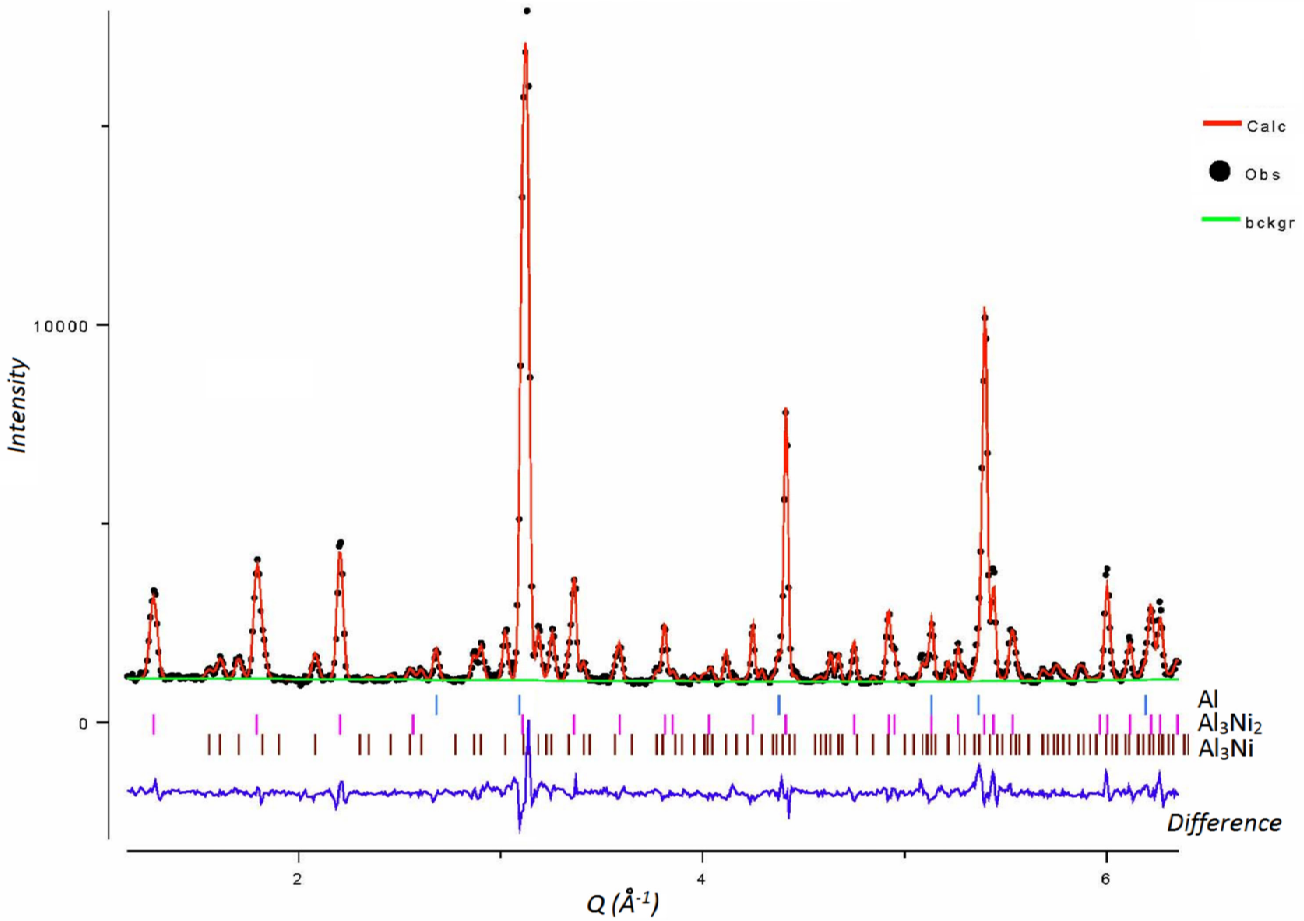

Figure 5.5. Profile refinement of Al-50 wt%Ni with the diameter of 328 μm and cooled in helium using the GSAS computer code. The top line shows the calculated diffraction pattern as obtained from GSAS software and the bottom line represents the difference between the observed and calculated diffraction pattern. The small vertical bars indicate the positions of diffraction peaks of the Al_3Ni_2 (top), Al_3Ni (middle) and Al (below). wRp=%6.79, χ^2=8.92

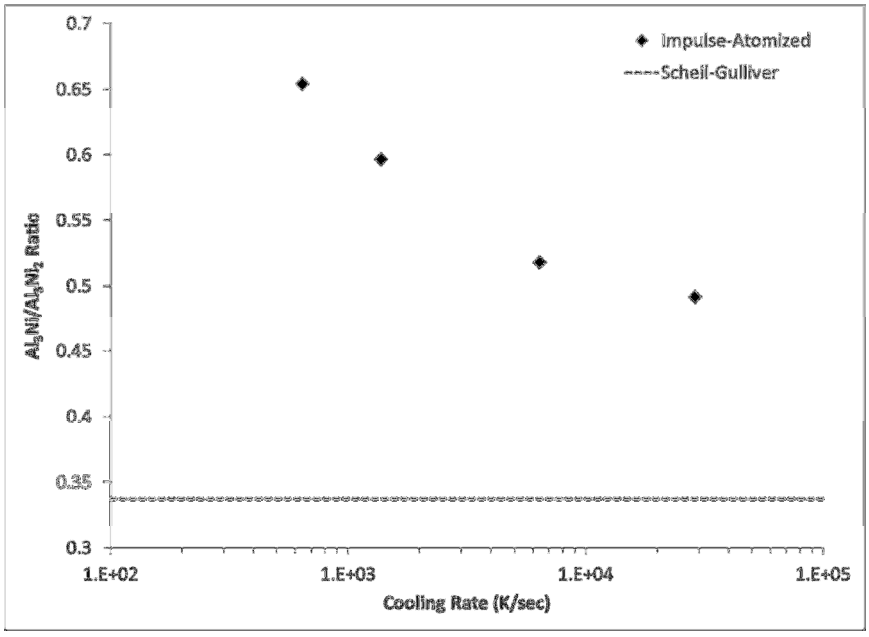

Figure 5.6. Ratio of Al_3Ni/Al_3Ni_2 as a function of cooling rate.

5.3.3. Optical Microscopy and X-Ray Micro-Tomography

Optical images of more than 30 particles from each of different sizes were analyzed using the image processing software called ImageJ. Since the images were high contrast, and the porosity appeared black, the measurement of the porosity within each particle was straightforward. Figure 5.8 shows sample cross sections of particles having 181 and 925 μm diameters of Al-50 wt%Ni, atomized in helium. From the figure, for larger particles (lower cooling rates) the distribution of porosity is different than that of smaller particles. In smaller particles, such as that in Figure 5.7a, 181 μm diameter, porosity tends to form closer to the periphery of the particle, whereas in larger particles, 925 μm diameter (Figure 5.7b), the pores are more randomly distributed. Also, as the microstructure is refined due to higher cooling rate, the size of the individual

pores decreases. Figure 5.8 shows the variation of the area fraction of porosity in Al-50 wt%Ni measured using image analysis on both optical microscope images and X-ray micro-tomography images (discussed below) as a function of cooling rate. It seems that the fraction of porosity increases with decreasing cooling rate.

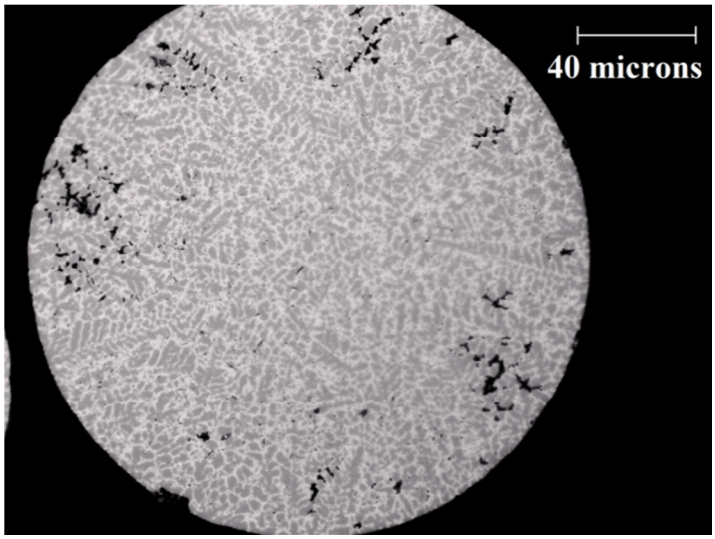

(a)

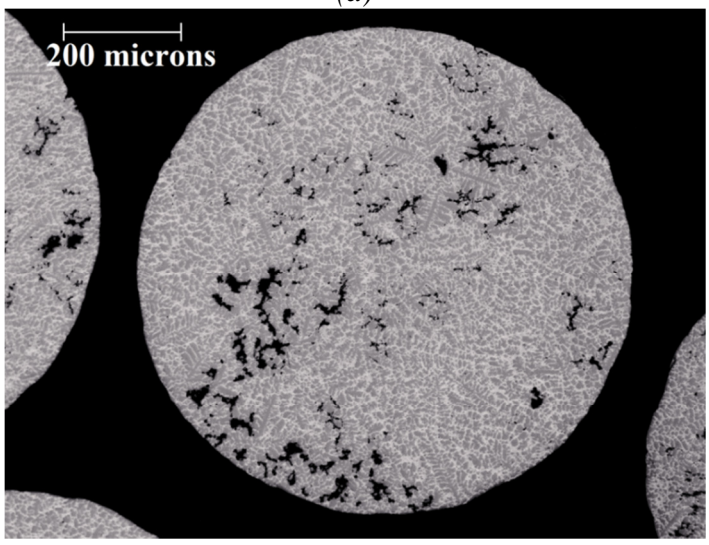

(b)

Figure 5.7. Optical microscopy images of Al-50 wt%Ni particles atomized in helium. (a) 181 μm, (b) 925 μm.

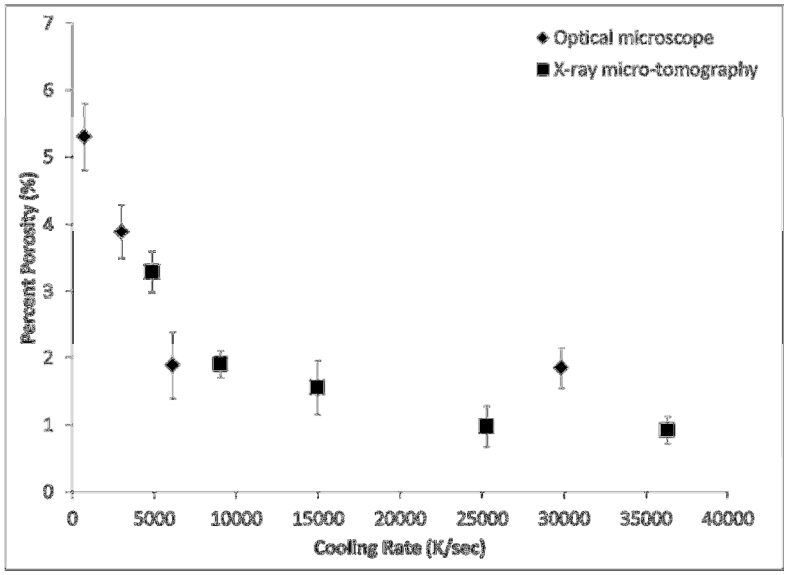

Figure 5.8. Variation of area fraction of porosity as a function of cooling rate from optical microscopy and X-ray micro-tomography.

However, 2D methods are limited by the small number of sections that can be viewed for a given sample. Also, since the intermetallics are quite brittle, not all porosity may be due to solidification shrinkage. Some may result from material loss during sample preparation. Therefore, a 3D method has obvious advantages over conventional 2D approaches. X-ray micro-tomography was used to gather 3D information on rapidly solidified atomized Al-Ni droplets. From the analysis performed on X-ray micro-tomography images it was found that porosity tends to form closer to the periphery in droplets cooled in helium compared with those cooled in nitrogen, as is visualized in Figure 5.9. In this figure, two 328 μm diameter particles are shown. The particle in Figure 5.9a was atomized in helium while the particle in Figure 5.9b was atomized in nitrogen. Quantitative analysis of these images revealed that the volume percent of the porosity decreases with

increasing cooling rate (Figure 5.8).

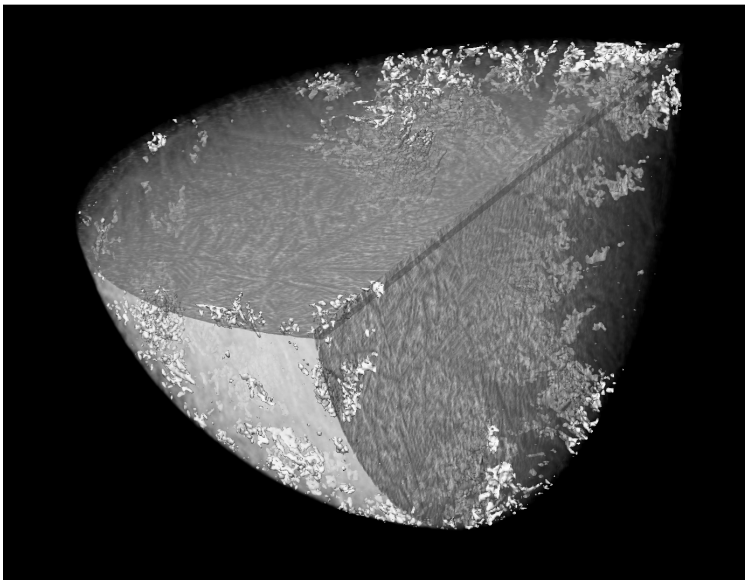

(a)

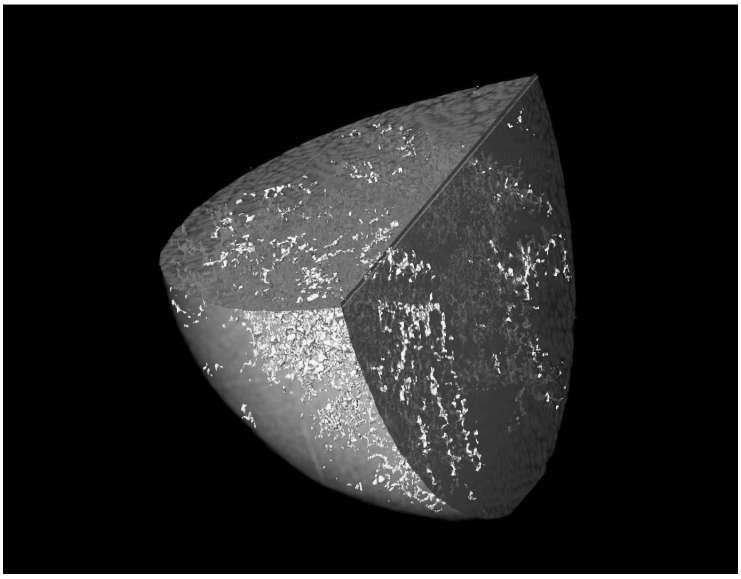

(b)

Figure 5.9. Visualization of the porosity within two particles of 328 μm diameter, atomized in helium (a) and nitrogen (b).

5.4. Discussion

5.4.1. Effect of Cooling Rate on Microstructure and Phase Selection

The results show that increasing cooling rate as a result of decreasing particle size, or using helium instead of nitrogen, refines the microstructure, as it seen in Figures 5.2 and 5.3. Since the thermal conductivity of helium is significantly higher than that of nitrogen [5.17] this was an expected outcome.

One interesting point of Figure 5.2 is the morphology of the Al_3Ni phase. This figure shows that Al_3Ni does not completely envelop Al_3Ni_2 (Figure 5.2b). This was also observed by Patchett and Abbaschian [5.4]. This is in contrast to the conventional understanding of peritectic formation, in which the formation of an envelope of the peritectic phase around the primary phase immediately after its nucleation is assumed [5.18]. In the case of Al-Ni alloys, this special type of peritectic phase growth and the observation of eutectic in the intergranular region lead to this conclusion that a three phase contact between liquid and two solids remains throughout solidification prior to eutectic formation. This results in enhanced dissolution of the primary phase. At high cooling rates however, SDAS decreases and reduces the space for the three phase contact. As a result, the gap between the arms is filled by the peritectic product faster and less dissolution of the primary phase occurs.

On the other hand, St John and Hogan [5.20] propose that the rate at which a peritectic reaction goes to completion is directly related to the shape of the peritectic region on the phase diagram. In the case of Al_3Ni, having an exact

stoichiometric composition eliminates the strong influence of a composition gradient within the peritectic product. As a result, the rate of transformation becomes extremely slow. Since the peritectic reaction is a time dependent process, this complication causes a reduction of the peritectic product at higher cooling rates, which is observed in Figures 5.6.

5.4.2. Effect of Phase Selection on Porosity Formation

Growth of Al_3Ni results in narrower feeding channels for the liquid. This is because Al_3Ni forms around the primary dendrite, Al_3Ni_2, which itself has experienced a relatively long solidification interval. Also, as it is observed in Figure 5.2b, after nucleation occurs as a result of peritectic reaction, the Al_3Ni grows freely into the liquid, which results in completely isolating the liquid in the inter-dendritic region. Since the dendrite arm spacing is larger at lower cooling rates, the size of individual porosity also increases, as also illustrated in Figure 5.7.

Using micro-tomography has the advantage of providing 3-D data in a non-destructive manner. The result of micro-tomography not only helped measure the amount of porosity within particles, but it also allowed for visualizing the distribution of porosity inside the particles by using the image processing technique mentioned in the previous section. From this analysis, it was found that both volume percent porosity as well as porosity distribution vary with the cooling rate (Figures 5.7-9). It seems that in the range of cooling rates that the

particles of Al-50 wt%Ni experienced during IA, volume percent of porosity is directly related to the weight fraction of Al_3Ni.

5.4.3. Lattice parameter of Al_3Ni_2

In the previous chapter, effect of cooling rate on the lattice parameter of Al_3Ni_2 in Al-36 wt%Ni was studied. In this section similar analysis will be performed for Al-50 wt%Ni and the results will be compared with that from the previous chapter.

Figure 5.11 illustrates the effect of cooling rate on the lattice parameter ratio (*c/a*) of Al_3Ni_2 in droplets of Al-36 wt%Ni (from previous chapter) and Al-50 wt%Ni.

For Al-36 wt%Ni, the Al_3Ni_2 is a metastable phase at room temperature. Also, the *c/a* ratio for this phase is significantly smaller than 1.2132, the stoichiometric *c/a* ratio of Al_3Ni_2, and it decreased with increasing cooling rate. On the other hand, for Al-50 wt%Ni, the Al_3Ni_2 is a stable phase at room temperature. The *c/a* ratio in this alloy is much closer to the stoichiometric *c/a* ratio and it appears that it increases with increasing cooling rate.

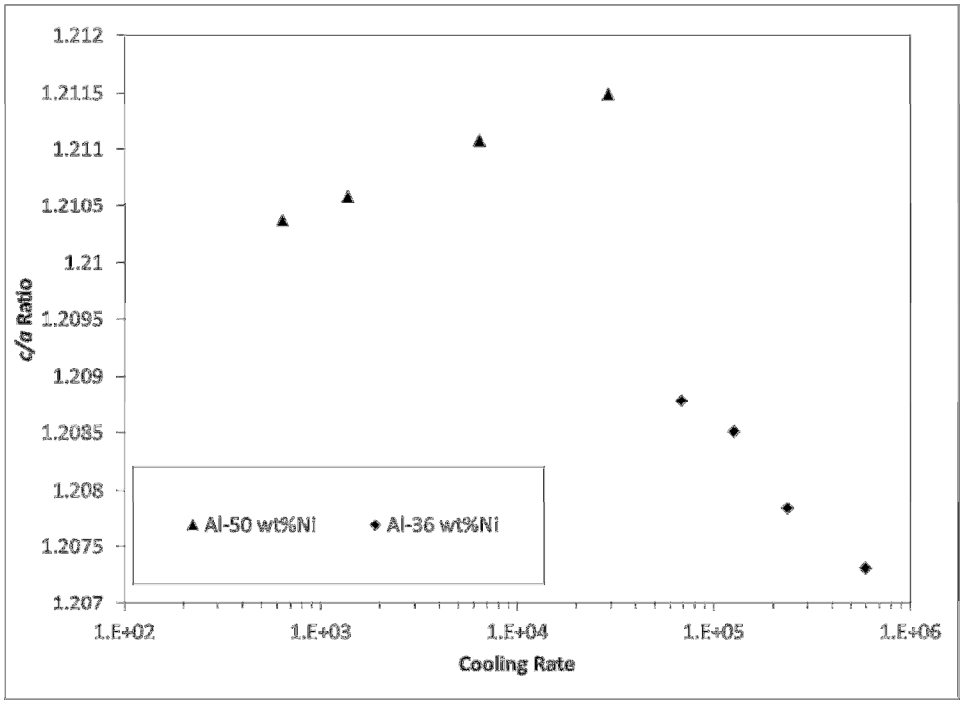

Figure 5.10. Lattice parameter ratio (*c/a*) of the phase Al_3Ni_2 in Al-50 wt%Ni (top) and Al-36 wt%Ni (bottom).

From the phase diagram, it is obvious that the atomic percent of Ni within the Al_3Ni_2 that forms from AlNi is higher than that in the Al_3Ni_2 which forms directly from the liquid. This can result in an increase of the *c/a* ratio as there are more nickel atoms in the lattice of Al_3Ni_2. Also, it is possible that the observed differences are due to different formation mechanisms of Al_3Ni_2 in these alloys. In Al-36 wt%Ni, the Al_3Ni_2 phase forms directly from the liquid. In Al-50 wt%Ni, it forms from the peritectic reaction of AlNi with the liquid. Also, in Al-50 wt%Ni, during the transformation of AlNi to Al_3Ni_2, increasing the cooling rate may not allow for the substitution of nickel atoms by aluminum atoms; therefore, the *c/a* ratio increases and it approaches the stoichiometric value of that in Al_3Ni_2.

5.5. Summary

Findings from this chapter contribute to better understanding of the effects of cooling rate on peritectic reactions, especially in a system with two of such reaction. These effects include changes in microstructure, phase fractions and porosity formation.

Al-50 wt%Ni was atomized in stagnant helium and nitrogen using the IA technique. A finer microstructure was achieved in the smaller particle sizes. Using helium instead of nitrogen also resulted in a refined microstructure. Rietveld analysis on ND data of the particles studied showed that only three phases (i.e. Al_3Ni_2, Al_3Ni and Al) formed in the particles.

Increasing the cooling rate decreased the weight fraction of Al_3Ni and it increased the weight fraction of Al_3Ni_2.

Optical microscopy and X-ray micro-tomography were used to investigate the effect of cooling rate on the formation of the porosity. It was found that in smaller particles, porosity tends to form closer to the periphery of the particles, whereas in larger particles the pores are more randomly distributed.

At lower cooling rate Al_3Ni seems to grow freely into the melt. This can isolate the liquid in the inter-dendritic region, which causes more porosity.

In the next chapter, solidification of Al-Ni alloys produced using other systems will be studied.

5.6. References

5.1. Sumida, M., "Evolution of Two Phase Microstructure in Perotectic Fe-Ni Alloy", Journal of Alloys and Compounds, Vol. 349, Issue 1-2, (2003), 302-310.

5.2. Liu, Y., Lan, F., Yang, G. and Zhou, Y., "Microstructural Evolution of Rapidly Solidified Ti-Al Peritectic Alloy", Journal of Crystal Growth, Vol. 271, Issues 1-2, (2004), 313-318.

5.3. Devred, F., Gieske, A. H., Adkins, N., Dahlborg, U., Bao, C. M., Calvo-Dahlborg, M., Bakker, J. W., Nieuwenhuys, B. E., "Influence of Phase Composition and Particle Size of Atomised Ni-Al Alloy Samples on the Catalytic Performance of Raney-type Nickel Catalysts", Applied Catalysis A: General, Vol. 356, No. 2, (2009), 154-161.

5.4. Patchett, J. A. and Abbaschian, G. J., "Solidification of Nickel Aluminides at Rapid Rates", Proceeding of the Fourth Conference on Rapid Solidification Processing: Principles and Technologies, Edited by R. Mehrabian and P. A. Parrish, U. of California, Santa Barbara, CA, USA, (1986).

5.5. Bao, C. M., Dahlborg, U., Adkins, N., Calvo-Dahlborg, M., "Structural Characterization of Al-Ni Powders Produced by Gas Atomisation", Journal of Alloys and Compounds, 481, (2009), 199–206.

5.6. Tourret, D., Gandin, Ch.-A., "A generalized segregation model for concurrent dendritic, peritecticand eutectic solidification", Acta Materialia, 57, (2009), 2066–2079.

5.7. Siquieri, R., Doernberg, E., Emmerich, H. and Schmid-Fetzer, R., ”Phase-field Simulation of Peritectic Solidification Closely Coupled with Directional Solidification Experiments in an Al-36wt% Ni alloy”, Journal of Physics: Condensed Matter, 21, (2009), 464112 (6pp).

5.8. Henein, H., “Single Fluid Atomization through the Application of Impulses to a Melt”, Materials Science and Engineering: A, Vol. 326 (1), (2002), 92-100.

5.9. Wiskel, J. B., Henein, H. and Maire, E., “Solidification study of Aluminum Alloys Using Impulse Atomization: Part I: Heat Transfer Analysis of an Atomized Droplet”, Canadian Metallurgical Quarterly, Vol. 41, No. 1, (2002), 97-110.

5.10. Nash, P., Singleton, M. F. and Murray, J. L., Phase Diagrams of Binary Nickel Alloys. In: ASM, Materials Park, OH, (1991), 3.

5.11. Standard test methods for metal powders and powder metallurgy products 1993 Metal Powder Industries Federation (Princeton, NJ).

5.12. Von Dreele, R. B., Neutron Diffraction in Materials Science and Technology: A Comprehensive Treatment, Vol. 2B, Wiley–VCH, New York, NY, (1994).

5.13. Johansson, J., Ilbagi, A., Thornton, D. and Henein, H., “Processing 3D Data Sets from X-Ray Tomography of Impulse Atomized Metal Particles”, TMS Annual Meeting, Seattle, WA, USA, (2010).

5.14. Shuleshova, O., Holland-Moritz, D., Loser, W., Reinhart, G., Iles, G. N. and Buchner, B., “Metastable Formation of Decagonal Quasicrystals

during Solidification of Undercooled Al-Ni Melts: In Situ Observations by Synchrotron Radiation", EPL, Vol. 86, 2009, 36002.

5.15. Jones, H., Rapid Solidification of Metals and Alloys, The Institution of Metallurgists, London, (1983), 40-43.

5.16. Kurz, W. and Fisher, D.J., Fundamentals of Solidification, Trans Tech Pub., (1989), 88.

5.17. Rohsenow, W. M., Hartnett, J. P., Cho, Y. I., Handbook of Heat Transfer, 3rd Edition, (1998), McGraw-Hill.

5.18. Kerr, H. W., Cisse, J. and Bolling, G. F., "On Equilibrium and Non-Equilibrium Peritectic Transformation", Acta Metallurgica, Vol 22, (1974), 677.

5.19. St John, D. H. and Hogan, L. M., "A Simple Prediction of the Rate of the Peritectic Transformation", Acta Metallurgica, Vol. 35, Issue 1, (1987), 171-174.

5.20. Han, Q., Shrinkage Porosity and Gas Porosity, Casting, Vol 15, ASM Handbook, ASM International, (2008), 370–374.

Chapter 6

6. Microstructural analysis of Al-Ni alloys processed using EML and DSC [5]

6.1. Introduction

The materials characteristics are greatly influenced by microstructure evolution during the solidification, which in turn is a function of processing parameters during production. Peritectic reaction is a common solidification reaction that occurs in industrial alloys, such as Fe-C steels and Al-, Cu- and Ti-based alloys [6.1]. Aluminum alloys with nickel are practically significant due to their high temperature strength and heat resistance [6.2] and their catalytic capability [6.3]. However, the final properties of the alloy depend on its constituent phases formed during the solidification process. For example, the activity of Raney nickel catalysts is strongly affected by the amount and morphology of the Al_3Ni [6.3-4].

Recently, modeling of the solidification of Al-rich Al-Ni alloys has attracted the attention of many scientists who try to understand and simulate this important and complex system [6.5-8]. On the other hand, many experimental results have been published about the effects of various processing parameters on the final phase fractions and the evolved microstructure [6.9-11]. Bao et al. [6.9] analyzed gas atomized Al–Ni powders with different compositions on the Al-rich side of the phase diagram. They used ND and X-ray diffraction to identify the existing phases at the surface and in the bulk of the particles. Their results show a

[5] A major part of this chapter will be published as, "Effect of cooling rate on solidification of Al-Ni alloys", Ilbagi, A. et al., ***J. Phys: Conf. Ser.***. Reformatted according to thesis requirements.

significant dependence of phase selection during the solidification of different sized gas atomized particles. Using IA technique, it has been shown that in Al-50 wt-%Ni, by increasing cooling rate, the ratio of Al_3Ni to Al_3Ni_2 decreases, while opposite behavior was observed in Al-36 wt-%Ni [6.10-11].

Although atomization techniques offer containerless undercooling in conjunction with high degrees of cooling rates, the measurement of the whole history of nucleation and growth in these techniques is difficult. Therefore, EML has been extensively used to containerlessly undercool bulk samples to study the solidification of a freely suspended droplet but at small cooling rates. The unique possibility of undercooling bulk samples due to the avoidance of heterogeneous nucleation on container walls coupled with accessibility of the solidifying droplet for direct observation and temperature measurement make the EML technique a powerful tool for solidification studies [6.12]. This technique was used to study the effect of melt undercooling prior to solidification on the dendrite growth velocity of various Al-Ni alloys. The results showed that while on the Ni-rich side, growth velocity increases with increasing undercooling, Al-rich alloys show an unusual decrease in growth velocity with increasing undercooling [6.13]. Since it was already known that the melt stirring due to electromagnetic forces can generate pronounced forced convection [6.14], which in turn would affect the solidification, it was decided to perform the experiment in microgravity. Microgravity conditions provide the advantage of reduced electromagnetic stirring which is essential for the investigation of nucleating kinetics and growth in the absence of convection. The experiment was performed during the sounding

rocket mission TEXUS 44 of the European Space Agency (ESA) and the German Aerospace Center (DLR). TEXUS sounding rocket missions provide an excellent quality of reduced gravity of the order of 10^{-4}g [6.15]. An Electro-Magnetic Levitator (EML) for use in reduced gravity environment (TEMPUS-EML) was utilized to process the sample in reduced gravity [6.16].

In this paper, solidification of Al-50 wt-%Ni and Al-36 wt-%Ni produced using different techniques will be studied. Solidification of both alloys in slow cooling rate condition in a furnace, high cooling rate condition during free-fall in a drop tube and high undercooling condition in reduced gravity on-board of the TEXUS 44 rocket will be discussed.

6.2. Experimental

6.2.1. Solidification at Low Cooling Rates

In order to compare the microstructure of IA samples to those solidified in near equilibrium conditions, 30 mg of IA particles of Al-36wt-%Ni and Al-50wt-%Ni with diameter of 750 μm were completely melted again by increasing the temperature to 1773 K. This was done in a Setaram Labsys Evo Differential Scanning Calorimetry (DSC). The DSC had been calibrated for temperature and heat measurement for the entire temperature range using standard samples of Zn, Sn, Al, Ag, Au and Ni. The molten samples solidified at two different cooling rates of 0.08 K/sec and 0.33 K/sec. To study the microstructure, a Zeiss Evo MA15 SEM with 20 keV electron beam energy was used. Image analysis was then performed on the SEM micrographs to find out the volume fraction of each

phase. This analysis was performed by ImageJ, a public domain Java image processing program [6.17].

6.2.2. Heat treatment of Al-50 wt-%Ni.

The effect of heat treatment on the phase fractions in IA particles of Al-50 wt-%Ni was investigated at Oak Ridge National Laboratory using a neutron beam of 1.33 Å wavelength. The particles of 780 µm diameter were put into a vanadium capsule that was placed inside a furnace. The measurements were performed at 100 °C steps up to 500 °C. At each step the sample was held for 2 hours while the ND experiment was being performed. The heating rate was set to 3 °C/minute. The reason for performing this experiment will be discussed later in this chapter.

6.2.3. Solidification under Microgravity

The TEMPUS facility, which is designed for EML in reduced gravity [6.16], has been integrated into a sounding rocket. TEXUS sounding rockets provide about 320 seconds of reduced gravity time. The crystallization front velocity of Al-50wt-%Ni in the undercooled liquid phase was measured during the TEXUS44 sounding rocket flight [6.9]. Three undercooling and solidification cycles were obtained. The sample was heated by more than 200 K above the liquidus temperature of this alloy in order to reduce and even eliminate Al-Oxides at the surface of the liquid drop, which can act as heterogeneous nucleation sites of high catalytic potency. The sample undercooled during the subsequent solidification

cycles to ΔT_1=185 K and ΔT_2=220 K, respectively. The TEXUS 44 sample was then studied using SEM and ND. Image analysis using the software ImageJ was also used to find the volume fraction of the phases in the TEXUS sample.

6.3. Results and Discussion

6.3.1. Solidification at slow cooling rates

Figure 6.1 shows the microstructure of two Al-36 wt-%Ni particles solidified with cooling rates of 0.08 K/sec (Figure 6.1a) and 0.33 K/sec (Figure 6.1b). It can be seen that the particle cooled at higher cooling rate has a finer microstructure. On the other hand, in both images three distinct features can be observed. From the phase diagram, it was expected to have only the pro eutectic Al_3Ni and the eutectic microstructure. However, both particles, although cooled with relatively slow cooling rates, contain a light grey phase, which energy dispersive X-ray (EDX) spectroscopy revealed to be close to Al_3Ni_2. Therefore, it is shown that even in cooling rates as low as 0.08 K/sec, the peritectic reaction between Al_3Ni_2 and liquid does not go to completion. This is not surprising since peritectic reactions need diffusion in solid and therefore behave very sluggishly [6.18]. The DSC curves achieved during the cooling cycle Al-36 wt-%Ni particles also showed a larger exothermic peak for the eutectic transformation in the sample cooled at higher cooling rate. The DSC curves are shown in Figure 6.2.

Figure 6.3 shows the microstructure of two Al-50 wt-%Ni particles solidified at cooling rates of 0.08 K/sec (Figure 6.3a) and 0.33 K/sec (Figure

6.3b). In both figures, Al_3Ni_2, the light grey phase, and Al_3Ni, the dark grey phase, were identified using EDX. It was also noticed that in the particles solidified under the lower cooling rate (0.08 K/sec), visually no eutectic structure can be found. It must be noted that the equilibrium phase diagram does not predict any eutectic transformation for this alloy. However, in the particle that solidified at 0.33 K/sec cooling rate, eutectic microstructure can be seen. This can be further investigated by looking at the DSC results. The DSC curves shown in Figure 6.4 present the cooling cycle of Al-50 wt-%Ni samples. A significant exothermic peak is visible in the sample cooled at 0.33 K/sec as a result of the eutectic transformation. This peak is not as large in the sample cooled at 0.08 K/sec. This shows that even though the equilibrium phase diagram does not predict any eutectic transformation for this composition, eutectic microstructure still forms even in the slow cooling rate used in this study. An increase in the cooling rate from 0.08 K/sec to 0.33 K/sec resulted in increased formation of eutectic microstructure.

It is also interesting that even at such low cooling rates eutectic undercooling occurs. In the sample cooled at 0.08 K/sec eutectic undercooling is almost 10 K whereas in the sample cooled at 0.33 K/sec this value is about 30 K.

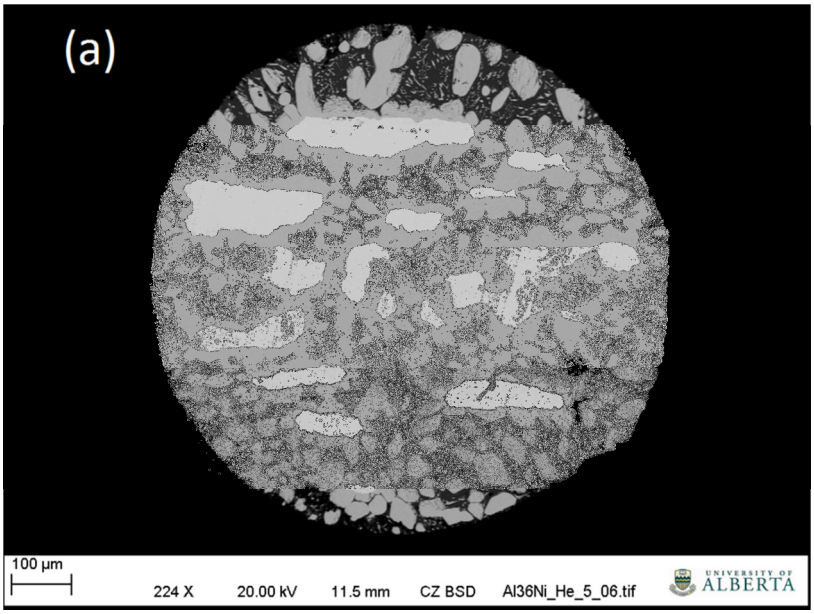

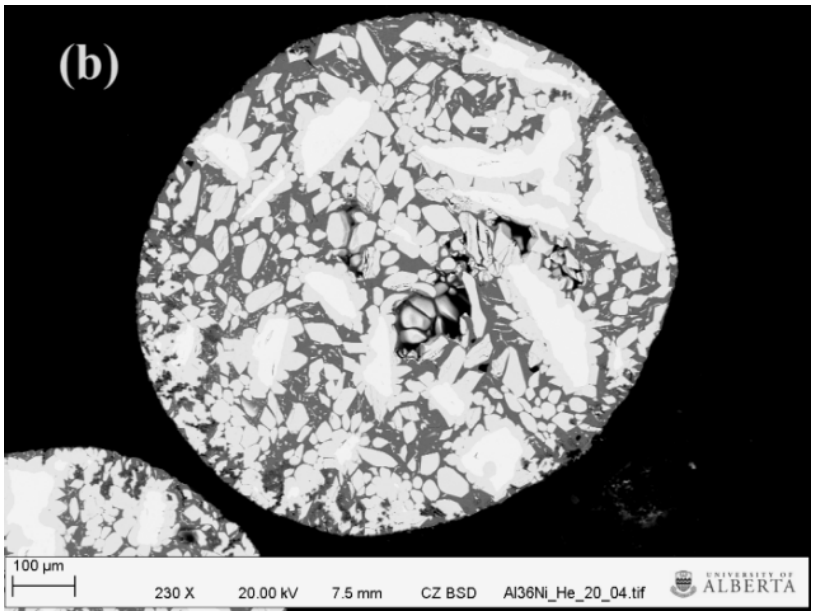

Figure 6.1. SEM micrograph of Al-36 wt-%Ni particles solidified under cooling rates of 0.08 K/sec (a) and 0.33 K/sec (b).

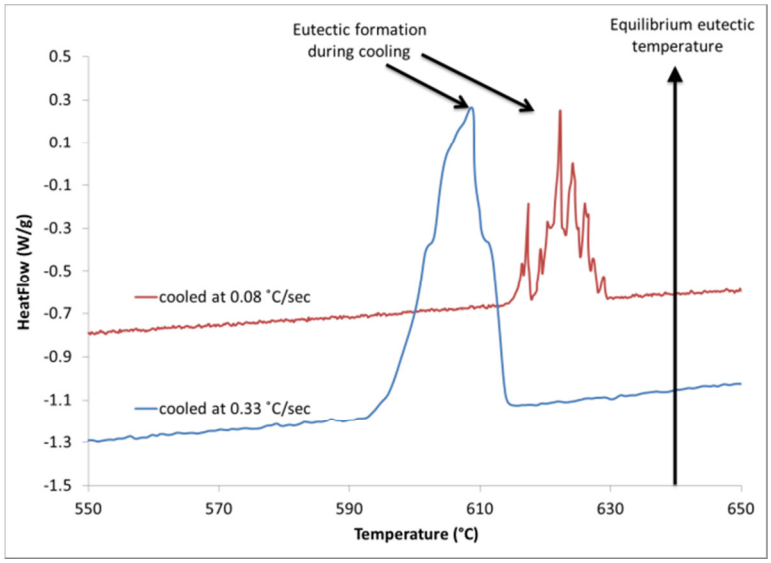

Figure 6.2. DSC curves during cooling for Al-36 wt-%Ni at two different cooling rates showing the exothermic peak for eutectic transformation.

6.3.1.1. Validation of the values used for Γ and D

Since a known value of cooling rate is imposed during solidification of samples solidified in the DSC, the values used for Γ and D in Chapters 4 and 5 can be evaluated. By using the assumed values in the coarsening model along with measured values of SDAS from a DSC sample, one can determine an imposed cooling rate and compare it to the actual value. Lines were drawn parallel to few dendrites observed in Al-50 wt%Ni solidified at 0.33 K/sec (Figure 6.5) and the distance between dendrites was measured using ImageJ 1.45h. Then, using the coarsening model discussed in Chapter 4, the cooling rate was calculated to be 0.53 K/sec. This value is reasonably close to the imposed values of 0.33 K/sec for this sample and provides evidence of the validity of the assumed values of Γ and D.

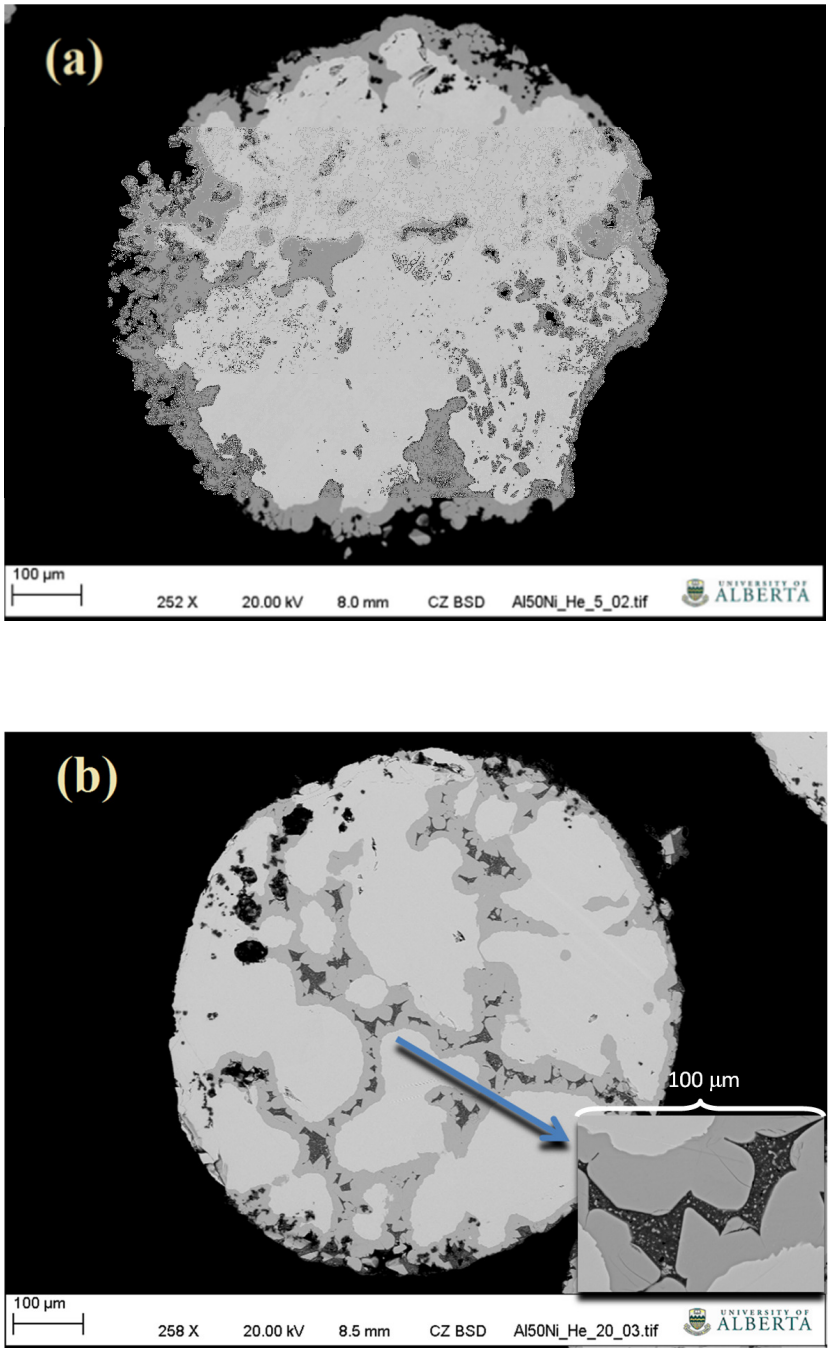

Figure 6.3. SEM micrograph of Al-50 wt-%Ni particles solidified under cooling rates of 0.08 K/sec (a) and 0.33 K/sec (b).

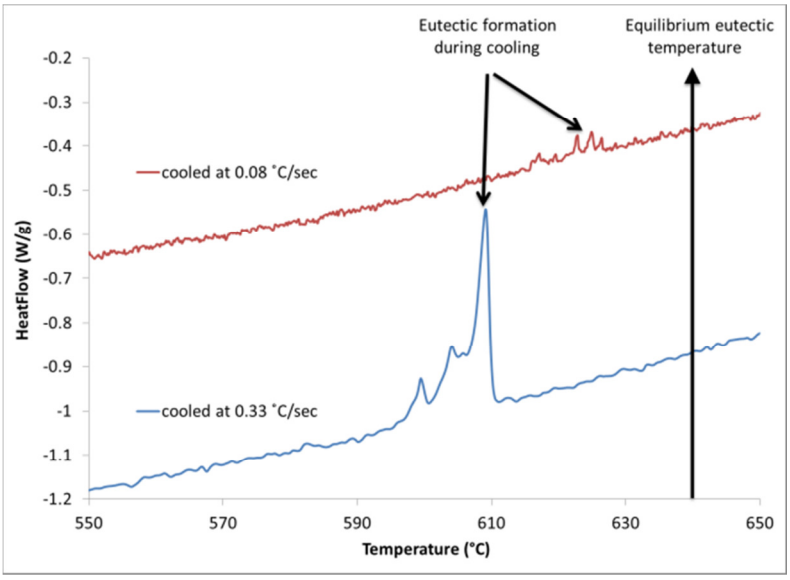

Figure 6.4. DSC curves during cooling for Al-50 wt-%Ni at two different cooling rates showing the exothermic peak for eutectic transformation.

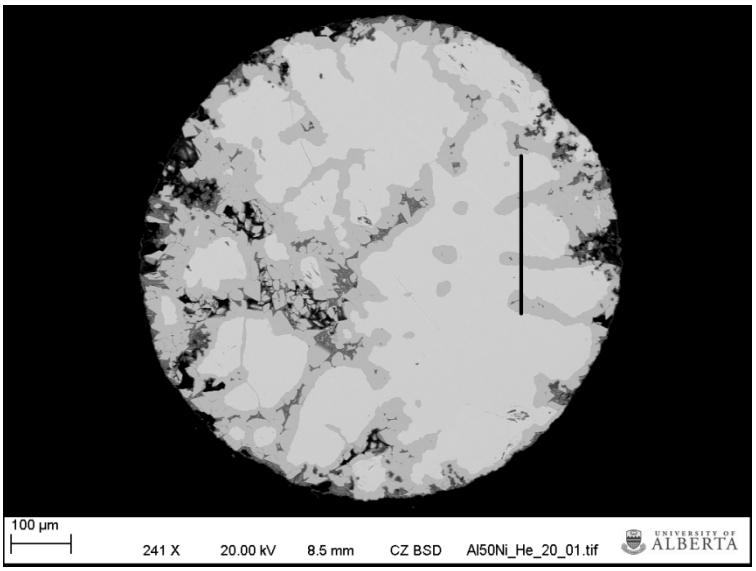

Figure 6.5. SDAS measured for a sample of Al-50 wt%Ni solidified in DSC with imposed cooling rate of 0.33 K/sec.

6. 3.2. Solidification in reduced gravity

The temperature-time profile of the TEXUS specimen, Al-50 wt-%Ni alloy, is shown in Figure 6.6. The spikes on the temperature curve at the beginning of the experiment are due to oxides that were still on the sample's surface. Since oxides show, in general, a higher emissivity than metals the pyrometer signal changes abruptly each time when an oxide layer on the surface of the rotating sample moves through the observation window of the pyrometer. After oxides were eliminated by increasing the temperature, the oscillations of the temperature signal vanished and the sample was cooled until the first recalescence was completed. Then the sample was completely melted again for the second cooling cycle. During this cycle, and shortly after the first recalescence, the reduced gravity period was finished. The primary phase undercooling achieved was ΔT_1=185 K and ΔT_2=220 K for the first and second cycles, respectively. The cooling rate achieved by the sample before the first recalescence of the second cycle was inferred from the temperature-time profile as 14 K/sec, assuming that the slope of the cooling curve was constant in the last 200 K prior to the start of solidification. The cooling rate was further decreased after the first recalescence to 10 K/sec.

The growth velocity of the solidification front in the undercooled liquid was also measured. The result of this measurement was presented elsewhere [6.13]. In brief, performing the experiment on Al-50 wt-%Ni on-board of the TEXUS 44 sounding rocket resulted in observation of two significant and important differences between the experiments in normal gravity and in reduced gravity. First, the growth

velocity measured in reduced gravity is substantially smaller than the data taken under 1g conditions. Second, in reduced gravity, it was apparent that the growth velocity increases with increasing undercooling as usual for a great variety of alloys. In this section the solidification microstructure of the TEXUS 44 specimen will be discussed.

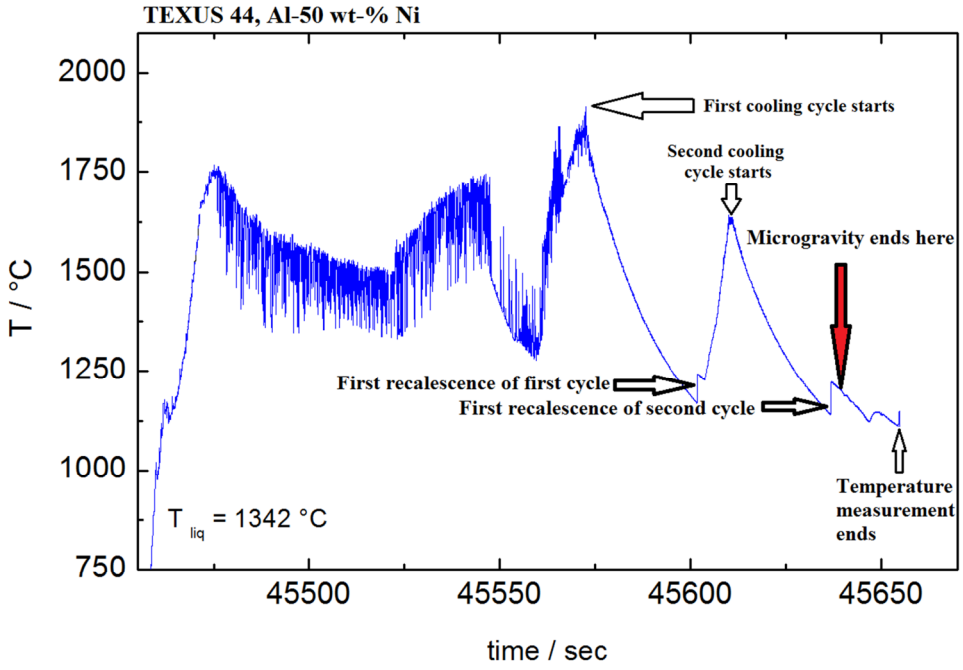

Figure 6.6. The temperature-time profile of the TEXUS 44 specimen.

Microstructural analysis of the solidified specimen showed a distinct difference between the inner part and outer rim of the particle. The microstructure of the TEXUS specimen is shown in Figure 6.7. The outer rim of the sample contains Al_3Ni_2 primary dendrites surrounded by the peritectic phase Al_3Ni and an interdendritic Al-rich eutectic.

Figure 6.8 shows an SEM micrograph of the inner part of the Al-50 wt-%Ni sample processed during TEXUS 44 flight (in the following denoted as TEXUS sample). The inner part is characterized by large amount of porosity, absence of the Al-rich eutectic and dominant occurrence of the Al_3Ni_2 phase.

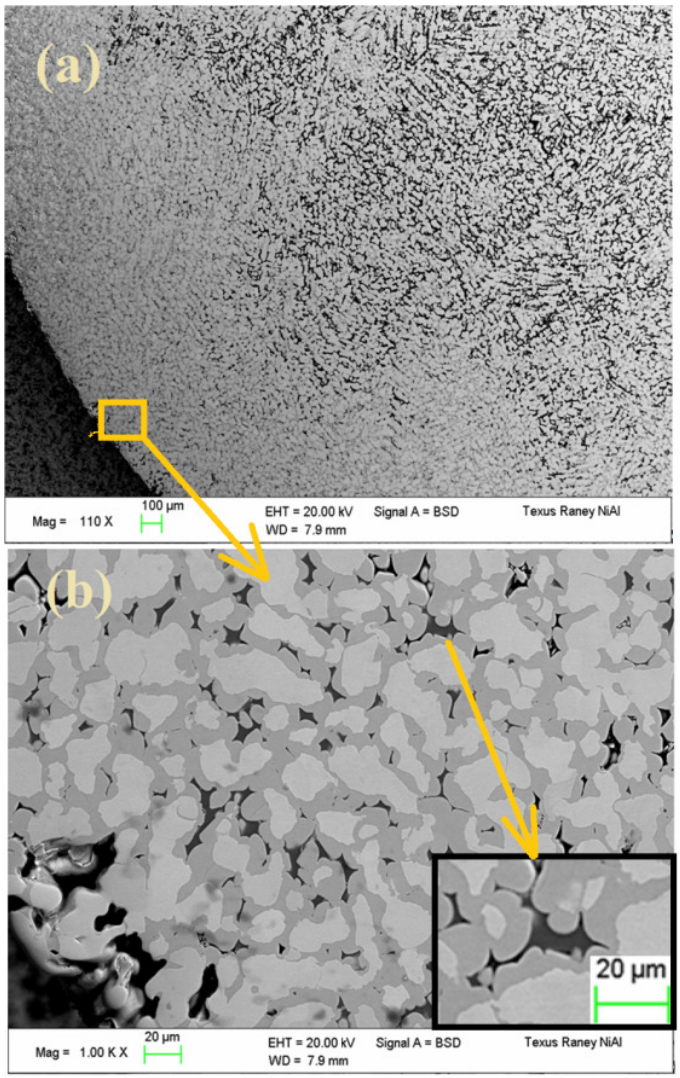

Figure 6.7. a) SEM backscattered electron image of the TEXUS Al-50 wt-%Ni specimen. Outer rim and inner part. b) Outer rim of the specimen shown in (a) in higher magnification.

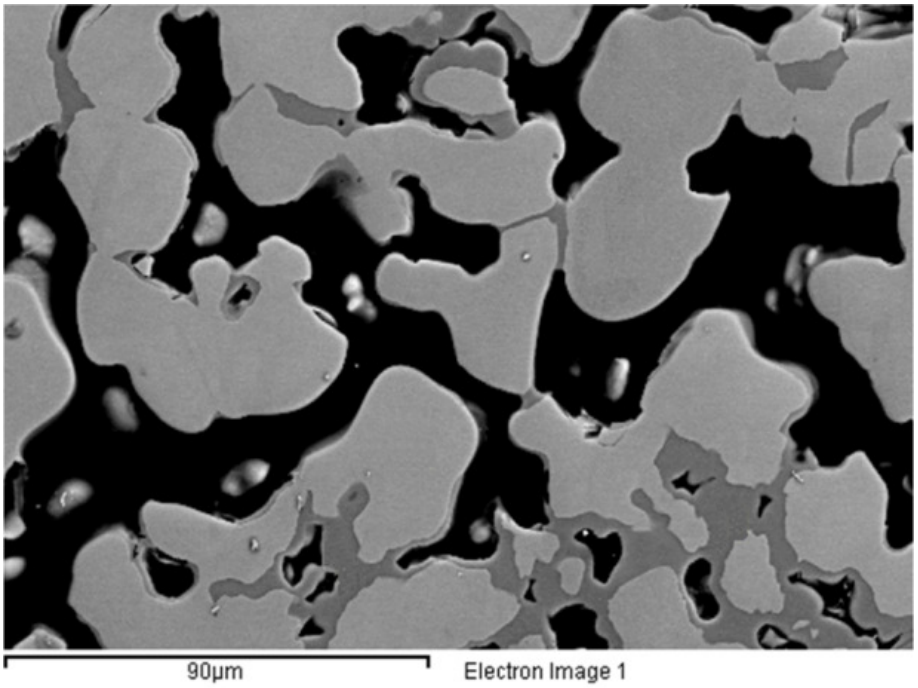

Figure 6.8. SEM backscattered electron image of the inner part of the TEXUS solidified Al-50 wt-%Ni specimen exhibiting the Al_3Ni_2, light grey, and Al_3Ni phase, dark grey. The black areas represent voids.

ND was used to investigate the phases formed within the IA particles (from previous chapters) and the TEXUS sample. Figure 6.9 shows a small range of the diffractograms from all samples superimposed on each other. All peaks found in the diffractogram correspond to the phases Al, Al_3Ni and Al_3Ni_2. From Figure 6.9 it is evident that the TEXUS sample is missing the characteristic (111) peak of Al, a component of the eutectic structure, at 2.68 $Å^{-1}$. Given the high depth of penetration of neutrons in the sample and the absence of Al peak in the diffraction pattern, clearly if any Al is present in the sample, it is below the ND detection limit, which is about 0.5 vol.% [6.19]. It must be noted that the mass loss of the

sample as a result of evaporation of Al during the process is negligible [6.20]. To calculate the mass loss, initial total mass of 641 mg, in which 320.5 mg is Al and 320.5 mg is Ni, was used. The total mass loss as a result of EML processing during TEXUS experiment was found to be less than 0.1 mg. This is because the chamber was filled with argon at 1.01 bar to ensure a clean environment inside the chamber during the flight. Measurement of the sample's mass before and after the experiment also showed no significant difference; therefore, evaporation of Al was not the cause for disappearance of Al peak from ND patterns.

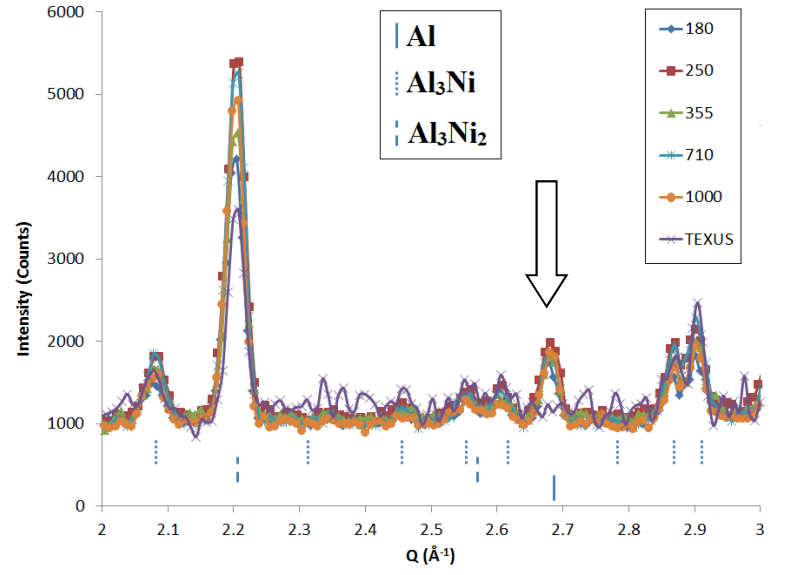

Figure 6.9. Neutron diffractogram of various particle sizes of IA Al-50 wt%Ni and the TEXUS sample, showing the absence of the Al peak in the TEXUS sample.

6.3.3. Phase quantification

SEM micrographs from the samples solidified in the DSC and the TEXUS samples were further investigated using ImageJ to find the volume fraction of

consisting phases. For this purpose, from each of the samples solidified in the DSC, ten particles were used for image processing. The average of the phase fractions were then taken and reported as the volume fraction of each phase.

The volume percent of the phases in the inner part and outer rim of the TEXUS sample were also measured from the SEM images of each part. For the cooling rate, from Figure 6.6, it was found that the maximum cooling rate was achieved at the beginning of the solidification, 14 K/sec, which then declined to 10 K/sec after the first recalescence. It is expected that this cooling rate goes further down as more solid forms and releases its latent heat, and also, as the temperature gradient between the droplet and the environment decreases.

Figure 6.10 shows the Al_3Ni to Al_3Ni_2 ratio as a function of cooling rate. The data for TEXUS specimen is drawn with straight lines for each of the inner parts and the outer rim. Both lines were cut off at 14 K/sec since that was the maximum cooling rate achieved.

The first striking feature of Figure 6.10 is the similarity of the Al_3Ni/Al_3Ni_2 ratio in the sample that was cooled at 0.08 K/sec cooling rate in the DSC and that of the inner parts of the TEXUS sample. Also, as it was mentioned in the previous sections, in both samples the eutectic was not observed. Understanding the similarity of the Al_3Ni/Al_3Ni_2 ratio in the inner parts of the TEXUS sample to that of the slow cooled sample requires better understanding of the solidification of both samples. Possible solidification scenarios are now discussed.

The sample that was cooled in the DSC, experienced prolonged time at high temperatures resulting in extended coarsening of the primary phase. This leaves a

little surface area for the nucleation of the peritectic phase Al_3Ni. On the other hand, due to extensive coarsening of the primary phase there is not enough liquid for peritectic reaction to proceed further. These hypotheses can explain why the ratio of Al_3Ni/Al_3Ni_2 is much smaller than that predicted by the equilibrium phase diagram. Increasing the cooling rate, by almost one order of magnitude in the DSC, results in less coarsening and finer structure, which leaves more surface area for Al_3Ni nucleation. That can explain the increase in the Al_3Ni/Al_3Ni_2 ratio. However, larger cooling rate does not allow for further continuation of Al_3Ni growth, as the temperature reaches the eutectic temperature. Therefore, the remaining liquid solidifies into eutectic microstructure (Figure 6.3b).

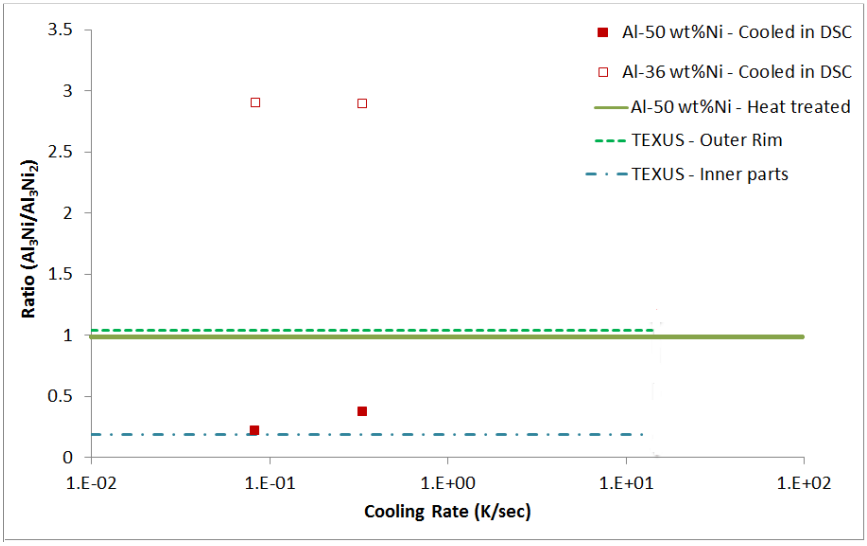

Figure 6.10. The Al_3Ni/Al_3Ni_2 ratio as a function of cooling rate from the image analysis on samples of Al-50 wt-%Ni and Al-36 wt-%Ni alloy produced using DSC (at two cooling rates of 0.08 K/sec and 0.33 K/sec), impulse atomiz ation and EML during TEXUS 44 campaign (only Al-50 wt-%Ni).

In the TEXUS sample, after it experiences 220 K primary phase undercooling, solidification starts from the surface since the heat transfer is highest on the surface, and solid grows towards the inner parts. The initial growth rate is high because of high level of undercooling. However, this high growth rate decreases rapidly as the recalescence increases the sample temperature and decreases the cooling rate. Tourret et al. [6.5] showed that in Al-42 wt%Ni less than 10 vol.% of the solid formed by the end of the recalescence period in which the growth rate is the fastest, while more than 60 vol.% of the solid formed after the recalescence and before the peritectic reaction $L+Al_3Ni_2 \rightarrow Al_3Ni$. The growth rate in this stage is much slower than that during the recalescence. It is expected that the amount of solid formed before the peritectic reaction to be higher in Al-50 wt%Ni alloy. It is argued that the decreasing cooling rate as a result of increasing solid formation and poor heat extraction from the large droplet (~6mm diameter) in the EML chamber [6.21-22], resulted in the formation of large amount of Al_3Ni_2. Therefore, similar to the sample solidified in the DSC, there are not enough surfaces available for the nucleation of Al_3Ni. That is why the ratio of Al_3Ni/Al_3Ni_2 in the inner parts of this sample is low. It is also expected that most of the remaining liquid in the small interdendritic regions to be consumed by the peritectic reaction, and thus, no eutectic region is seen in this sample.

From Figure 6.10 it is clear that the value of Al_3Ni/Al_3Ni_2 ratio in the outer rim of the TEXUS sample is significantly higher than that of other samples studied in this research. As it was discussed, it is expected that the solidification starts from the surface at high growth rate. As a result, the microstructure in this

region is refined and more surface area is available for the Al_3Ni nucleation. However, this cannot justify the high volume fraction of Al_3Ni in this region. It is argued that since this region acted as the heat passage for the entire volume of the specimen, a phenomenon similar to heat treatment has occurred to the phases in the outer rim. To investigate this hypothesis, the ratio of Al_3Ni/Al_3Ni_2 was estimated from the in-situ ND during heat treatment of the Al-50 wt%Ni particles. The results are shown in Figure 6.10 with a straight solid line. It is obvious that both the heat treated samples and the outer rim of the TEXUS sample contain very similar fractions of Al_3Ni and Al_3Ni_2.

In the case of Al-36 wt%Ni, increasing the cooling rate from 0.08 K/sec to 0.33 K/sec did not have a significant effect on the Al_3Ni/Al_3Ni_2 ratio. Although both alloys were cooled at relatively low cooling rates, it was not still enough to transform the entire primary Al_3Ni_2 to Al_3Ni. Increasing cooling rate resulted in microstructural refinement, which provides more surfaces for Al_3Ni nucleation. However, it seems that this effect was offset by higher amount of transformation of Al_3Ni_2 to Al_3Ni at lower cooling rate. It was discussed in previous chapters that the existence of a three point contact between the three phases in this system may result in further transformation of primary Al_3Ni_2. This may explain why at both cooling rates similar ratio of the phases was observed.

6.4. Summary

In this chapter, solidification of Al-Ni alloys was studied using two other techniques than IA that was discussed in the previous chapters. Two different

compositions of Al-Ni alloys (36 and 50 wt-% Ni) were solidified under different conditions. Slow cooling rate in a DSC and IA in a drop tube. Also Al-50 wt-%Ni was solidified on-board of TEXUS 44 sounding rocket using the TEMPUS EML facility for containerless processing of liquid metals in reduced gravity.

From the SEM micrographs it was found that both the inner parts of the TEXUS sample and the sample that was cooled at 0.08 K/sec in a DSC contain almost no eutectic. ND and DSC curves also confirmed this observation.

The outer rim of the TEXUS sample showed the highest amount of Al_3Ni and lowest amount of Al_3Ni_2. This observation was attributed to the reheating of Al_3Ni_2 in that zone during post-recalescence period.

Increasing the cooling rate from 0.08 K/sec to 0.33 K/sec resulted in the formation of some eutectic microstructure and it increased the Al_3Ni/Al_3Ni_2 ratio. The opposite trend was observed in the IA particles at higher cooling rates, where increasing the cooling rate decreased the Al_3Ni/Al_3Ni_2 ratio.

In Al-36 wt-%Ni, increasing the cooling rate from 0.08 K/sec to 0.33 K/sec did not significantly change the volume fraction of the respective phases. However in the IA sample the Al_3Ni/Al_3Ni_2 ratio was increased. Also ND analysis on Al-36 wt-%Ni showed some unidentified peaks in the particles with diameters ≤275 μm. These peaks were attributed to the formation of metastable phases and in particular the D-phase. In larger particle sizes and in the particle sizes studied from Al-50 wt-%Ni this phenomenon was not observed.

6.5. References

6.1. Kerr, H. W., Kurz, W., “Solidification of Peritectic Alloys”, International Materials Reviews, Vol. 41, No. 4, (1996), 129-164.

6.2. Povarova, K. B., Lomberg, B. S., Filin, S. A., Kazanskaya, N. K., Shkol'nikov, D. Y. and Bespalova, M. D., “Structure and properties of Ni-Al-Co system (β+γ)- alloys”, Izvestia Akademii nauk SSSR. Metally, (1994), No. 3, 77-84.

6.3. Devred F, Reinhart G, Iles G N, Van D K, Adkins N J, Bakker J W, Nieuwenhuys B E, “Synchrotron X-ray microtomography of Raney-type nickel catalysts prepared by gas atomisation: Effect of microstructure on catalytic performance”, Catalysis Today, (2011) 163(1) 13-19.

6.4. Devred, F., Gieske, A. H., Adkins, N., Dahlborg, U., Bao, C. M., Calvo-Dahlborg, M., et al. “Influence of phase composition and particle size of atomised Ni-Al alloy samples on the catalytic performance of Raney-type nickel catalysts”, Applied Catalysis A: General, 356(2), (2009), 154-161.

6.5. Tourret, D., Gandin, C.-A., Volkmann, T., Herlach, D. M., “Multiple non-equilibrium phase transformations: Modeling versus electro-magnetic levitation experiment”, Acta Materialia, 59(11), (2011), 4665-4677.

6.6. Tourret, D., Gandin, Ch.-A., “A generalized segregation model for concurrent dendritic, peritecticand eutectic solidification”, Acta Materialia, 57, (2009), 2066–2079.

6.7. Tourret, D. and Gandin, C.-A., “Microsegregation modeling of multiple phase transformations – Atomization of Al-Ni alloys”, in Modeling of Casting, Welding and Advanced Solidification Processes XII, Eds. S. L. Cockcroft and D. M. Maijer, 603-611. T.M.S., Warrendale, Pennsylvania, USA (2009).

6.8. Siquieri, R., Doernberg, E., Emmerich, H. and Schmid-Fetzer, R., ”Phase-field Simulation of Peritectic Solidification Closely Coupled with Directional Solidification Experiments in an Al-36wt% Ni alloy”, Journal of Physics: Condensed Matter, 21, (2009), 464112 (6pp).

6.9. Bao, C. M., Dahlborg, U., Adkins, N., Calvo-Dahlborg, M., “Structural Characterization of Al-Ni Powders Produced by Gas Atomisation”, Journal of Alloys and Compounds, 481, (2009), 199–206.

6.10. Ilbagi, A., Henein, H. and Phillion, A. B., “Phase quantification of impulse atomized Al68.5Ni31.5 alloy”, Journal of Materials Science, (2011) 46:6235–6242.

6.11. Ilbagi. A., Delshad Khatibi. P., Swainson. I. P., Reinhart. G. and Henein. H., “Microstructural analysis of rapidly solidified aluminium-nickel alloys”, Canadian Metallurgical Quarterly, 50(3), (2011), 295-302.

6.12. Herlach, D. M., Galenko, P. and Holland-Moritz, D. Metastable Solids form Undercooled Metls, Pergamon Materials Series, New York, (2007).

6.13. Lengsdorf, R., Holland-Moritz, D. and Herlach, D. M., “Anomalous dendrite growth in undercooled melts of Al-Ni alloys in relation to results obtained in reduced gravity”, Scripta Materialia, 62(6), (2010),

365-367.

6.14. Reutzel, S., Hartmann, H., Galenko, P. K., Schneider, S. and Herlach, D. M., "Change of the kinetics of solidification and microstructure formation induced by convection in the Ni-Al system", Applied Physics Letters, (2007), 07/23;91(4):041913-1.

6.15. Kuhl, R., Friker, A., Friedrichs, D., Gritzner, C., "National report on sounding rocket and balloon research activities within the German space programme", 19th ESA Symposium on European Rocket and Balloon Programmes and Related Research; 7-11 June 2009; Noordwijk, Netherlands: ESA Communication; (2009).

6.16. Piller, J., Knauf, R., Preu, P., Herlach, D. M., Lohöfer, G., "Electromagnetic positioning and inductive heating under micro-g", Sixth European Symposium on Material Sciences under Microgravity Conditions; Proceedings of an International Symposium.; Bordeaux, Fr: ESA; (1987).

6.17. Abramoff, M. D., Magelhaes, P. J., Ram, S. J., "Image Processing with ImageJ", Biophotonics International, 11(7), (2004), 36-42.

6.18. St John, D. H. and Hogan, L. M., "A Simple Prediction of the Rate of the Peritectic Transformation", Acta Metallurgica, Vol. 35, Issue 1, (1987), 171-174.

6.19. Grosse, M., Niffenegger, M. and Kalkhof, D., "Monitoring of low-cycle fatigue degradation in X6CrNiTi18-10 austenitic steel", Journal of Nuclear Materials, 296(1-3), (2001), 305-311.

6.20. Lee, J. and Matson, D., Tufts University, Department of Mechanical Engineering, Private Communication, November 28, (2011).

6.21. Liu, R. P., Volkmann, T. and Herlach, D. M., "Undercooling and solidification of Si by electromagnetic levitation", Acta Materialia, 49(3), (2001), 439-444.

6.22. Filip, O. and Hermann, R., "Phase and microstructure evolution during solidification of Nd-Fe-B melts processed by novel techniques", Journal of Optoelectronics and Advanced Materials, 8(2), (2006), 504-510.

Chapter 7

7. General Discussion, Conclusions and Future Work

7.1. General Discussion and Conclusions

The purpose of the current work was to study the microstructure evolution during solidification of Al-Ni peritectic alloys and to investigate the effects of processing parameters on the phase fractions and porosity formation. To achieve these goals, Al-Ni alloys were generated using different techniques. Characterization was then performed by employing several different techniques. Optical and electron microscopy was used to study the 2D microstructure of the droplets, while other techniques such as ND and X-ray micro-tomography which are capable of sampling the whole volume of the droplets were used for quantification of 3D microstructure. The observations that can be drawn from this research are presented below.

In both Al-36 wt%Ni and Al-50 wt%Ni, it was found that the cooling rate has a significant effect on the formation of microstructure, phase fractions and metastable phase formation. SEM analysis of the produced particles showed that the microstructure is refined as a result of decreasing particle size. Using helium instead of nitrogen also refines the microstructure.

In Al-36 wt%Ni, increasing cooling rate as a result of decreasing particle size resulted in suppression of primary Al_3Ni_2 phase nucleation. Such cooling rate also results in the formation of a quasicrystalline phase known as D-phase, which was identified using ND.

The effect of cooling rate on the phase fractions was also studied. In this chapter a review of the results is presented and they will be compared with the results from other researchers.

Figure 7.1 shows the Al_3Ni to Al_3Ni_2 ratio of both alloys studied in this research that were produced using IA, DSC, EML and other techniques used by other researchers.

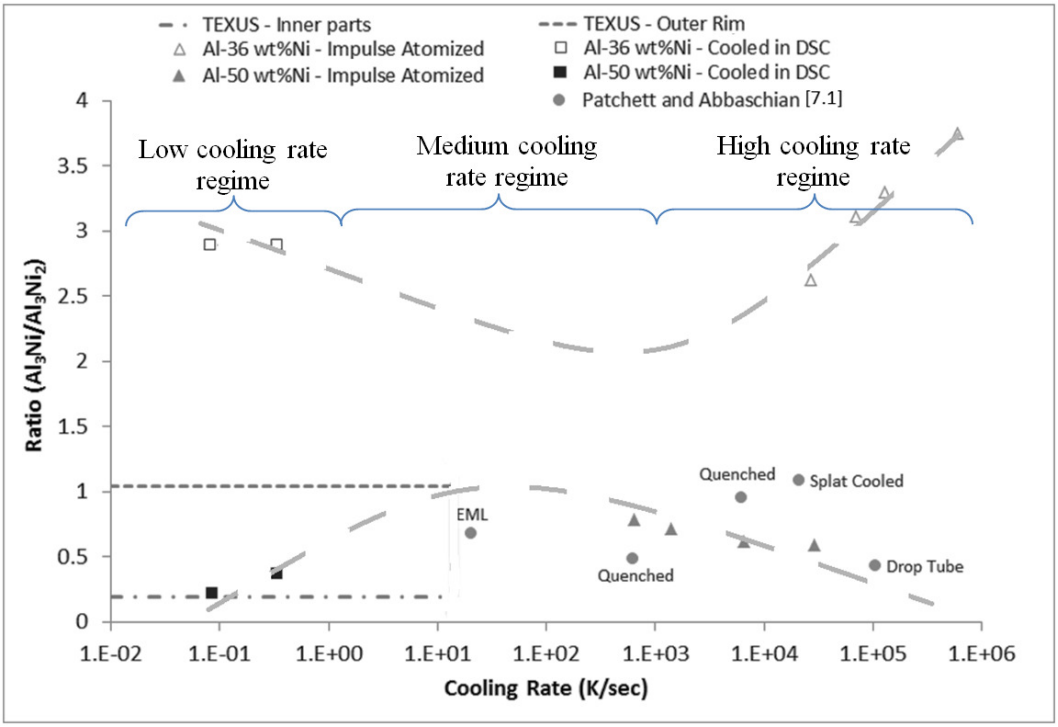

Figure 7.1. The Al_3Ni/Al_3Ni_2 ratio as a function of cooling rate for samples of Al-50 wt%Ni and Al-36 wt%Ni alloy produced using DSC (at two cooling rates of 0.083 K/sec and 0.33 K/sec), IA and EML during TEXUS 44 campaign (only Al-50 wt-%Ni), as well as from the literature.

While in Al-36 wt%Ni the ratio of Al_3Ni/Al_3Ni_2 decreases and then increases with the cooling rate, in Al-50 wt%Ni opposite trend is observed. The curved dashed-lines on Figure 7.1 do not represent any mathematical curve fittings. They were drawn to present the proposed trend of phase fractions as a function of cooling rate in Al-50 wt%Ni and Al-36 wt%Ni. Four factors may be considered for the observed changes:

1. Nucleation and growth kinetics of the primary phase
2. Nucleation and growth kinetics of the peritectic phase
3. Dissolution of the primary phase by the peritectic phase
4. Solid state diffusion

In the case of Al-36 wt%Ni, although no experiment was performed for large range of cooling rates (medium cooling rates), it seems that in the low cooling rate range the ratio is almost constant and at high cooling rate it increases. It is likely that at low cooling rate regime the amount of Al_3Ni_2 increases because there is ample opportunity for it to nucleate and grow. Meanwhile, a slight increase in the cooling rate refines Al_3Ni_2 structure and provides more surface area for the peritectic Al_3Ni to nucleate. It was shown in the previous chapter that there is a three point junction between the primary phase, peritectic phase and the liquid; therefore, in the low cooling rate regime where the contact between the liquid and the primary Al_3Ni_2 persists, which would reduce the amount of Al_3Ni_2. These competing phenomena can define the ratio of the phases at low cooling rate regime.

At high cooling rates, it is not expected that time dependent processes, such as those requiring diffusion, play a major role. Instead, it is believed that the kinetics of nucleation and growth of the primary phase play a major role. High cooling rate reduces the time available for the primary phase to grow, thus the ratio decreases. The Al_3Ni phase grows directly from the liquid and at very high cooling rates, the nucleation of the primary Al_3Ni_2 is suppressed and Al_3Ni nucleates as the primary phase.

The phase selection scenario for Al-50 wt%Ni, however, is somewhat different. In this alloy, at low cooling rate regime, samples experience prolonged time at high temperatures resulting in extended coarsening of Al_3Ni_2. This leaves little surface area for the nucleation of the peritectic phase Al_3Ni. On the other hand, a peritectic reaction can progress by diffusion of constituents through the peritectic phase. Thus, remaining for such long time at high temperature may allow for diffusion to occur. However, due to extensive coarsening of the primary phase there is not enough liquid for peritectic reaction to further proceed. Increasing the cooling rate will result in less coarsening and refine the structure, which leaves more surface area for Al_3Ni nucleation. On the other hand, the time available for diffusion reduces transformation of Al_3Ni_2 to Al_3Ni through peritectic reaction becomes less probable. Also, since the cooling rate is high, the SDAS decreases and the three-point contact between the liquid, Al_3Ni and Al_3Ni_2 diminishes as Al_3Ni fills the secondary dendrite arm space. Hence, at high cooling rate the Al_3Ni/Al_3Ni_2 ratio decreases with increasing cooling rate.

Comparing the results of the techniques used in this research with those reported by Patchett and Abbaschian [7.1] confirms the importance of the processing parameters in the phase fractions of a solidified specimen. While the Al_3Ni/Al_3Ni_2 ratio of the two samples that they studied in a containerless system such as EML and drop tube follows similar trend to that of the TEXUS and IA samples, the results from the quenched and splat cooled samples are significantly different. This may be due to the constrained growth of the solid in the quenched and splat cooled samples, in which the released latent heat is extracted through the solid. In containerless techniques such as EML, IA or drop tube, however, the latent heat is extracted through the undercooled liquid. This can result in different levels of undercooling (primary phase, peritectic and eutectic) for the solidifying phases. Considering the complexity of the Al-Ni system with two peritectic and one non-equilibrium eutectic transformations, it is not surprising that the different levels of undercooling achieved in different techniques resulted in different trend of changes in Al_3Ni/Al_3Ni_2 ratio. Also, the possibility of an anisotropic structure coupled with measurements using microscopy techniques may lead to errors and large scatter in measurements. Further work using 3D quantitative characterization techniques, such as ND, on samples solidified using processes that result in constrained growth is needed.

The effect of cooling rate on the lattice parameter ratio (*c/a*) of Al_3Ni_2 in droplets of Al-36 wt%Ni and Al-50 wt%Ni was also investigated. For Al-36 wt%Ni, the *c/a* ratio for this phase is significantly smaller than 1.2132, the stoichiometric *c/a* ratio of Al_3Ni_2, and it decreased with increasing cooling rate.

On the other hand, for Al-50 wt%Ni, the *c/a* ratio is much closer to the stoichiometric *c/a* ratio and it increases with increasing the cooling rate. It is believed that the changes observed in the *c/a* ratio of Al_3Ni_2 are directly related to the changes discussed above. It was shown that the ratio is reversely dependent on the fraction of Al_3Ni for both alloys. Also, in the case of Al-36 wt%Ni at high cooling rates the ratio departs from the stoichiometric ratio and it is likely that at certain cooling rate it becomes so low that Al_3Ni_2 becomes unstable and as a result, metastable phases form.

X-Ray tomography was used to characterize the microstructure of rapidly solidified particles of Al-36 wt%Ni and Al-50 wt%Ni. From the images obtained, multiple nucleation sites were observed in larger particles, while smaller particles contained only single nucleation point. Also, porosity within the particles was quantified and the distribution of porosity with regard to the nucleation site and cooling rate was discussed. The distribution of porosity within the small particles and large particles was found to be significantly different, which corresponds to the suppression of the primary phase in the smaller particle. Quantitative analysis of the micro-tomography images revealed that the volume percent of porosity increases with increasing particle size. Also, it was found that in smaller particles, porosity tends to form closer to the periphery of the particles, whereas in larger particles the pores are more randomly distributed.

In the case of Al-36 wt%Ni, it was shown that the Al_3Ni/Al_3Ni_2 ratio decreases with increasing particle size (decreasing cooling rate). Therefore, at smaller cooling rate, the alloy experiences larger freezing range, which results in

the formation of more Al_3Ni_2. Formation of more Al_3Ni_2 followed by the peritectic reaction makes the feeding of the shrinkages more difficult, and as a result, the volume percent of porosity increases.

In the case of Al-50 wt%Ni, it was found that growth of Al_3Ni results in narrower feeding channels for the liquid. This is because Al_3Ni forms around the primary dendrite, Al_3Ni_2, which itself has experienced a relatively long solidification interval. Also, after the peritectic phase nucleation, with the decreasing cooling rate the Al_3Ni grows freely into the liquid, which results in completely isolating the liquid in the inter-dendritic region. Since the dendrite arm spacing is larger at lower cooling rates, the size of individual porosity also increases.

The results of this dissertation are valuable as they shed light on the effects of cooling rate on the phase selection during peritectic reaction, which is an important transformation in many industrial alloys. Also, Al-Ni alloys as catalysts used in industry must possess high surface area and a certain ratio of Al_3Ni to Al_3Ni_2 as discussed in Chapter 4. Using the results of this work, optimum conditions for achieving desired properties for the catalysts pre-cursors can be identified. On the other hand, various benefits of 3D characterization techniques for identifying the phases and internal structure of solidified products were outlined and practical techniques for analyzing the images from micro-tomography were discussed.

7.2. Future Work

Based on the findings of the present work, the following subjects can be recommended in particular for further studies:

1. Modeling the solidification of Al-Ni alloys is an important step in better understanding the peritectic reaction phenomenon. Considering the complexity of the system, it is very important to investigate the effect of various degrees of undercooling for the transformations in the system.
2. Measurement of actual cooling rate of falling particles has long been a goal for scientists working on melt atomization. It is suggested that a systematic measurement of particle in-flight characteristics be performed at various heights, in order to investigate the sensitivity of the measurement devices. The result of such measurements coupled with the phase fraction analysis can improve the accuracy of the solidification models.
3. In the literature, solidification of Al-Ni alloys has been investigated using EML. The microstructural analysis of such sample, which was solidified under microgravity, was presented in Chapter 6. However, most of the published works on solidification of these alloys using EML is focused on variation of growth velocity as a function of undercooling. A systematic analysis of microstructure evolution during solidification of these alloys under terrestrial and microgravity conditions is beneficial as it reveals the effect of melt convection and various degrees of undercooling on the microstructure evolution in Al-Ni alloys. By variation of the pressure of

cooling gas in the atomization tower, it is possible to manipulate the level of microgravity achieved during the free-fall of the droplets. The results of such an experiment, when compared to those solidified on the International Space Station, sounding rocket or parabolic flights can help understand the effect of the cooling rate and microgravity on the solidifications of droplets.

4. Al-Ni alloys are used as catalyst. It is suggested that different compositions of Al-rich Al-Ni alloys be produced at different cooling rates to systematically investigate the effect of solidification parameters on the catalytic activity. The results of such analysis can be compared with the existing methods of producing these catalysts in order to achieve the highest catalytic performance.
5. It is suggested that the results of this research work be compared with those achieved using gas atomization. This comparison will illustrate the effects of processing parameters in smaller particle size range and different cooling rates.

7.3. Reference

7.1. Patchett, J. A. and Abbaschian, G. J., "Solidification of Nickel Aluminides at Rapid Rates", Proceeding of the Fourth Conference on Rapid Solidification Processing: Principles and Technologies, Edited by R. Mehrabian and P. A. Parrish, U. of California, Santa Barbara, CA, USA, (1986).

Appendix A

Appendix A1. Processing 3D Data Sets from X-Ray Micro-Tomography of Impulse-Atomized Metal Particles[6]

A1.1 Introduction

Rapid solidification techniques have become more important due to their ability to generate a variety of structures [A1]. The fact that the cooling rate in rapid solidification is extremely high compared to conventional solidification processes results in additional solidification regimes and consequently, differences in the scale of microstructure and morphology. In order to gather information about solidification characteristics one can use conventional 2-D methods such as microscopy. These methods are limited by the small number of sections that can be viewed for a given sample. In addition, a statistically meaningful sampling of 2D sections of anisotropic structures is prohibitive. In these instances, a 3-D method has obvious advantages over conventional 2-D methods. In this research X-ray micro-tomography was used to gather 3-D information on rapidly solidified atomized Al-Ni droplets. Prasad et al. [A2] have used such tomography to obtain details such as nucleation, recalescence and porosity distribution in atomized droplets, which were not possible to achieve in conventional 2-D techniques. Their analysis on porosity was limited to qualitative study of the distribution of

[6] A version of this chapter has been published in proceedings of Three-Dimensional Materials Science VI, 2010 TMS Annual Meeting & Exhibition, Seattle, Washington February 14-18, 2010.

porosities. Later, they were successful in quantitatively measuring the amount of porosities [A3] by calculating the number of pixels with gray scale levels matching that of porosity within the entire droplet volume. However, for particles that had porosity open to the droplet surface they were not able to analyze the volume fraction of the porosities. It was due to the fact that the area surrounding the droplet also had the same grey scale value as that of porosity. Hence, the authors of this paper realized that there was a missing step in the previous analysis. That step, which turned out to be a critical step, is to create a mask file that allows for the separation of the particle from its surrounding without losing much of the surface details. Different methods have been considered and compared to achieve this goal. After the proper method for creating the mask file was found, it was applied to two particles of the same size and composition that were cooled in different gases (N_2 and He).

A1.2. Experimental

Nominal Al-50wt%Ni powders were produced in both nitrogen (sample 090916) and helium (sample 080731) using the IA technique. The details of this technique are described elsewhere [A4]. The powder was sieved and droplets of size range 300-355 μm were chosen for X-ray micro-tomography. The experiment was carried out on the ID19 beam line at the European Synchrotron Radiation Facility (ESRF) in Grenoble, France. Observations were made using X-ray beams of 0.27 μm resolution.

A1.3. Results and Discussion

Using the X-ray micro-tomography technique, data files for the 3-dimensional section of the droplet were generated. The data files are saved with the extension '.raw' indicating that the contents are essentially a large array of numbers with no description of the dimensions or size, in bytes, of each data value. The size of each RAW file ranges from 1GB to 16GB.

Analysis of the data sets involves the following steps:

1. Generate a histogram of the data
2. Locate the minimum data value between peaks. This corresponds to particle and exterior ranges of data values.
3. Do a thresholding operation on the data using the value from step 2. This generates a new data set contain 2 values, one for the particle and one for the exterior. Note that this new data set contains a variety of structures which must be cleaned.
4. Clean the thresholded data set by locating connected regions and filling in the small structures, both on the inside and outside. The result is the mask file which allows us to separate the original data into particle and non-particle regions. Note that this operation is done on each slice of the data set using 2D connection information.
5. Using the original data and comparing to the mask file, quantitative analysis on the particle alone can now be performed.

An illustrated example of these steps will now be described.

Steps 1and 2: Selecting a Minimum Value from a Histogram

The first part of the procedure is to delineate the inside of the particle from the outside of the particle. To accomplish this, the starting point is to generate a histogram for the entire data set. A program was written in the C language, that gives a histogram as a probability distribution, in which, the minimum is selected by searching between the peak values. Figure A1.1 shows an example of a histogram generated for a test case data set. One caution here is that if the data set has been previously edited, such as a case in which there is more than one particle in the data; there needs to be enough of the exterior of the particle to be able to resolve the minimum point between the peaks.

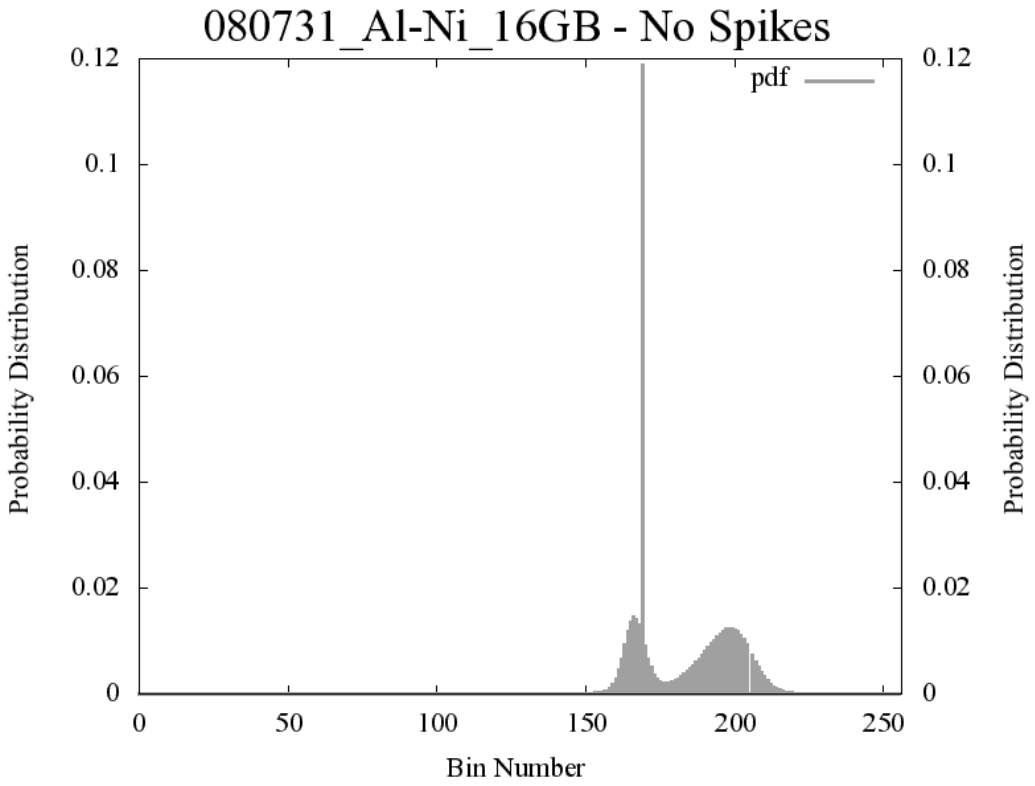

Figure A1.1. Image of the histogram of the test case data set.

Step 3: Threshold

The next step is to run a threshold function on each slice of the data set based on the minimum histogram value to get a binary image, containing only two values (one value for points belonging to the particle, and the other value for exterior points). This operation is straightforward to do with a user written program, and can be done in the tools discussed below. (This step leaves a variety of structures such as porosity or artifacts which must be cleaned up before there is a separation of the particle. The tools used to achieve this goal are:

a. In Avizo® use the Label Voxel() module.
b. In ImageJ the “Image Adjust Threshold” menu item is used.
c. MATLAB® use the function im2bw(), part of the image processing toolbox.

Step 4: Structure removal from thresholded data to create a mask file

In order to generate a mask file, the structural features inside the particle that are still visible must be removed. This is accomplished using any one of the following three approaches:

a) Using Avizo®: The following steps are used to create the mask file: The "Label Voxel" module allows for the removal of interior bubbles and exterior noise - this is simply a matter of filling the holes in the two regions of the data. This is a segmentation operation in Avizo® which separates the data into a set of connected regions, which can then be filled depending on size. Figure A1.2 contains close-ups of two screen shots of slice 1196. The left one is from the black and white image file and the right is from the new mask file. Figure A1.2a

shows a slice after thresholding and Figure A1.2b shows the same slice after segmentation and hole filling.

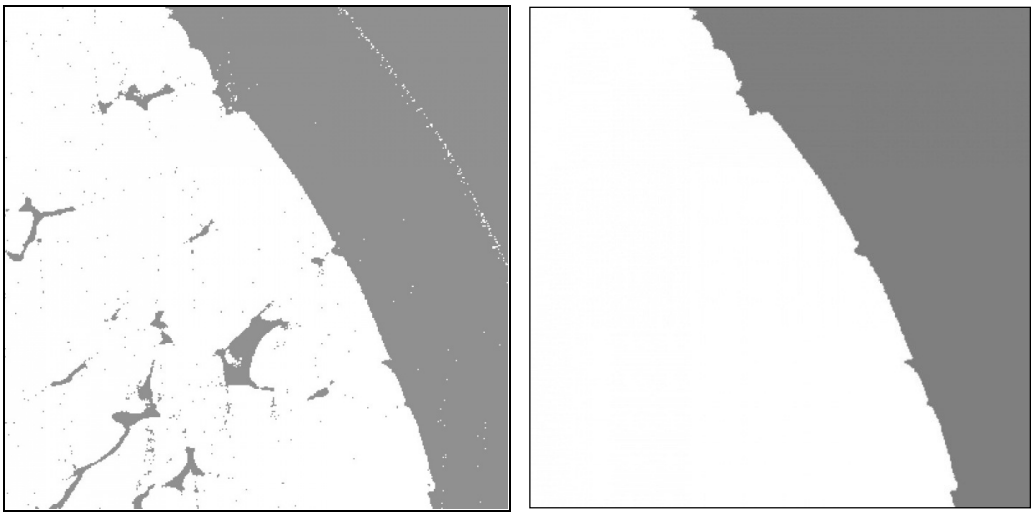

Figure A1.2. (a) The dataset after thresholding contains structure and artifacts which need to be removed. (b) After cleaning, the mask file contains "particle" (white) and "not particle" (grey) regions.

b) Using ImageJ: The result from the first procedure was very good; however, this process is very time consuming. The main purpose of producing one very clean mask file was to use it as a benchmark against other less perfect but less time consuming methods and to reduce the amount of human interaction required and automate this process. The following command was used to create the mask file on each image using ImageJ macro language:

run("Fill Holes", "stack"); % every black hole surrounded by white turns to white.

run("Despeckle", "stack"); % remove small white spots surrounded by black.

run("Remove Outliers...", "radius=5 threshold=50 which=Bright stack").

The last command is to remove larger white spots surrounded by black. The size of the white spot has to be changed until satisfactory results are achieved. However, this is not the final step. The last step still leaves odd bits and pieces that are not part of the particle, so there is one more step, which involves manually selecting the particle and leaving out the rest. A duplicate of the mask created so far is made and then on the copy data set a floodfill algorithm is applied to set all the connected points of the particle to a value of 0, leaving the bits that are unwanted as 255. When done the copy mask file is subtracted from the original mask, which will leave only the particle. Although this method can be automated quite nicely, it was found that using the ImageJ software some of the surface information was lost so other software was explored, namely MATLAB®.

c) Using MATLAB®: MATLAB®, with the Parallel Computing Toolbox, has the advantage of using local servers for distributing work and using 8 processors at a time to speed up the process. The two main MATLAB functions used to create the new mask file are “imfill” and “bwareaopen”. These functions are applied individually to each two dimensional slice of the particle. After reading a slice, the next step is to fill in holes.

The command for filling the holes is:

Ifill = imfill(Image,'holes');

Then, the command "*bwareaopen()*" is then applied to remove all the smaller structure that is outside the particle.

Imask = bwareaopen(Ifill, 1500);

The function "*bwareaopen()*" removes connected components fewer than P pixels (P is some value entered by the user; in this case 1500 was chosen).

At the end of this step a very clean mask file is created in which the surface details of the original mask file have been preserved. This can be seen in Figure A1.3. The codes used for this procedure can be found in Appendix D.

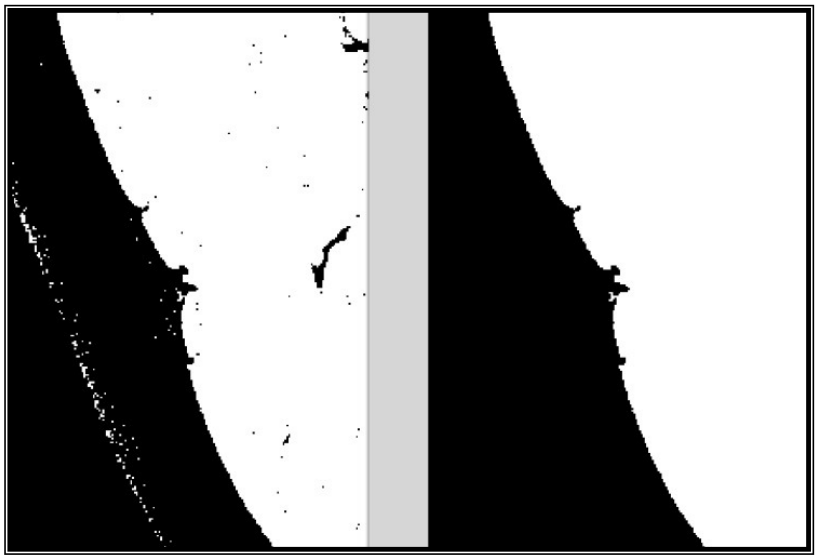

Figure A1.3. The comparison between the original black and white image and the new mask file created using MATLAB®.

Step 5: Analysis:

At this point the original data file with values for each point in the volume in the range [0, 255] for 8-bit data values is available. The mask file contains two values which can in principle be any values, but for simplicity, take them to be 0 for exterior points, and 1 for interior particle points. Comparisons of the corresponding points in the files can be done to ensure that any analyses on the data will be on the particle or on the exterior if so desired. It is also possible to do arithmetic and logical operations using the mask file which might be faster than directly comparing the grid point value. For example to set the exterior values of the data file to 0 simply multiply the corresponding grid points of the two files:

```
mask(i,j,k) * data(i,j,k)
```

or use the mask file in logical functions as:

```
if( mask(i,j,k) )
```

which is TRUE (= 1) for particle points. This enables us to create more complex functions and comparisons in our analysis.

To get a simple approximation of the porosity it is possible to use the mask data file, and the thresholded data file and multiply them as shown in Figure A1.4. The result is a set of connected regions that correspond to the porosity if the data value for porosity is close to the value used for thresholding the data set (Figure A1.5).

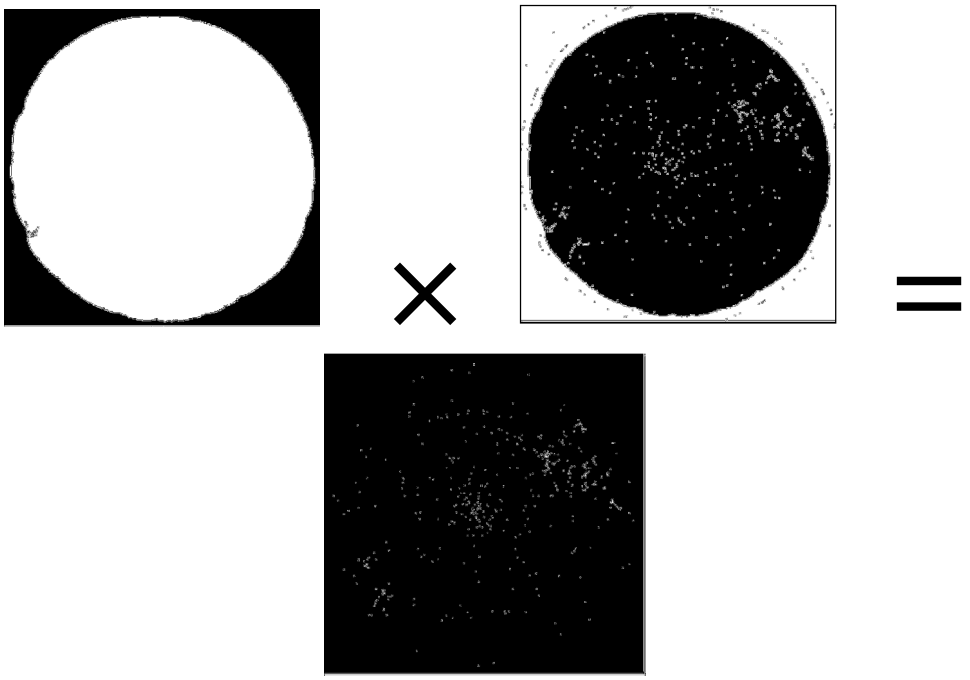

Figure A1.4. Result of multiplying the mask file of slice 1040 by the negative of slice 1040 ran through a threshold of 158.

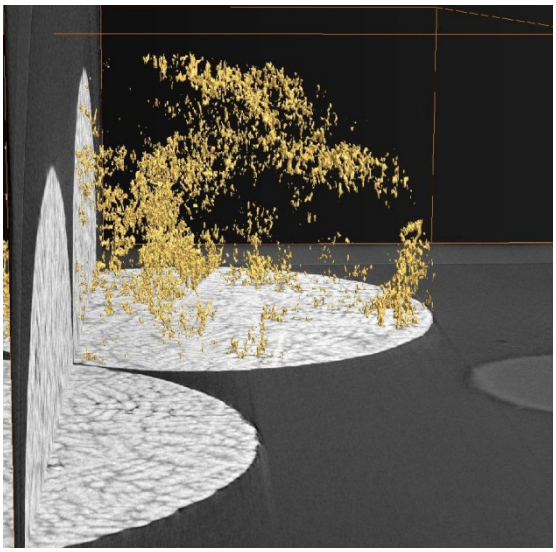

Figure A1.5. The isosurface of pixels threshold at data values = 158 superimposed on orthoslices of the original file (080916) created using Avizo®. Note the existence of one other particle and the background noise in the original data set.

MATLAB® was also used to reduce the number of artifacts in the image. This method is still being investigated to improve the efficiency of the procedure to remove artifacts. The basic method is similar to Step 3 with the addition of a few extra steps. Once the inside of the particle is attained using the aforementioned method then by simply removing structures comprised of 4 or fewer 4-connected pixels, most of the artifacts are removed without removing porosity. Figure 6 shows the inside of the particle of Fig. 4 after the artifacts are removed.

Currently additional MATLAB® capabilities are being explored to eliminate the spiral artifacts. The idea behind this method is to convert the image into polar coordinates, which transforms the artifact rings into lines - lines are generally easier to filter than rings and/or spirals.

When these techniques are applied to Al-50wt%Ni powders, a quantification of the porosity in the particles is feasible.

A1.4. Conclusions

The important conclusion of the current work is that a method is necessary to separate a particle from its background in order to perform meaningful quantitative analyses of particle properties. Avizo®, ImageJ and MATLAB® were used to create mask files that enable one to distinguish between the interior and the exterior of the particles. It was found that the code written in MATLAB® is the most efficient way to create the mask files from the different methods that were used in that it allows for automation of the process, reducing the amount of user time required. Also a method is discussed that allows for decreasing the

amount of X-ray artifacts that appears in a large number of data sets.

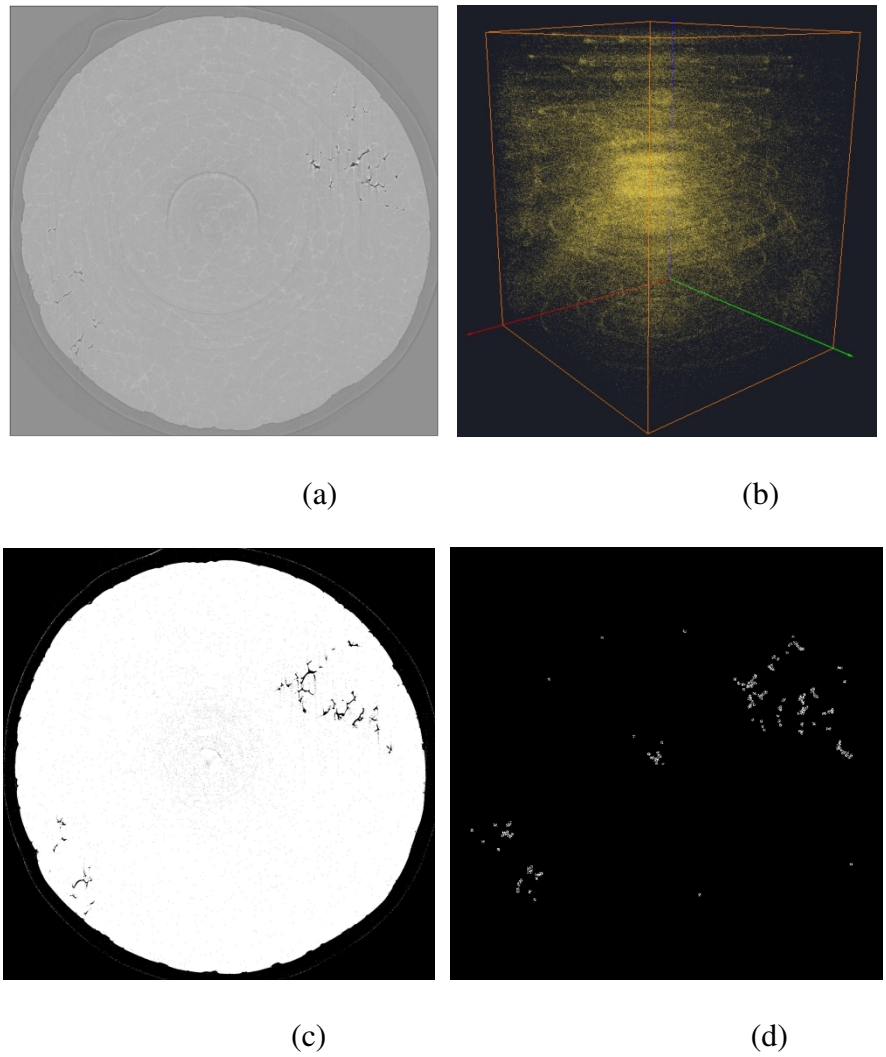

(a) (b)

(c) (d)

Figure A1.6. A series of images to illustrate the effect of artifact removal: (a) slice 990 of particle, (b) 3D reconstruction of articfacts both inside and outside of particle, (c) the inside of the particle (slice 1040) with small (4 and less pixels) structures removed, and (d) the porosity highlighted.

A1.5. References

A1. Jones, H., Rapid Solidification of Metals and Alloys, Whetstone, London: The Institution of Metallurgists, (1982).

A2. Prasad, A., Henein, H., Maire, E. and Gandin, C. A. "X-ray tomography study of atomized al-cu droplets", Canadian Metallurgical Quarterly, 43(2), (2004), 273-282.

A3. Prasad, A., Henein, H., Maire, E. and Gandin, C. A., "Understanding the rapid solidification of al-4.3Cu and al-17Cu using X-ray tomography", Metallurgical and Materials Transactions A, 37(1) (2006) 249-257.

A4. Henein, H. "Current development and opportunities using the Impulse Atomization technique", Science and Technology of Powder Materials: Synthesis, Consolidation and Properties - Proceedings of a Symposium sponsored by Materials Science and Technology 2005, MS&T05, (2005), 213-220.

Appendix B

1. The full set of MATLAB commands (.m file) needed to read, clean, and write a raw mask file for a complete particle:

```
-----------------------------------------------------------------
% create a new mask file without holes or
% extra outside structures
%
% Read a binary datafile and so some processing
fname = 'hh_20.raw';
foutname = 'hh_20_mlmask.raw';
nx = 1840;
ny = 1840;
nz = 1870;
% the data are unit8 for this data set
% allocate space for the arrays
a = zeros(nx, ny, nz, 'uint8');
b = zeros(nx, ny, nz, 'uint8');
%
% Open the file for reading as a binary
infh = fopen( fname, 'rb' );
for k = 1:nz
  a(:,:,k) = fread( infh, [nx, ny], 'uint8' );
end
% done with the data file so close it
fclose(infh);
%
% fill holes and remove structures for each slice
```

```
for k=1:nz
  %grab one image
  Image = a(:,:,k);
  %
  %fill in the holes
  Ifill = imfill(Image,'holes');
  %
  %remove the outside
  % i.e., remove structures less than 1500 pixels
  Imask = bwareaopen(Ifill, 1500);
  %
  % put the image into a new array for output
  b(:,:,k) = uint8(Imask)*255;
end
%
% Open a file for writing the binary results
outfh = fopen(foutname, 'wb');
% Write the results (byte 1840x1840x1870)
 for k = 1:nz
   icount = fwrite(outfh,b(:,:,k),'uint8');
 end
% close the output file
fclose(outfh);
```

Notes: The above .m file will fills holes and removes outside structures for slices in the z direction. For completeness these step should be done for slices in both the x and y directions as well. Here is a code fragment for the x direction:

```
---------------------------------------------------------------
% new output array
c = zeros(nx, ny, nz, 'uint8');
% fill and remove in the x direction
for i=1:nx
  %grab one image
  Image = b(i,:,:);
  %
  %fill in the holes
  Ifill = imfill(Image,'holes');
  %
  %remove the outside
  % i.e., remove structures less than 1500 pixels
  Imask = bwareaopen(Ifill, 1500);
  %
  % put the image into a new array for output
  c(i,:,:) = uint8(Imask)*255;
end
---------------------------------------------------------------
```

Code to account for open to surface porosity:

```
---------------------------------------------------------------
%
 % Read in a test datafile
 image90 = imread('hhi_550a_newmask.0090.tif');
 figure, imshow(image90);
 %
 % find the edge using sobel filter
 %imedgesobel = edge(image90,'sobel');
 %figure, imshow(imedgesobel);
 %
```

```
% find the edge using canny filter
imedgecanny = edge(image90,'canny');
figure, imshow(imedgecanny);
%
% dilate the edge with two lines
% line: length and degrees
%se90 = strel('line', 3, 90);
%se0 = strel('line', 3, 0);
%im90dilate = imdilate(imedgecanny, [se90 se0]);
%figure, imshow(im90dilate);
%
% dilate the edge with a disk
% disk: radius 6
sedisk6 = strel('disk',6);
im90dilate = imdilate(imedgecanny, sedisk6);
figure, imshow(im90dilate);
%
% fill in holes
im90fill = imfill(im90dilate,'holes');
figure, imshow(im90fill);
%
% erode by one or two more than was dilated
sedisk8 = strel('disk',8);
im90erode = imerode(im90fill,sedisk8);
figure, imshow(im90erode);
% check the amount eroded againt the org file
%imcheck = logical(image90) - im90erode;
%figure, imshow(imcheck);
%
% create a new mask with surface porosity
```

```
% included within the mask
im90withsp = logical(image90) | im90erode;
figure, imshow(im90withsp);
```

The full set of MATLAB commands (.m file) needed to read the original mask raw file(the black and white images), read the cleaned mask raw file, find the artifacts and write the artifacts into a new raw file:

```
% create a artifacts mask file
%
% Read a binary datafiles and so some processing
fname = 'hhi_550a_mask.raw';
fnameclm = 'hhi_550a_mlmask.raw';
foutname = 'hhi_550a_artifactsmask.raw';
nx = 1840;
ny = 1840;
nz = 1870;
% the data are unit8 for this data set
% allocate space for the arrays
a = zeros(nx, ny, nz, 'uint8');
aclm = zeros(nx, ny, nz, 'uint8');
b = zeros(nx, ny, nz, 'uint8');
%
% Open the files for reading as a binary
infh = fopen( fname, 'rb' );
infhclm = fopen( fnameclm, 'rb' );
%
for k = 1:nz
```

```
a(:,:,k) = fread( infh, [nx, ny], 'uint8' );
end
for k = 1:nz
aclm(:,:,k) = fread( infhclm, [nx, ny], 'uint8' );
end
% done with the data file so close it
fclose(infh);
fclose(infhclm);
%
% Get the inside of the particle for each slice
% starting with slices in z (following with slices
% in both x and then y)
for k=1:nz
  %grab one image
  Imagemask = a(:,:,k);
  Imageclm = aclm(:,:,k);
  %
  % get the neg of the original mask
  % then get only the inside of the particle
  % clean mask * negative of the original
  Imagemaskneg = ~Imagemask;
  Iinside = logical(Imageclm).*logical(Imagemaskneg);
  %
  % remove structures less than 4 pixels
  Inosmall4 = bwareaopen(Iinside, 4);
  %
  % get a mask of the artiacts
  % inside - nosmallinside; i.e.,(0-0=0 1-0=1 1-1=0)
  Iartionly = Iinside - Inosmall4;
  % put the image into a new array for output
```

```
   b(:,:,k) = uint8(Iartionly)*255;
end
%
% Open a file for writing the binary results
outfh = fopen(foutname, 'wb');
% Write the results (byte 1840x1840x1870)
for k = 1:nz
   icount = fwrite(outfh,b(:,:,k),'uint8');
end
% close the output file
fclose(outfh);
```
